INTERNATIONAL JOURNAL OF
IJCOE
COASTAL, OFFSHORE &
ENVIRONMENTAL ENGINEERING

Optimization of Adaptive Neuro-Fuzzy Inference System using Differential Evolution Algorithm for Scour Prediction around Submerged Pipes
Ali Reza Mahmodian; Behrouz Yaghoubi; fariborz yosevfand

Effect of New Structures at Headland of Crenulate-Shaped Bays on the Equilibrium Shape of Bays in Mokran Coasts
Mohammad Arian; Hassan Akbari; Seyed Mojtaba Hoseini Chavoshi

Numerical Modeling of Wave and Current Patterns of Beris Port in East of Chabahar-Iran
Mesbah Sayehbani; Danial ghaderi

Application of Soft Computing in Forecasting wave height (Case study: Anzali)
Mohammad Akbarinasab; Iman Paeen Afrakoti

Recent Wave Breaking Prediction Formulas Evaluation Based On Compiled Laboratory Data
Behrooz Tadayon; Hamid Dehghani; Cyrus Ershadi

Pitch Motion Response of an Equipped Semi-Submersible Platform with Tuned Sloshing Dampers
Ahmad Reza Mostafa gharabaghi; Arefeh Emami

Volume 4 | Issue 1 | Apr 2019

www.ijcoe.org info@ijcoe.org

www.ijcoe.org

International Journal of Coastal, Offshore and Environmental Engineering (IJCOE)
Vol. 4 | Issue. 1 |Apr 2019
13

International Journal of Coastal, Offshore & Environmental Engineering

Since 2015

ISSN: 2980-8731 (online)

Volume 4| Issue 1| Apr 2019

IJCOE

Editor-in-Chief: Prof. Hamid S.Bahai

International Journal of
Coastal, Offshore
& Environmental
Engineering
Since 2015
ISSN: 2980-8731 (online)

In The Name of God

Message from the Editor-in-Chief

The IJCOE journal office was established in 2015,and its first issue was published in 2016. TheIJCOE covers a wide range of research in thefields of oceanography & ocean technology, aswell as marine industries & marine engineering.The editorial board of IJCOE consists of nearly130 of the greatest scientists and researchersfrom over 30 countries worldwide, and thejournal's review board comprises 1,000 membersfrom all five continents. The membership andapplication process for joining the editorial andreview boards of this journal is ongoing. IJCOE isa research-academic quarterly journal that haspublication and distribution permissions fromthe Press Organization and permission topublish scientific-research articles from theMinistry of Science, Research, and Technology(MSRT) with an "A" rating. It also holds a "Q1"rating from the ISC institute with an impactfactor (IF) of approximately 0.43 and isconsidered a "core journal" (prestigious andoutstanding journal). IJCOE is an open-accessjournal and allows the download and receipt ofaccepted articles in full text for free. It respectsand adheres to copyright and COPE regulations.The journal's office operates 24/7, providingservices to researchers. In addition to publishinga regular quarterly journal, IJCOE has 16 specialissues on specific topics in preparation. It alsoprovides conditions for publishing specializedbooks, references, and handbooks. Moreover, itis ready to cooperate with the secretariats ofreputable international conferences to publishtheir selected and outstanding articles. IJCOEevaluates, appraises, and publishes books,articles, and the scientific achievements andfindings of esteemed researchers and scientistsworldwide who are innovating and conductingin-depth research in the "important and strategicfield of the maritime technology & Oceanengineering." It welcomes any form of jointcooperation with universities, research institutes,and related research centers at the national,regional, and international levels, and extends ahand for collaboration.

Classification of Editorial Board in IJCOE

- Editor-in-Chief
- Director-in-Chief
- Deputy Editor
- Executive Managers
- English Text Editor
- Technical Editor
- International Editorial Board
- National Editorial Board
- Editorial Board Associate
- Editorial Board Assistant
- Guest Editorial Board
- Advisory Board
- Administrative Coordinator
- Honorary Board Member
- Methodology Advisor

Author Benefits

- Open Access
- Rapid Publication
- Thorough Peer-Review
- No Copyright Constraints
- Coverage by Leading Indexing Services
- Discounts On Article Processing Charges (APC)
- No Space Constraints, No restriction on the maximum length of the papers, number of figures or colors

INTERNATIONAL JOURNAL OF
IJCOE
COASTAL, OFFSHORE &
ENVIRONMENTAL ENGINEERING

Aims of IJCOE

Hydrodynamics

Marine equipment

Structural mechanics

Ocean environmental predictions

Stochastic calculations Experimental

Automatic Control of Marine Systems

Scope of IJCOE

Marine Hazards

Ocean Acoustics

Naval Architecture

Ocean Engineering

Coastal Engineering

Marine Meteorology

Marine Earth Sciences

Underwater Technology

Marine Renewable Energy

Polar & Arctic Engineering

Marine Renewable Energy

Marine Geography & Geodesy

Marine Environmental Engineering

Automatic Control of Marine Systems

Hydro Physics & Physical Oceanography

Type of papers

- Case Studies
- Book Reviews
- Review Article
- Letters to the Editor
- Methodology Papers
- Editorials and Commentaries
- Response or Rejoinder Papers
- Perspective or Opinion Papers
- Conceptual or Theoretical Papers
- Meta-Analysis and Systematic Reviews
- Short Communications or Brief Reports
- Research Articles (Original Research Papers)

Scientific Research Journal

Ministry of Science, Research And Technology (MSRT)

Jurnal Ranking 2023: A

Ministry Of Science, Research And Technology (ISC)

Citation Impact 2022: 0.429

Quartile 2022 : Q1

Core Collection

IJCOE is a Member of

- CIVILICA We Respect the Science
- Google Scholar
- Jouroscope
- COPE 20TH ANNIVERSARY 1997-2017 CC BY NC SA
- ISC
- JREF.IR Journals Reference
- DOAJ DIRECTORY OF OPEN ACCESS JOURNALS
- ISSN INTERNATIONAL STANDARD SERIAL NUMBER INTERNATIONAL CENTRE
- Researcher.Life
- doi Crossref EScience Press mEDRA
- iThenticate
- magiran
- OPEN ACCESS
- pistoтn
- ResearchGate
- Regional Information Center for Science and Technology RICEST
- ScienceGate
- Scilit
- SID
- website.informer.com
- WEBrate

Cantact Us

Office 1 | Research Institute of Meteorology and Atmospheric Science

Address | Tehran, Shahid Kharrazi Highway, Pajoohesh Blvd, Research Institute of Meteorology and Atmospheric Science, Sand and Dust Storm International Research Center (SDS-IRC), No. 13, 1st floor.

Phone | +982144787652

Postal code | 13611-14977

website | www.rimac.ac.ir

Office 2 | Iranian National Institute for Oceanography and Atmospheric Science

Address | Tehran, Dr. Fatemi Gharbi St., Shahid Etemadzade St., No. 3, third floor.

Phone | +982166944873

Postal code | 13389 – 14118

website | www.inio.ac.ir

Email | Info@ijcoe.org

Website | www.ijcoe.org

Follow Us

www.ijcoe.org

INTERNATIONAL JOURNAL OF IJCOE COASTAL, OFFSHORE & ENVIRONMENTAL ENGINEERING

Volume & Issue:

Volume 4, Issue 1, April 2019

Number of Articles: 6

Content

INTERNATIONAL JOURNAL OF
COASTAL & OFFSHORE ENGINEERING
IJCOE Vol.4/No. 1/Spring 2019 (1-10)

Available online at: http://ijcoe.org/browse.php?a_code=A-10-214-1&sid=1&slc_lang=en

Optimization of Adaptive Neuro-Fuzzy Inference System using Differential Evolution Algorithm for Scour Prediction around Submerged Pipes

Ali Reza Mahmodian[1], **Behrouz Yaghoubi**[2*], **Fariborz Yosefvand**[2]

[1] *Ph.D. Candidate, Department of Water Engineering, Kermanshah Branch, Islamic Azad University, Kermanshah, Iran*
[2] *Department of Water Engineering, Kermanshah Branch, Islamic Azad University, Kermanshah, Iran; *behrouz.yaghoubi.h@gmail.com*

ARTICLE INFO

Article History:
Received: 7 Jul. 2018
Accepted: 27 Apr. 2019

Keywords:
Scouring
ANFIS
Differential Evolution Algorithm
Submerged Pipes
Hybrid Model

ABSTRACT

Nowadays, a huge amount of natural resources such as gases and oil are exploited from offshore oil fields and transported by pipes located at seabed. The pipelines are exposed to waves and currents and scour may occur around them. Subsequently, stability of the pipes can be threatened, so estimation and simulation of scouring around the pipes are quite vital. In this study, a hybrid method for simulating the scour depth in the vicinity of submerged pipes was developed. In other words, the adaptive neuro-fuzzy inference system (ANFIS) and the differential algorithm were combined with each other to simulate the scour depth. In general, ANFIS is an artificial neural network acts based on the Takagi-Sugeno inference system. This model is a set of if-then rules which is able to approximate non-linear functions. In addition, the differential algorithm is a powerful evolutionary algorithm among optimization algorithms which have many applications in scientific fields. In this study, the Monte-Carlo simulation was employed for examining the ability of numerical models. To validate the modeling results, the k-fold cross validation approach was also utilized with k=6. Then, the parameters affecting the scour depth were detected and six ANFIS and hybrid models were developed for scour estimation. After that, the results of the mentioned models were examined and this analysis showed that the superior model predicts scour values in terms of all input parameters. This model has reasonable accuracy. For example, the values of R and RMSE for this model were calculated 0.974 and 0.079, respectively. Furthermore, the analysis of the modeling results indicated that the ratio of the pipe distance from the sedimentary bed to the pipe diameter (e/D) was identified as the most effective parameter.

1. Introduction

Generally, in coastal regions transmission lines located horizontally on the sea bed are used for operating from oil and gas resources. Due to the existence of transitional flows and tide waves, the possibility of scouring occurrence around submerged pipes must be considered. Erosion of beds beneath pipelines might lead to failure and damage. Therefore, taking effective measures for scour prediction and estimation are essential. Thus, several studies have been carried out by different researchers. Hansen et al. (1986) using the potential theory, analytically examined the scour in the vicinity of pipes located on sedimentary beds. He validated the analytical results with experimental data. Later, Sumer et al. (1988) by conducting an experimental study, evaluated the influence of transverse flows and pipe vibration on the scour pattern around pipelines located on live-beds. Also, Mao (1988) by studying the scour pattern in the vicinity of submerged pipes, stated that there are three types of vortexes forming around the mentioned pipes. Chiew (1993) investigated the influence of vanes attached to submerged pipe walls. He showed that the presence of the mentioned vanes increases the intensity and volume of the scour hole occurring in the vicinity of pipes up to 1.3 times the ordinary pipes.

Moncada et al. (1999) by carrying out an experimental study, examined the scour pattern around horizontal pipes located on sedimentary beds. According to the results, by increasing the Froude number causes to increase the depth and length of the scour hole as well. They also demonstrated that by increasing the diameter of sediment particles, the scour hole dimensions is reduced. Teh et al. (2003) experimentally studied the marine pipelines on unstable and liquefied seabed. By analyzing the experimental results, they proposed a method for designing pipes in such conditions. In addition, Dey and Singh (2008) experimentally studied the scour pattern under clear-water conditions around submerged pipes located on sedimentary beds. They studied the influence of various hydraulic and geometric conditions such as the pipe shape and the distance of the pipe from the bed. They also investigated the influence of the protected bed and stated that the scour depth for the unprotected bed is more than the protected bed. Wu and Chiew (2012) measured the 3D scour pattern in the vicinity of submerged pipes located on sedimentary beds under clear-water conditions by conducting an experiment. They examined the influence of different parameters on the scour hole and indicated that by increasing the Froude number and Shields parameters, the scouring process accelerates. Yang et al. (2012) experimentally studied the impact of the presence of rubber sheets and flow guidance vanes on the scour pattern around submerged pipes subjected to waves. They indicated that the use of rubber sheets with 1.5 times pipe dimensions is the best way for protecting sedimentary beds. Luan et al. (2015) in a numerical study simulated the effects of submerged pipe vibrations on the bed scour pattern in a two-dimensional way. They proved that by increasing the frequency and the range of vibrations, the scour hole dimensions increase as well. Currently, various neural networks and different neuro-fuzzy techniques are used in pattern cognition, prediction and estimation of complex hydrological and hydraulic phenomena. Etemad-Shahidi and Kazeminezhad (2011) by means of the M5'model, approximated the scour pattern around submerged pipes under clear-water and live-bed conditions. By reviewing the modeling results, they deduced that the Shields number is the most effective factor in the scour prediction under the mentioned conditions. Furthermore, they suggested a number of relationships for calculating scouring. Also, Najafzadeh et al. (2014) using the group method of data handling (GMDH) method, the ANFIS model, the tree model and empirical equations, predicted the scour pattern around submerged pipes located on sedimentary beds. By evaluating the results, they demonstrated that the GMDH method forecasts scour values with higher accuracy.

On the one hand, natural resources such as oil and gases are transported by pipelines and after a while scour phenomenon may occur in the vicinity of such facilities. The scouring can damage the pipelines and threatened the stability of these infrastructures.

On the other hand, many artificial intelligence studies have been carried out to model various engineering problems, with increasing such studies every day. The AI models such as Artificial Neural Networks (ANNs), Support Vector Machine (SVM), Gene Expression Programing (GEP) and Adaptive neuro fuzzy inference systems (ANFIS) are quite popular and practical. Generally, ANFIS network has been widely applied to model multifarious problems because it is a universal estimator and integrates both neural networks (NNs) and fuzzy logic principles in a single framework. By contrast, the model has some limitations. For instance, ANFIS uses different rules and numerous optimized parameters for modelling, so uncertainty of results is pretty high.

Moreover, optimization algorithms like such as gradient descent and least-square approaches may be useful, however they may have some disadvantages including trapping in local optimum and high-volume of computations. To overcome these challenges, other optimization tools are utilized in different areas. For instance, genetic algorithm (Azimi et al 2017a), singular value decomposition (Khoshbin et al. 2016), differential evolution (Ebtehaj et al. 2017; Azimi et al. 2017b) and firefly algorithm (Azimi et al. 2018) were applied to optimize artificial intelligence models.

Therefore, for the first time, differential evolution (DE) algorithm is applied for optimization of the ANFIS network in order to estimate scour around submerged pipelines in clear-water conditions. To do this, firstly, the applied numerical models are introduced. Secondly, the experimental model will be presented. Next, using the important input parameters, six ANFIS and ANFIS-DE are defined. Then, numerical models are analyzed and the most effective input parameter and the superior model are identified.

2. Material and methods

2.1. Adaptive Neuro-Fuzzy Inference System

This method was introduced by Yang (1993) for the first time. The structure of ANFIS comprises five layers including input nodes, base nodes, medium nodes, response nodes and output nodes which are directly connected (Figure1). Each node is function of adjustable or fixed parameters. The proper structure of the ANFIS technique is chosen proportional with output data. In the learning step, by correcting parameters of the degree of membership based on the acceptable error, input values get closer to actual values. The ANFIS technique uses neural network learning and fuzzy logic algorithms for conducting non-linear mapping into the space between inputs and outputs. This algorithm also has a good ability in learning, construction and classification. In addition, this system is able to extract fuzzy rules from numerical data or the expert knowledge and creates a rule-base adaptively. Furthermore, this algorithm can adjust the transformation of mankind complex intelligence to the fuzzy system. The learning rule is based on the error back-propagation with a view to minimizing the error between the network output and the actual output. It worth noting that other evolutionary algorithms could be also used in such cases.

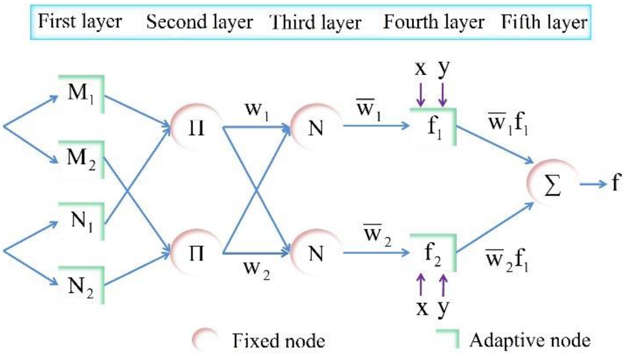

Figure1- Architecture of ANFIS network

Most fuzzy inference systems comprise three types including the Mamdani, Sugeno and Tsukamoto systems which in most cases the Mamdani system is employed, however the Sugeno system has a better performance and has the actual output. Thus, in this study, by programming in the MATLAB, the modeling is conducted by the ANFIS method using the Sugeno system. In addition, the hybrid learning algorithm which is a combination of the back-propagation and the least square method is used for learning and adapting with the fuzzy inference system. The membership function in the fuzzy inference system comprises several adjustable parameters. In order to achieve an optimized modeling, these parameters must be optimized. Thus, a more powerful algorithm is required for defining the values. There are many optimized algorithms which are able to enhance the performance of fuzzy systems. The differential evolution (DE) algorithm is one of these algorithms which is a suitable tool for optimization. This algorithm is able to minimize the error between the model output and the actual value of learning data.

2.2. Differential Evolution Algorithm

The differential evolution (DE) optimization algorithm provided by Storm R. and Price (1995). As a global search method, it is employed for optimizing membership function parameters in combination with ANFIS. The DE algorithm is a simple search approach yet with a powerful population based on the direct random search often used for selecting network parameters. The objective of DE is minimizing the objective function *f(θ)*. Where, $\theta \in R^D$ is the parameter vector. The DE algorithm produces a population of NP unique parameter vectors in order to reach the global optimization. In the generation *G*, the i_{th} parameter vector is as follows:

$$\theta_{i,G} = \left[\theta^1_{i,G}, \theta^2_{i,G}, \ldots, \theta^d_{i,G}\right] \quad i = 1,2,\ldots,NP \tag{1}$$

The general procedure of the DE algorithm includes four steps as follows:

First step: initial initialization

A set of *NP* unique parameter vectors $\theta_{i,G}$ is used to cover the parameter space so that the following equation is established:

$$\theta_{i,G} = \theta_{min} + rand(0.1)\left(\theta_{max} \quad \theta_{min}\right) \tag{2}$$

Here,

$\theta_{min} = \left[\theta^1_{min}, \theta^2_{min}, \ldots, \theta^D_{min}\right]$ and $\theta_{max} = \left[\theta^1_{max}, \theta^2_{max}, \ldots, \theta^D_{max}\right]$ are determined as minimum and maximum criteria, respectively.

Second step: mutation

Based on the unique parameter vector $\theta_{i,G}$ in the current generation, the mutated vector $v_{i,G}$ is produced through a special mutated strategy. Many mutated strategies have been proposed for solving different problems. Here, four important strategies are expressed.

Strategy 1: DE/rand/1

$$v_{i,G} = \theta_{r_1^j,G} + F.\left(\theta_{r_2^i,G} \quad \theta_{r_3^i,G}\right) \tag{3}$$

Strategy 2: DE/rand-to-best/2

$$v_{i,G} = \theta_{r_1^j,G} + F.\left(\theta_{best,G} \quad \theta_{r_1^i,G}\right) + F.\left(\theta_{r_2^i,G} \quad \theta_{r_3^i,G}\right) + F.\left(\theta_{r_4^i,G} \quad \theta_{r_5^i,G}\right) \tag{4}$$

Strategy 3: DE/rand/2

$$v_{i,G} = \theta_{r_1^j,G} + F.\left(\theta_{r_2^i,G} \quad \theta_{r_3^i,G}\right) + F.\left(\theta_{r_4^i,G} \quad \theta_{r_5^i,G}\right) \tag{5}$$

Strategy 4: DE/current-to-rand/1

$$v_{i,G} = \theta_{i,G} + K.\left(\theta_{r_1^i,G} \quad \theta_{i,G}\right) + F.\left(\theta_{r_2^i,G} \quad \theta_{r_3^i,G}\right) \tag{6}$$

In all equations, $r_1^i, r_2^i, r_3^i, r_4^i, r_5^i$, integer indices are unique produced randomly in the domain on $[1,2,\ldots,NP]$ and are different from the index *i*. The positive reinforcement factor *F* is used for controling the scale of differential vectors and is usually chosen in the range of $0 \leq F \leq 2$. The control parameter *K* is produced in the range of $0 \leq K \leq 1$.

The DE/rand/1 strategy is suitable for solving multi-purposes problems due to its powerful search ability, though its slow convergence speed. The DE/rand-to-best/2 strategy based on the best solution found so far, convergences fast in encountering with strategic issues and acts well. Although, during solving multi-purposes problems this strategy is stuck in the local optimization and it leads to fast convergence. Two strategies based on the differential vector (DE/rand-to-best/2 and DE/rand/2) have better mutation compared to a based on differential vector strategy, but they have high computational cost. DE/current-to-rand/1 is an unchangeable rotation. As shown, this strategy is efficient in solving multi-purposes optimization problems.

Third step: reproduction

After production of all mutated vectors, the reproduction method is implemented for increasing variations of disruptive vectors. For each mutated vector $v_{i,G} = \left[v_{i,G}^1, v_{i,G}^2, \ldots, v_{i,G}^d\right]$ in the generation *G*, a test vector $u_{i,G} = \left[u_{i,G}^1, u_{i,G}^2, \ldots, u_{i,G}^d\right]$ is created based on the following reproduction formula:

$$u_{i,G}^J = \begin{cases} v_{i,G}^J & if\left(rand_j \leq CR\right) \quad or \quad \left(j = j_{rand}\right) \\ & \theta_{i,G}^j \quad Otherwise \end{cases} \tag{7}$$

Where, CR is the reproduction rate rewritten from the mutated vector for a fraction of the parameter value and choses a positive value in the range between 0 and 1. $rand_j$ is the j_{th} evolution of the uniform random number production with a result of [0,1]. j_{rand} is a selected integer number from [1, d] and is used to ensure there is at least one parameter in $u_{i,G}$ different from the objective vector $\theta_{i,G}$ .D is the dimension of the desired problem.

Fourth step: selection

For each objective function and the test vector related to it, the selection step is carried out by means of the fitness function. The vector with a value less than the objective function is kept as the population of the next generation. Step 2 to step 4 continues until the objective is satisfied or the maximum iteration is achieved.

2.3. Experimental Model

In this study, the experimental data obtained by Moncada and Aguirre (1999) are used for validating the results of the hybrid model. The mentioned experimental model consists of a rectangular channel with transverse submerged pipes located on the sedimentary bed. Length, width and height of the mentioned channel are reported 8.3m, 0.5m and 0.5m, respectively. They stated that in this experimental model, four types of pipes and sediments with two different diameters are employed. The schematic of scouring in the vicinity of horizontal submerged pipes located on sedimentary beds is illustrated in Figure 2. Furthermore, in Table1 the range of the experimental values used for validating the ANFIS-DE models are shown.

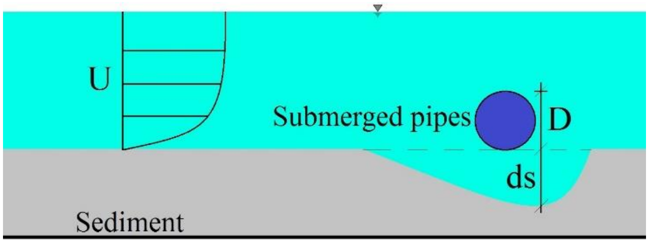

Figure2- Schematic of scouring around horizontal submerged pipes on sedimentary beds

Table1- Range of experimental values used for validating ANFIS-DE models

Parameter	Minimum	Maximum
e/D	0	1.068
D/d_{50}	3.289	66.667
y/D	1.067	5
τ^*	0.038	0.665
Fr	0.238	0.836
d_s/D	0.008	1.606

2.4. Scouring around submerged pipes on sedimentary beds

In general, scouring around horizontal submerged pipes (*S*) is a function of the average velocity of the flow (*U*), the normal flow depth (*y*), the density of water (ρ), the density of sediment(ρ_s), the kinematic viscosity of water(μ), the channel slope (S_0), the channel width (*B*), the diameter of bed sediments (d_{50}), pipe diameter (*D*), the distance between the pipe and sedimentary bed before scouring (*e*) and gravitational acceleration (*g*) (Moncada and Aguirre, 1999):

$$S = f\left(U, y, \rho, \rho_s, \mu, S_0, B, d_{50}, D, e, g\right) \tag{8}$$

By conducting the dimensional analysis and introducing eight dimensionless group, Equation (8) is rewritten as follows:

$$S/D = f\left(Fr, Re, \tau^*, y/D, D/d_{50}, e/D, S_0, y/B\right) \tag{9}$$

Where, $Fr = U/\sqrt{g.y}$, $Re = UD\mu/g$ and $\tau^* = u_*^2/g.\left(\rho_s/\rho \quad 1\right).d_{50}$ are the Froude number, the Reynolds number and the Shields dimensionless number due to the sediment transport. In Moncada and Aguirre (1999) study, bed slope (S_0) is considered constant and the Reynolds number is placed in a range with no effect on the scour pattern. Thus, Equation (9) is written as follows:

$$S/D = f\left(Fr, \tau^*, y/D, D/d_{50}, e/D\right) \tag{10}$$

The dimensionless parameters of Equation (10) are used as the input parameters of different ANFIS-DE models. In Figure 3, combinations of the Equation (10) parameters for six ANFIS-DE models are illustrated.

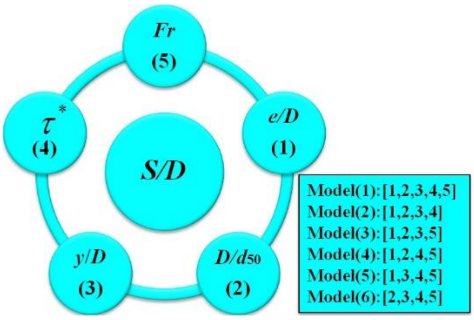

Figure3- Combinations of input parameters for six ANFIS-DE models

In this study, the Monte Carlo simulations are used for examining the abilities of the numerical models. These simulations are a broad classification of computational algorithms using random sampling for calculating numerical results. The Monte-Carlo methods are usually implemented for simulating physical and mathematical systems which are not solvable by means of other methods. Furthermore, the k-fold cross validation method is utilized for examining the proficiency of the mentioned models. In the k-fold cross validation method, the main sample is divided into k sub-samples with the same size randomly. Among k sub-samples, one sub-sample is used as the validation data and the remaining (k-1) as the test data of the model. Then, the method repeats k times so that each k sub-sample is used exactly once as the validation data once. The results obtained from the mentioned k layers are averaged and provided as an approximation. The advantage of this method is the random repetition of sub-samples in the test and learning process for all observations. In this paper, the k value is assumed 6. The dealing of the k-fold cross validation method with the experimental data in the test and learning conditions are depicted in Figure4.

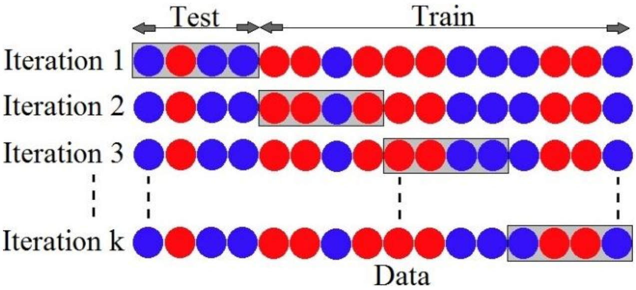

Figure4- Dealing of k-fold Cross Validation with experimental data in test and learning conditions

3. Results

In this study, the correlation coefficient (R), the root mean square error (RMSE) and the scatter index (SI) are used for examining the accuracy of different numerical models:

$$R=\frac{\sum_{i=1}^{n}\left((d_s/D)_{(Observed)i}-\overline{(d_s/D)}_{(Observed)}\right)\left((d_s/D)_{(\Pr edicted)i}-\overline{(d_s/D)}_{(\Pr edicted)}\right)}{\sqrt{\sum_{i=1}^{n}\left((d_s/D)_{(Observed)i}-\overline{(d_s/D)}_{(Observed)}\right)^2\sum_{i=1}^{n}\left((d_s/D)_{(\Pr edicted)i}-\overline{(d_s/D)}_{(\Pr edicted)}\right)^2}} \tag{11}$$

$$RMSE=\sqrt{\frac{1}{n}\sum_{i=1}^{n}\left((d_s/D)_{(\Pr edicted)_i}-(d_s/D)_{(Observed)_i}\right)^2} \tag{12}$$

$$SI=\frac{RMSE}{\overline{(d_s/D)}_{(Observed)}} \tag{13}$$

Where, $(d_s/D)_{(Observed)i}$, $(d_s/D)_{(\Pr edicted)i}$, $\overline{(d_s/D)}_{(Observed)}$ and n are experimental scour, predicted scour, average experimental scour and the number of experimental measurements, respectively.

As discussed, in this study, six models with different combinations of input parameters are introduced. Model1 is a function of all inputs, while Model2 to Model6 simulate scour values in the vicinity of horizontal submerged pipes by a combination of four input parameter.

First, six ANFIS models are investigated. In Figure 5, the variations of the correlation coefficient (R) versus RMSE and SI for the ANFIS models are shown. The scatter plots for different ANFIS models are shown in Figure 6. The ANFIS (1) model is a function of all input parameters. The R value for this model is equal to 0.968. Meanwhile, the values of RMSE and SI for this model are estimated 0.087 and 0.099, respectively. In the following, the models with four input parameters are evaluated. For example, the values of R and RMSE for the ANFIS (2) model are obtained 0.968 and 0.086, respectively. This model is a function of the dimensionless parameters τ^*, *y/D*, *D/d*$_{50}$, *e/D*. In other words, the influence of the Froude number is eliminated for scour simulation around submerged pipes. According to the modeling results, the results of Model1 and Model2 are very close to each other. In other words, elimination of the influence of the Froude number has no significant impact on the modeling accuracy. ANFIS (3) is a function of *Fr*, *y/D*, *D/d*$_{50}$, *e/D*. For this model, the influence of the dimensionless Shields number is neglected due to the sediment transport. For this model, the value of RMSE and R are considered 0.100 and 0.958, respectively. Also, the value of SI for this model is 0.114. In order to estimate the scour depth around horizontal submerged pipes by ANFIS (4), the influence of *y/D* is removed. Furthermore, the values of SI and RMSE for the mentioned model are 0.967 and 0.089, respectively. In the following, the accuracy of ANFIS (5) is evaluated. This model estimates the objective function in terms of Fr, τ^*, y/D, e/D. The influence of the parameter D/d_{50} is neglected for the mentioned model. The values of RMSE and R for the ANFIS (5) mode are calculated 0.116 and 0.939, respectively. Meanwhile, among all models with four inputs the ANFIS (6) model has the lowest accuracy and the maximum error value. In other words, the values of R and RMSE for this model are obtained 0.896 and 0.116, respectively. However, the SI value for the mentioned model is calculated equal to 0.167.

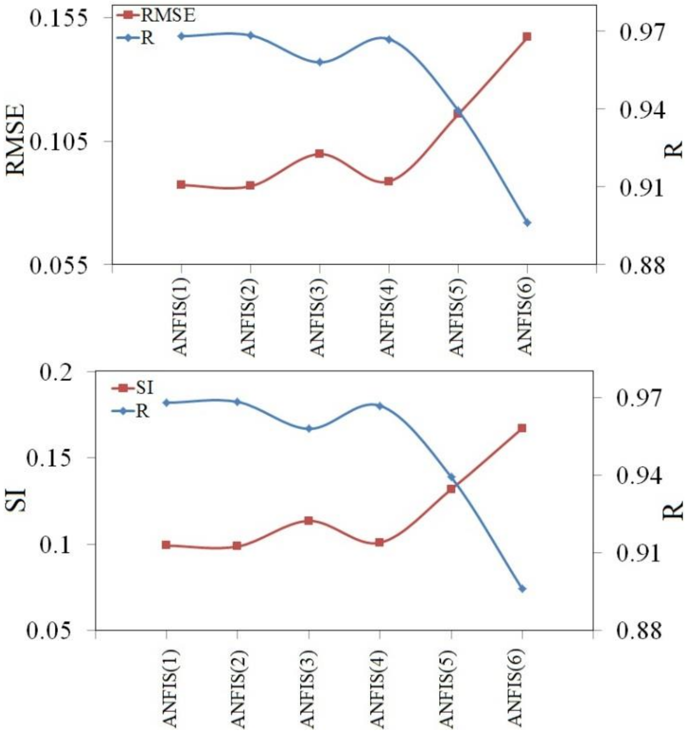

Figure 5- Variations of R versus RMSE and SI for different ANFIS models

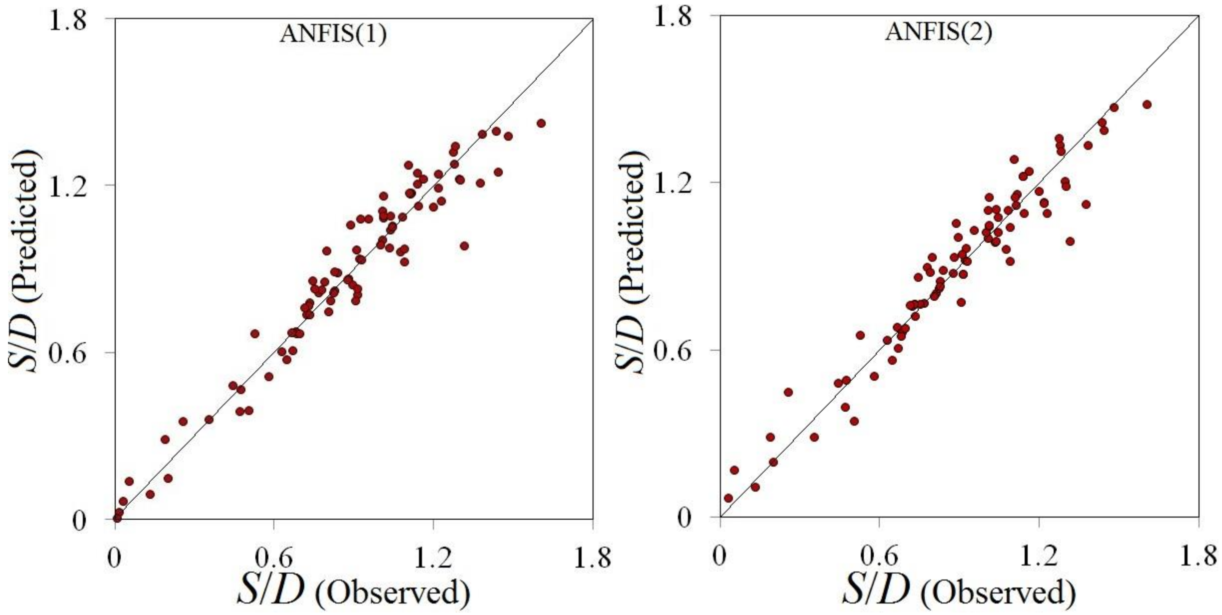

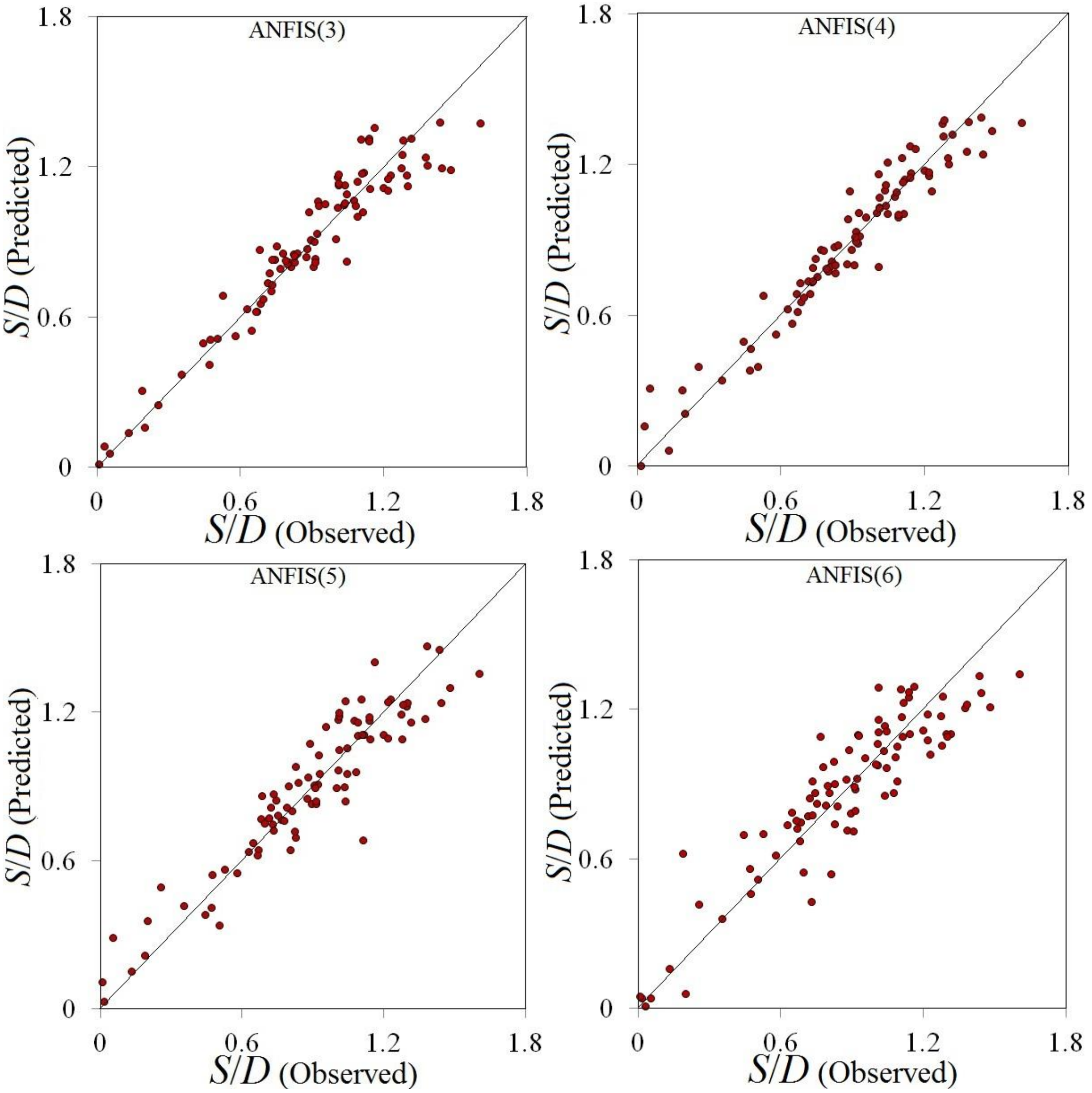

Figure6- Scatter plots for different ANFIS models

Next, the ANFIS-DE models are investigated. In Figure7, the variations of R versus RMSE and SI for the mentioned models are shown. Also, the scatter plots for these models are depicted in Figure8. Similar to the ANFIS models, in the hybrid model the ANFIS-DE (1) model has also the highest accuracy among all models. For example, the values of R and RMSE for the mentioned models are calculated 0.974 and 0.079, respectively. For this model, the SI value is estimated 0.090. Also, for the ANFIS-DE (2) model, the R value is equal to 0.973 and the RMSE index is equal to 0.081. Among all ANFIS-DE models with four input parameters, ANFIS-DE (3) has the highest accuracy. For the mentioned model, the values of RMSE and R are estimated 0.974 and 0.079, respectively. Additionally, scatter index for ANFIS-DE (3) is almost 0.090. In the following, the accuracy of the ANFIS-DE (4) model is examined. For this model, the values of R, SI and RMSE are 0.966, 0.103 and 0.090, respectively. For the model, the effect of the τ^* is eliminated and ANFIS-DE (4) simulates the target parameter as a function of other input parameters.

In addition, for the ANFIS-DE (5) model, the values of R and RMSE are 0.952 and 0.104, respectively. Also, for the mentioned model the value of SI is calculated 0.118. It should be noted that the influence of d/D_{50} is removed for ANFIS-DE (5). Among all meta-heuristics models, the ANFIS-DE (6) model has the lowest accuracy and the maximum error value. For the mentioned model, the values of R and RMSE are computed 0.903 and 0.144, respectively. Furthermore, SI index for this model is obtained 0.163. For estimation the scour function using ANFIS-DE (6), the effect of e/D is ignored.

As discussed, the accuracy of the ANFIS-DE models corresponding with the ANFIS models is higher which shows that the hybrid algorithm is optimized. In addition, among all numerical models, the ANFIS-DE (1) has the highest correlation with the experimental values. This model predicts scour values in terms of all input parameters. Thus, the ANFIS-DE (1) is detected as the superior model. Furthermore, by eliminating the parameter *e/D*, the modeling accuracy is significantly reduced. So, this parameter is identified as the most effective factor in scour estimation in the vicinity of submerged pipes.

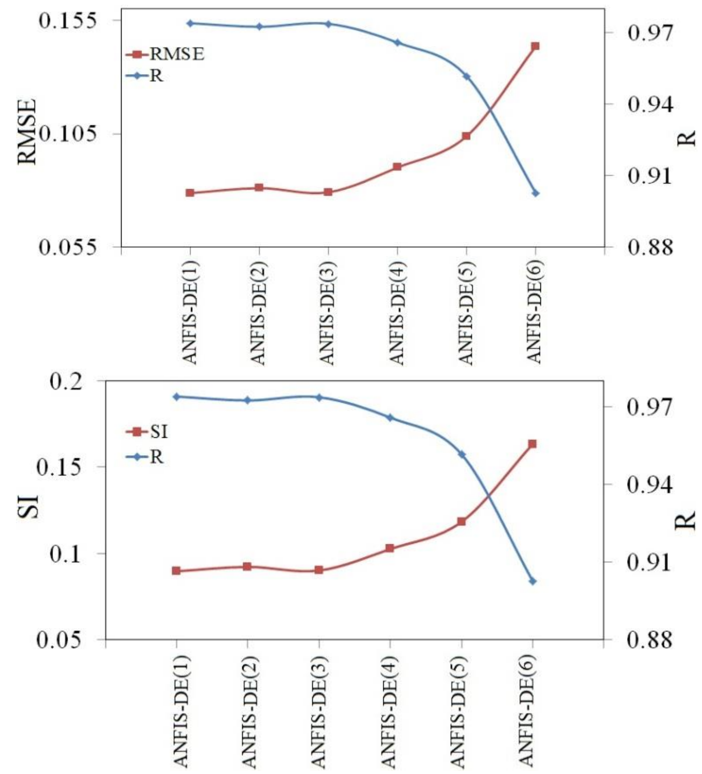

Figure7- Variations of R versus RMSE and SI for different ANFIS-DE models

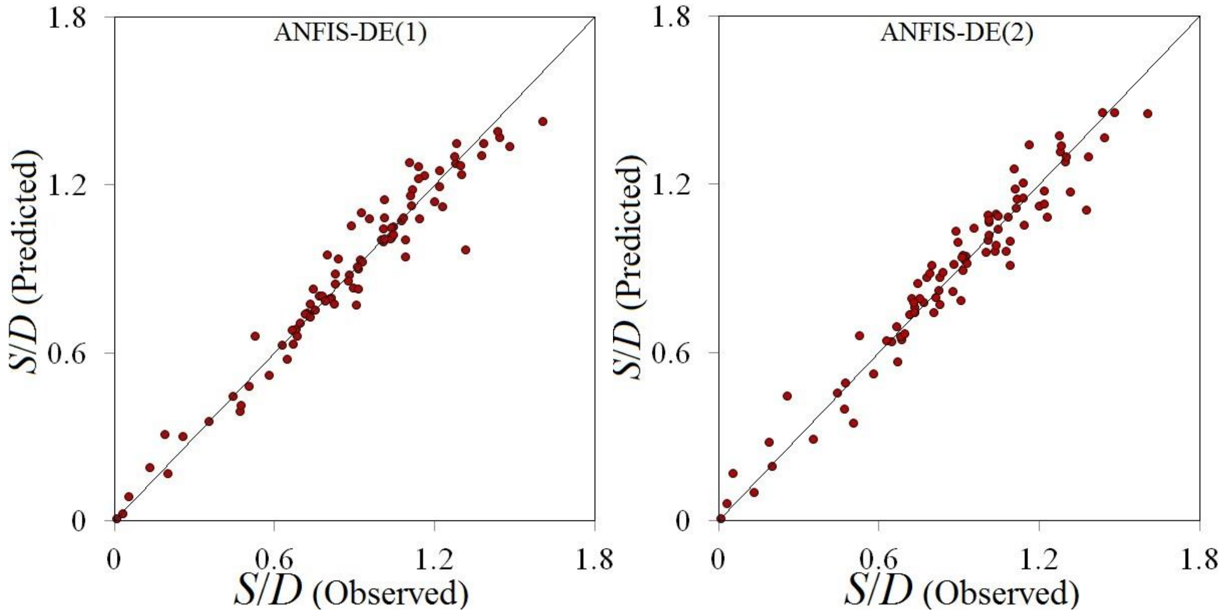

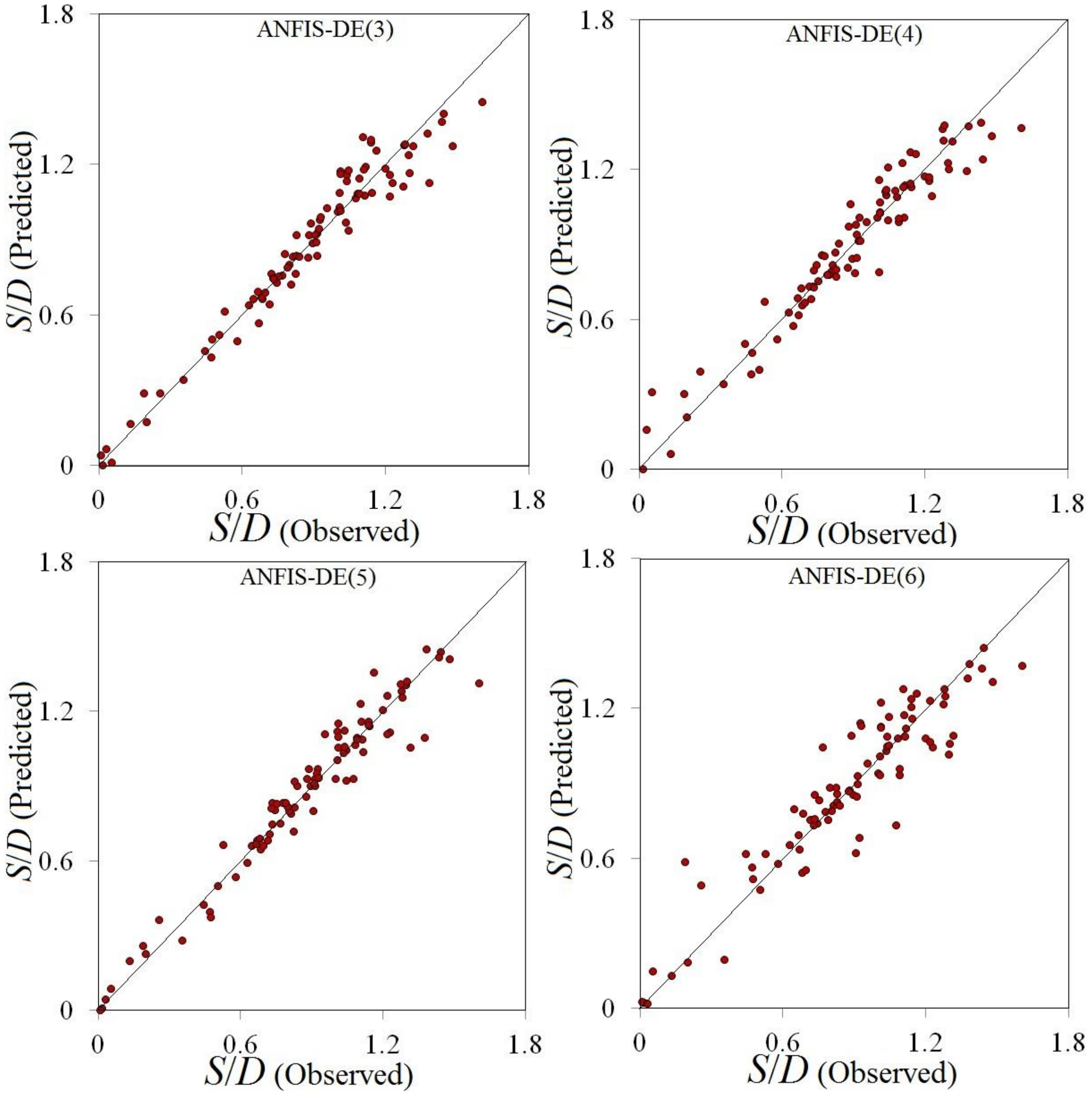

Figure8- Scatter plots for ANFIS-DE different models

4. Discussion and Conclusion

Today, the transfer of oil derivations and gas condensates produced in the coastal regions is performed through pipelines. In general, pipelines are passed above sedimentary beds and due to the presence of coastal flows and waves the possibility of scouring must be considered. In this study, first, the parameters affecting the scour depth around submerged pipes were identified. Then, a hybrid model was developed using the ANFIS model and the differential evolution (DE) algorithm (ANFIS-DE). Based on the input parameters, six ANFIS models and six ANFIS-DE models were introduced. By analyzing the modeling results, the superior model for each of the ANFIS and hybrid models was detected. The superior models predicted the scour values with reasonable accuracy. For example, the value of the correlation coefficient (R) for the ANFIS and hybrid models were calculated 0.968 and 0.974, respectively. Both models estimated the scour values using a combination of all input parameters. It should be noted that the hybrid algorithm modeled the objective function values with higher accuracy compared to the ANFIS model. In other words, the DE algorithm optimized the ANFIS model. In addition, the analysis of the modeling results indicated that the ratio of the distance between the submerged pipe and the sedimentary bed to the pipe diameter is the most effective factor in simulating the scour depth by the mentioned algorithm.

5. References

1. Hansen, E.A., Fredsoe, J. and Mao, Y., (1986), *Two-directional scour below pipelines*, Fifth Internat. Symp. on Offshore Mech. and Arctic Energy, American Society of Mechanical Engineering, Vol. 3, p.670.

2. Sumer, B.M., Mao, Y. and Fredsøe, J., (1988), *Interaction between vibrating pipe and erodible bed*,

Journal of Waterway, Port, Coastal, and Ocean Engineering, Vol. 114(1), p.81-92.

3. Mao, Y., (1988), *Seabed scour under pipelines*, In OMAE 1988 Houston, Proc. 7th Int. Conf. on Offshore Mechanics and Arctic Engineering, Am. Soc. Civ. Engineers, Houston, TX, 7-12.

4. Chiew, Y.M., (1993), *Effect of spoilers on wave-induced scour at submarine pipelines*, Journal of waterway, port, coastal, and ocean engineering, Vol. 119(4), p.417-428.

5. Moncada-M, A.T. and Aguirre-Pe, J., (1999), *Scour below pipeline in river crossings*, Journal of Hydraulic Engineering, Vol. 125(9), p.953-958.

6. Teh, T.C., Palmer, A.C. and Damgaard, J.S., (2003), *Experimental study of marine pipelines on unstable and liquefied seabed*, Coastal Engineering, Vol. 50(1), p.1-17.

7. Dey, S. and Singh, N.P., (2008), *Clear-water scour below underwater pipelines under steady flow*, Journal of hydraulic engineering, Vol. 134(5), p.588-600.

8. Wu, Y. and Chiew, Y.M., (2012), *Three-dimensional scour at submarine pipelines*, Journal of Hydraulic Engineering, Vol. 138(9), p.788-795.

9. Yang, L., Guo, Y., Shi, B., Kuang, C., Xu, W. and Cao, S., (2012), *Study of scour around submarine pipeline with a rubber plate or rigid spoiler in wave conditions*, Journal of Waterway, Port, Coastal, and Ocean Engineering, Vol. 138(6), p.484-490.

10. Luan, Y., Liang, D. and Rana, R., (2015), *Scour depth beneath a pipeline undergoing forced vibration, Theoretical and Applied Mechanics Letters*, Vol. 5(2), p.97-100.

11. Etemad-Shahidi, A., Yasa, R. and Kazeminezhad, M.H., (2011), *Prediction of wave-induced scour depth under submarine pipelines using machine learning approach*. Applied Ocean Research, Vol. 33(1), p.54-59.

12. Najafzadeh, M., Barani, G.A. and Hessami Kermani, M.R., (2014), *Estimation of pipeline scour due to waves by GMDH*. Journal of Pipeline Systems Engineering and Practice, Vol. 5(3), p.06014002.

13. Azimi, H., Shabanlou, S., Ebtehaj, I., Bonakdari, H. and Kardar, S., (2017), *Combination of computational fluid dynamics, adaptive neuro-fuzzy inference system, and genetic algorithm for predicting discharge coefficient of rectangular side orifices*. Journal of Irrigation and Drainage Engineering, Vol. 143(7), p.04017015.

14. Khoshbin, F., Bonakdari, H., Ashraf Talesh, S. H., Ebtehaj, I., Zaji, A. H. and Azimi, H., (2016), *Adaptive neuro-fuzzy inference system multi-objective optimization using the genetic algorithm/singular value decomposition method for modelling the discharge coefficient in rectangular sharp-crested side weirs*, Engineering Optimization, Vol. 48(6), p.933-948.

15. Ebtehaj, I., Sattar, A., Bonakdari, H. and Zaji, A. H., (2017), *Prediction of scour depth around bridge piers using self-adaptive extreme learning machine*, Journal of Hydroinformatics, Vol. 19(2), p.207-224.

16. Azimi, H., Bonakdari, H., Ebtehaj, I., Talesh, S. H. A., Michelson, D. G. and Jamali, A., (2017), *Evolutionary Pareto optimization of an ANFIS network for modeling scour at pile groups in clear water condition*, Fuzzy Sets and Systems, Vol. 319, p.50-69.

17. Azimi, H., Bonakdari, H., Ebtehaj, I. and Michelson, D. G, (2018), *A combined adaptive neuro-fuzzy inference system–firefly algorithm model for predicting the roller length of a hydraulic jump on a rough channel bed*, Neural Computing and Applications, Vol. 29(6), p.249-258.

18. Jang, J.S., (1993), *ANFIS: adaptive-network-based fuzzy inference system*, IEEE transactions on systems, man, and cybernetics, Vol. 23(3), p.665-685.

19. Storm, R. and Price, K., (1995), *Differential evolution—a simple and efficient adaptive scheme for global optimization over continuous spaces*. ICSI Technical Report.

INTERNATIONAL JOURNAL OF
COASTAL & OFFSHORE ENGINEERING

IJCOE Vol.4/No. 1/Spring 2019 (11-20)

Available online at: http://ijcoe.org/browse.php?a_code=A-10-70-3&sid=1&slc_lang=en

Effect of New Structures at Headland of Crenulate-Shaped Bays on the Equilibrium Shape of Bays in Mokran Coasts

Mohammad Arian[1], Hassan Akbari[2*], Seyed Mojtaba Hoseini Chavoshi[3]

[1] *MSc in coastal engineering, Tarbiat Modares University; mehrshad_aryan@modares.ac.ir*
[2*] *Assistant Professor, Tarbiat Modares; akbari.h@modares.ac.ir*
[3] *MSc in coastal engineering, University of Qom; sm.hoseini@stu.qom.ac.ir*

ARTICLE INFO

Article History:
Received: 4 Dec. 2018
Accepted: 22 May 2019

Keywords:
Shoreline changes
Crenulate-shaped bays
Long term morphological simulation
Mepbay
One-line models (COVE)

ABSTRACT

Construction of a new coastal structure changes the stable shape of the shoreline. This issue generally leads to sedimentation and erosion around adjacent structures due to changes in Littoral Sediment Transport (LST). This mechanism is considerably more complicated in crenulate-shaped bays than in straight shorelines. Therefore, special theories have been introduced for these bays. In addition to the above-mentioned difficulties, using two-dimensional long-term morphological models with considerable run times is not practical in most real cases. Instability and numerical errors may also be occurred due to the complicated forms of shorelines. The aim of this research is to introduce a proper morphological model for South-Eastern shorelines of Iran. Long term morphological simulation has been done for three important bays in the Mokran coasts using numerical and empirical models. The results show that these models are appropriate for understanding the behavior of crenulate-shaped bays. Their responses to natural changes like climate changes as well as human interventions can also be simulated properly.

1. Introduction

One of the particular types of bays formed by swell waves attacking from a particular direction is Crenulate-shaped bays. They are formed naturally and/ or due to the construction of coastal structures. These bays have different shapes, but all of them usually have three parts including a curved zone, a gentle transmission zone (from the curved to straight) and a straight tangent segment.

After analyzing these bays, [Silvester and Hsu, 1997] divided them into three categories, static equilibrium, dynamic equilibrium, and unstable or natural reshaping bays. The static equilibrium occurs in a region with prevailing angle perpendicular to the coastline or in a region with small littoral drift. There is no external sediment source in these areas and the shape of coastlines will not change considerably. Coasts in the dynamic equilibrium also have a stable form while the littoral drift is not zero in this condition. In these kinds of bays, if net sediment discharge changes, the coastlines will change. In unstable bays, the equilibrium condition has been ruined due to river activities or construction of new structures. In such situation, the beach rebuilds and adjusts itself to a new equilibrium condition.

Although, these bays are different in size, shape, and hydrodynamic condition, engineers and geologists suggested mathematical equations which can be used for prediction the stable shape of these bays. As the first efforts, [Krumbein, 1944] predicts the stable shape of California coasts using logarithmic spiral equations and [Yasso, 1965] used the same equation for prediction the stable shape of four bays in west and east of American beaches. He concluded that the center of spiral curve is not coincided with diffraction point and the effect of wave characteristics, especially the wave angle is not considered in the above-mentioned equation. Later, [Walton, 1977] concluded that the logarithmic equations did not necessarily present an equilibrium condition. due to the weaknesses of this equation, [Hsu et al., 1989], introduced an equation named parabolic equation based on curve fitting to 27 stable bays including 14 laboratory models and 13 real bays. Their equation can be used to determine the stable shape of the bay. After that, various attempts have been made for introducing a simple and accurate equation. [Moreno, 1999] suggested using hyperbolic models. He evaluated it by investigating 46 bays in Spain and North America. However, the wave diffraction was not considered in their equation. Regarding the existing ambiguities in choosing the wave diffraction point, [Gonzalez, 2001] determined the point of down-drift control through the results of wave energy flux. Later, [Martino, 2003] found the wave diffraction point by trial and error.

Among different proposed equations, the parabolic equations can determine the static shape but they cannot simulate the dynamic behavior of bays. They cannot also consider the effect of wave height and period as well as cross-shore profile and sediment size on final shape of bays. Instead, numerical models can be used for understanding the dynamic behavior of bays. Two dimensional numerical models are good instruments for short time simulations in order of some days; however, they are not appropriate for long-term morphological simulations. [Daly, 2014, 2015] simulated an imaginary bay between two structures with 150m distance from each other for 3 years using Delft3D software, but the simulation time was very long even by applying the speed-up factor. He found that the evolution of a coastline to a stable shape can be predicted well by an exponential function. An alternative to complicated 2D models is One-line model with simplified assumptions about cross shore profile. These models have been used for long time simulation of coastlines [Weesakul et al., 2010; Barkwith et al., 2014a, 2014b]. However, original One-line models with rectangular computational cells can be applied only to the straight parts of a coastline [Pelnard-Considere, 1956] and it is not appropriate for modeling curved coastlines. To address this issue, different modifications have been suggested. [Le Blond, 1972] proposed using the local coordinates so that the coastline can progress in all the directions. later, [Rea and Komar, 1975] introduced a coordinate system based on two independent perpendicular one-line models in which the coastline can progress along both of them. Yet, the mass was not conserved in these models because of the generated gaps between rectangular elements around convex or concave curves. [Kaergaard and Fredsoe, 2013] used polygonal elements to solve this problem. But this method also needed a trial and error which caused inaccuracy of results. In recent years, [Hurst, 2015] proposed a one-line model for simulation of a special kind of bays named crenulate-shaped bays. He showed that the Crenulate-shaped bays can be modeled with reasonable accuracy using the proposed method.

The Crenulate-shaped bays exist in different scales in Mokran coasts of Iran. Any change at the head of these bays can deform their stable shapes. A sample change is construction of a new structure at the heads. In this study, the response of Chabahar and Pozm bays to new constructions is investigated using an empirical model based on parabolic equation (MEPBAY) and a one-line numerical model (COVE). New strategies for decreasing of sedimentation problems and instability of the coastline are also proposed.

2. Numerical and empirical models for morphological simulation of crenulate-shaped bays.

To calculate the long-term coastlines morphological changes, different numerical and empirical models have been presented. Some of them are especially for Crenulate-shape coastlines and some others are useful in any region. Two-dimensional long-term morphological simulations need more execution time and special computers because of the complicated calculations. Therefore, using one dimensional model or simplified equations are more common. One of the most important empirical equations which are still used is parabolic bay shape equation introduced by [Hsu et al., 1989] as:

$$R_n / R_\beta = C_0 + C_1(\beta/\theta_n) + C_2(\beta/\theta_n)^2 \qquad (1)$$

Where, β is the angle between wave crests in diffractions point and the control line $R_\beta . R_n$ is the distance between the control point and coast line along a line with angle θ_n with the wave crest. The control line is a line which connects the wave diffraction point to an optional point in down-drift part. The coefficients C were suggested initially through the curve fitting for 27 cases.

The MEPBAY software can determine the stable static shape of coastline based on the above-mentioned equation in Crenulate-shaped bays. To determine the equilibrium shape of a Crenulate-shaped bay, it is necessary to choose diffraction point and down-drift point correctly in straight part of coastline. Definition of wave diffraction point is easy in MEPBAY. For ease of implementation, MEPBAY is a good instrument for initial assessment of length, location, and layout of a new structure. However, such empirical equations cannot predict the dynamic behavior of bays. In addition, choosing a rough control point and not including some important parameters such as bed slope and wave specifications in empirical methods are some other drawbacks. A solution is using numerical tools for simulations.

LITPACK is a numerical one-line model which is one of the subsets of MIKE software, the product of DHI Company. This software is very flexible to influence all the parameters such as waves and tidal currents and sediment grading specifications. But, it is weak in modeling too curved coastlines. Furthermore, because of using single straight base line and rectangular elements, if a part of coastline has two different values of y-coordination (same as the situation shown in Figure 1), this software cannot be used for predicting the deformation of this coastline. Since the aim of this research is the simulation of crenulate bays with too much curvature, this problem limits using LITPACK.

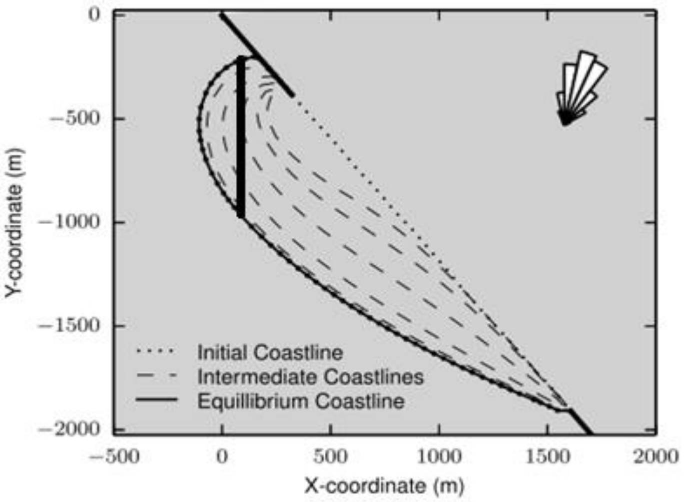

Figure 1: Shortage of the single line models with rectangular elements

Coastal Vector Evolution model (COVE), is another one-line model suitable for simulation of coasts with too much curvature. This model uses the local coordinate system and the form of elements in each area can be triangles, rectangular and trapezoidal based on the coastline curvature. For each element, the lateral boundaries are formed in a way to be perpendicular to the line which connects two adjacent coastal nodes. Coastal elements are formed in trapezoidal shapes in convex parts of the shoreline due to the divergence of boundaries. In concave parts, because of the convergence of boundaries, triangle elements are formed. In this way, the error decreases considerably. The mesh generation procedure used in COVE is shown in Figure 2. To solve the mass conservation equation and to calculate the progress rate of a coastline, equations (2) and (3) are solved in COVE for trapezoidal elements and Triangles/Polygon elements, respectively.

$$\Delta V = a_1 d\eta^2 + b_1 d\eta$$
$$a_1 = \frac{D_{sf}}{2}.\tan(\in_1 + \in_2) \qquad (2)$$
$$b_1 = w_0 D_{sf} + \frac{D_{sf}^2}{2\tan\beta}(\tan\in_1 + \tan\in_2)$$

$$\Delta V = a_2 d\eta^3 + b_2 d\eta^2 + c_2 d\eta$$
$$a_2 = -\frac{1}{6}\tan\beta(\tan\in_1 + \tan\in_2)$$
$$b_2 = \frac{1}{2} w_0 \tan\beta \qquad (3)$$
$$c_2 = A\tan\beta$$

where, w_0 is the width of coastal elements, β is bed slope in front of the coastline, A is the area of the elements and D_{sf} is closure depth. ϵ_1 and ϵ_2 are also used to measure the angle between elements as shown in Figure 2.

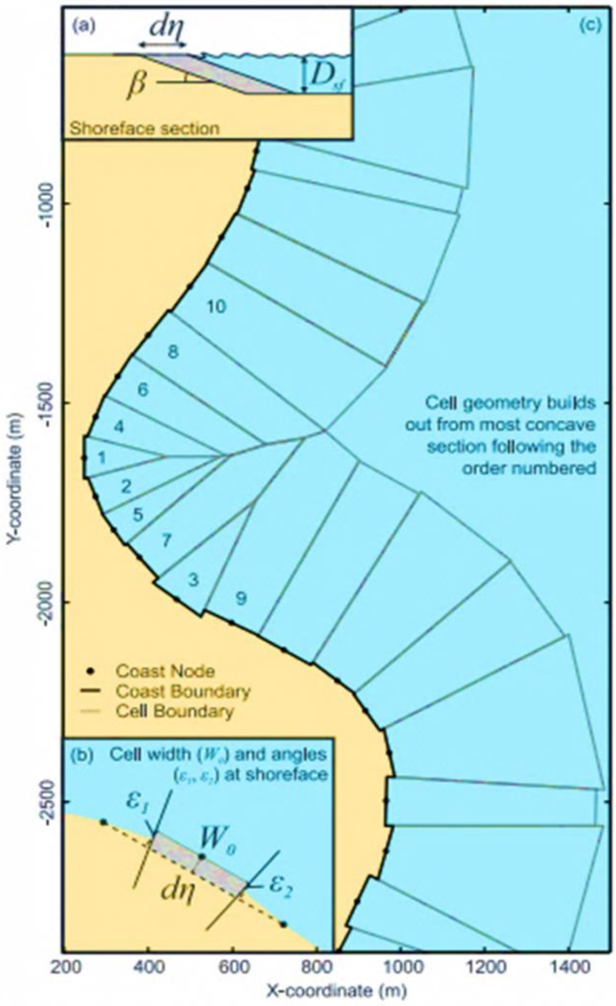

Figure 2: The way of making elements and using parameters in numerical modeling

In this numerical model, an equilibrium condition is calculated supposing that no sediment from the lateral boundaries influence the modeling area. The equilibrium condition happens when the rate of sediment transport parallel to coast is zero in all parts. In other words, the coastline will be stable if waves cannot generate any erosion. If there is a sediment source in the area or sediment exchange through the model boundaries, the equilibrium condition and consequently the equilibrium shape of the bay will be changed. The original version of COVE, is able to predict only the static equilibrium and it is unable to present the dynamic equilibrium condition. The tidal currents cannot be simulated by this model too. But these shortages can be resolved in this open source software. Since the stable shapes of bays are studied in this research, there is no need to such improvements. In table 1, the mentioned models are presented and compared according to their priority and suitability for this research. In this table, number 1 means the most priority and number 3 means the least priority.

Table 1: Evaluation of the presented Modelling

	MEPBAY	COVE	LITPACK
Speed	1	2	3
Accuracy (too much curved coasts)	2	1	3
Stability of Solution	-	1	2
Influencing the entrance parameters (wave, bed and general currents specifications)	3	2	1

Finally, two models of MEPBAY and COVE are investigated in this research. The former is based on empirical equations and the latter one is based on one-line numerical models.

3. Sensitivity of the Numerical Results to Wave Parameters

To determine the effective parameters in the equilibrium shape of bays, a sample case is selected based on the parameters of Chabahar bay with the default input values presented in Table 2. Then, the parameters are changed to investigate their importance. The final shapes of the bay obtained from numerical model are shown in Figure 3.

Table 2: Base values for sensitivity analysis

Parameters	Values
Shore-face Slope	0.0025
Node Spacing	40m
Closure Depth	10m
End time	100 year
Wave Parameters	H_m=1.15, H_{std}=0.35, T_m=6s, T_{std}=3s, MWD_m=28, MWD_{std}=10

As expected and presented in this figure, the prevailing wave angle is the most important factor in determining the stable shape of the coastline. In other words, coastline should conform to the wave direction and therefore, the stable shape of coastline is necessarily a function of dominant wave direction. On the other hand, by increasing the wave height, higher diffracted waves will reach to the shadow area at the back of the bay head. Consequently, the amounts of coastline erosion will be increased at this area and the stable shape of the coastline will be changed. Based on the outcomes, both the wave period and the bed slope can only affect the required time for generation an equilibrium coastline but these parameters do not considerably influence the final stable shape. Therefore, choosing the representative wave height and direction is more important than other parameters.
To simulate the long-term behavior of a shoreline, a representative wave should be considered. Frequency of waves is an important parameter in this regard while waves with permanent specifications govern

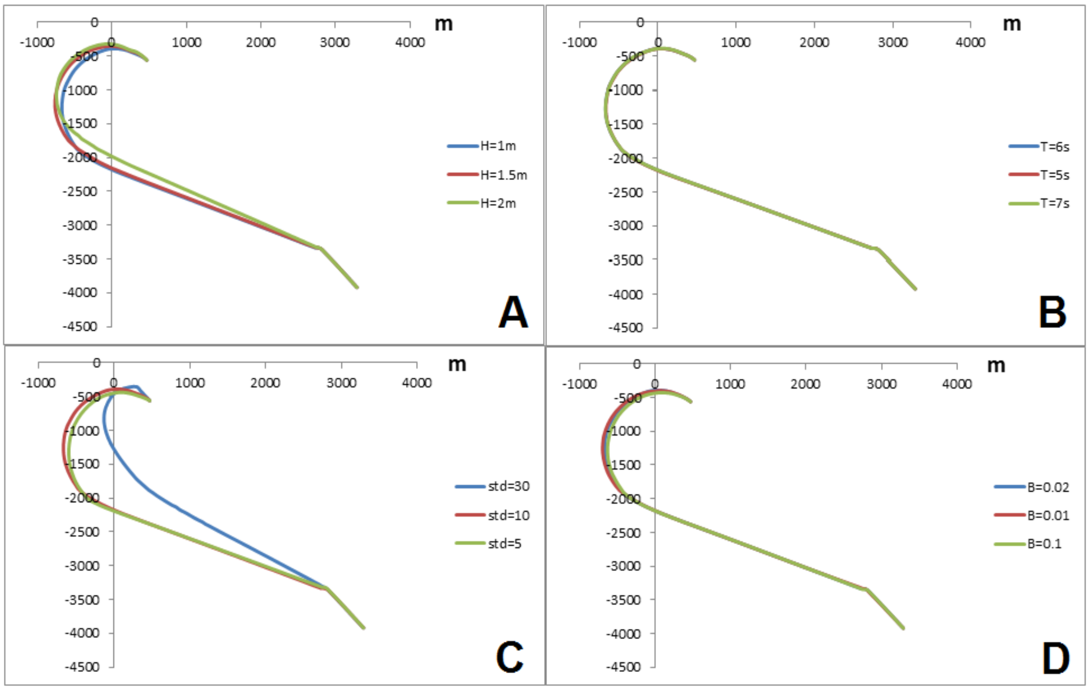

Figure 3: Effect of different parameters on the simulated morphological changes. (A): Wave height, (B): Wave Period, (C): Wave angle, (D): Bed Slope

the bay curved shape. Another factor is the wave potential in sediment transport. The criterion for choosing the representative wave is the well-known analytical sediment equation, CERC. Therefore, the height and direction of the representative wave are calculated as:

$$H_{rep}=\frac{\sum H_i^{2.5}*f_i}{\sum f_i} \qquad \alpha_{rep}=\frac{\sum \sin(2\alpha_i)*f_i}{\sum f_i} \tag{4}$$

4. Model Verification

The numerical model COVE is not evaluated properly in modeling of Iran’s bays. Therefore, it is necessary to test it on several real cases. Two cases are selected in this study as Shahid Beheshti port at the eastern part of Chabahar Bay and Pozm Port in Mokran coasts. These locations are shown with bold lines in Figure 4.

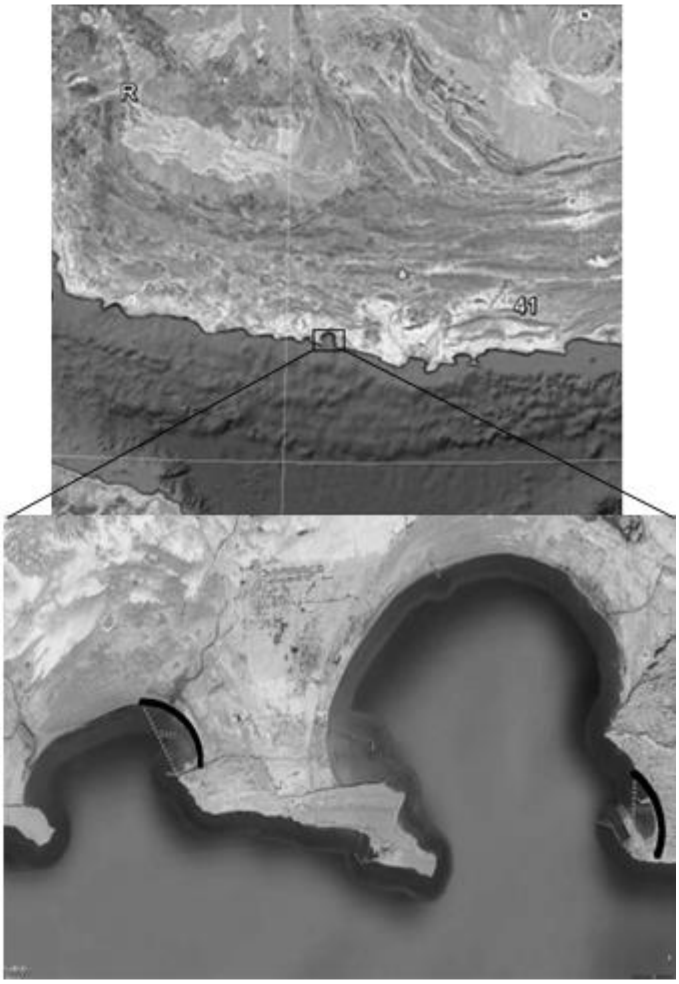

Figure 4- The applicability of COVE in the studied area (Bold lines show the areas which are modeled by COVE).

Since a long duration is required to reach a stable bay, it is assumed that the present shapes of the bays are compatible with the original position of headlands (assuming no new structure at the headlands). On the other hand, the stable shapes of these bays are obtained via both numerical and empirical models assuming no breakwater at the headlands. The results are shown in Figure 5 for Chabahar bay. The circle marks in the figures present the control points at upstream and downstream locations. Although the interior coast of the bay in Figure 5 is nearly consistent with the numerically predicted stable shape, both empirical and numerical models cannot predict well the coastlines close to the headland. However, it seems that the numerical model is generally more accurate for estimating the coastline shape.

To quantify and evaluate the results more accurately, the normal distance between the existing and the modeled coastline is measured and then its averaged value is calculated along the entire coastline to evaluate the amount of errors. Based on these calculations, the errors of the numerical and empirical methods are 11% and 18%, respectively.

The same methodology is performed for the eastern and the western areas of the Pozm bay and the results are presented in Figure 6. Again, the new constructed breakwaters are not considered in predicting the present form of the bay. Therefore, the control points are located by assuming no breakwater at the headlands. As it is observed, two numerical and empirical models have suitable ability in estimating the coastline shape. The errors of numerical and empirical models are 9% and 6.5% for the eastern part and 5% and 4% for the western part of the Pozm bay, respectively. These errors are clearly lower than the calculated values for Chabahar bay. The results also show that the coastlines in the eastern and western parts of the Pozm bay are in a static equilibrium condition.

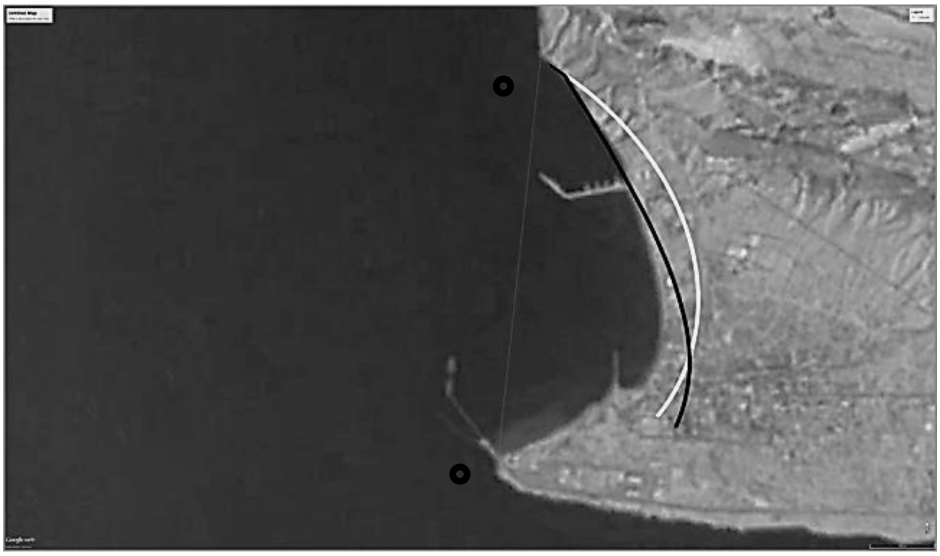

Figure 5- Dynamic equilibrium shape of Shahid Beheshti Port. (White curved line): empirical modelling MEPBAY, (black curved line): numerical model COVE

It can be understood from the results that the two mentioned models can be applied to estimate the stable shape of these bays with a relatively good accuracy. Generally, the numerical model is more accurate than the empirical model; however this is not completely true in the Pozm area where the river can deteriorate the numerical assumptions. Therefore, it is better to use COVE numerical model for investigating the pure crenulate-shaped bays without any significant sediment transportation due to existence of rivers, etc.

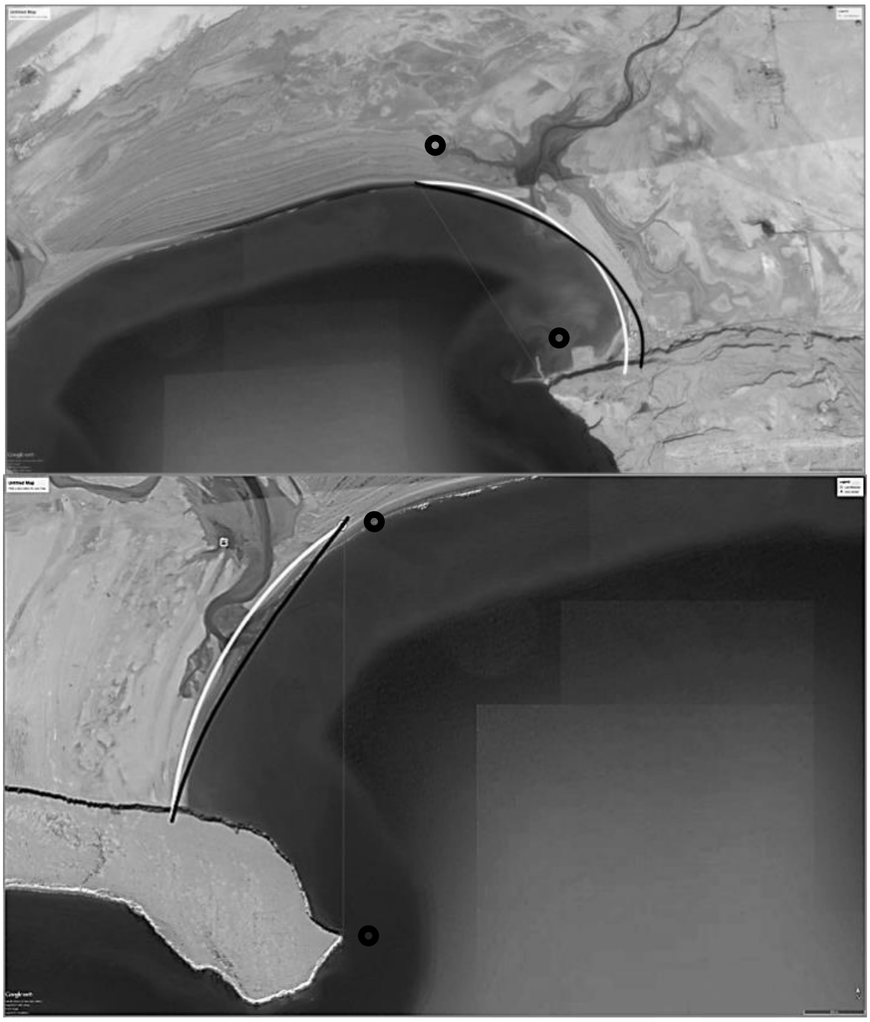

Figure 6- Static equilibrium of Pozm bay. (Up): eastern part, (Down): western part. White curved line shows empirical model results (MEPBAY) and black curved line shows numerical model results (COVE).

Figure 7- Construction of breakwater at eastern part of Chabahar bay. (Left): first construction, (Right): harbor extension.

5. Stable Coastlines around Shahid Beheshti Port

The headland at the eastern part of Chabahar Bay has been changed in two phases as presented in Figure 7. At the first phase, the static equilibrium shape of the coastline has been changed due to the construction of Shahid Beheshti breakwater. In the recent years, this breakwater has been extended during a port development plan. In this research, coastline evolution due to the breakwater extension has been investigated.

Construction and extension of the breakwater at the eastern head of Chabahar bay has changed the location of control points. As a result, the stable shape of the bay has been changed. The numerical model is used for investigating this problem. It should be mentioned that the numerical model considers the influence of the hydrodynamic condition. In addition, the required time to reach a new equilibrium condition can be calculated by this model. Since the wave height and direction are the most effective parameters for estimating the stable coastline shape (as discussed in previous sections), the wave rose of the area (based on ISWM studies) as shown in Figure 8, is used to extract the height and direction of the representative wave.

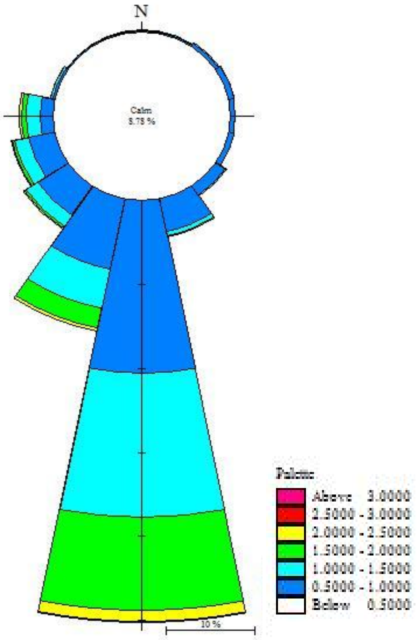

Figure 8- Rose wave ISWM Chabahar area

In the first phase, the position of the eastern headland has been changed to the breakwater head as presented in Figure 9. The new equilibrium condition is shown in figure too.

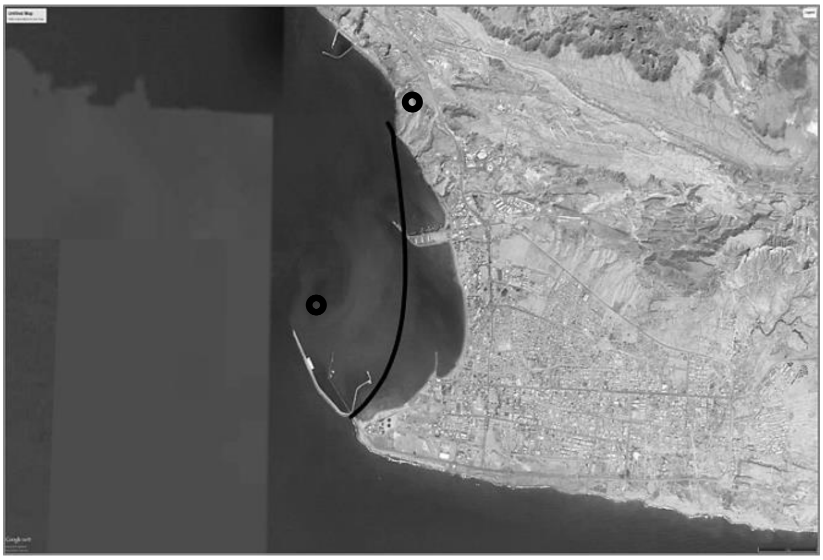

Figure 9- Coastline changes because of primitive construction breakwater

Figure 10- Changes of stable coastline because of port development

Based on the numerical results, the required time to reach this equilibrium condition is predicted about 120 years. In other words, it is anticipated that the coastline reached to its stable shape shown in Figure 9 after 120 years if no dredging performs in the port and no climate change occurs. However, the periodical dredging is an effective factor in the mentioned procedure.

In the recent years, extension of the breakwater has caused some changes in the wave and current circuits around the bay head and consequently, the sediment transport rate has been changed. This creates a new equilibrium conditions as presented in Figure 10 which is estimated to reach this condition in 100 years. New defined control points are clearly presented in this figure.

Based on the results, the stable time has been decreased after port development (from 120 to 100 years). Therefore, it can be concluded that this time is related to the interior distance between the bay heads. This conclusion is completely in agreement with the results reported by Hurst (2015). He studied the coastlines changes in several bays and concluded that the required time for making a stable bay is directly related to the square distance between two headlands. However, it should be mentioned that the wave condition and its diffraction pattern differs after breakwater extension in the development phase of Shahid Beheshti port. This item can also change the required time to reach an equilibrium condition.

It should be emphasized that coastal changes never reached to an exact zero value in the simulations, however, after a long time; the changes become so few that can be neglected. For instance, in Figure 11, the results of coastline changes versus different years have been presented for the port development phase. To protect the clearness of picture, the curved line of the coastline changes are just shown and the background of the port is omitted. As shown in the figure, after 100 years, the coastline is involved in few changes that can be ignored.

The above-mentioned results show that if the basin is not dredged, the coastline tends to develop and reach the calculated stable shape. Meanwhile, this evolution depends on other parameters such as sediment sources and possible erosion of coastal materials. In addition, presence of reclaimed area inside the port basin as well as ship traffic will affect these outcomes.

6. Stable Coastlines Around Pozm Bay

In this part, the stability of the eastern part of the Pozm bay is investigated and the static stable

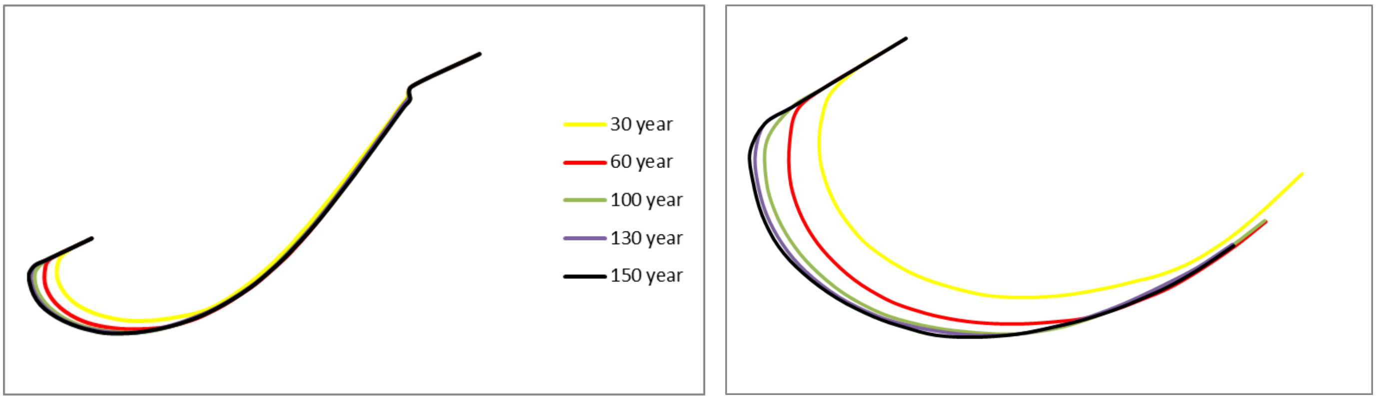

Figure 11- Coastline Evolution for the development phase of Shahid Beheshti port by the time

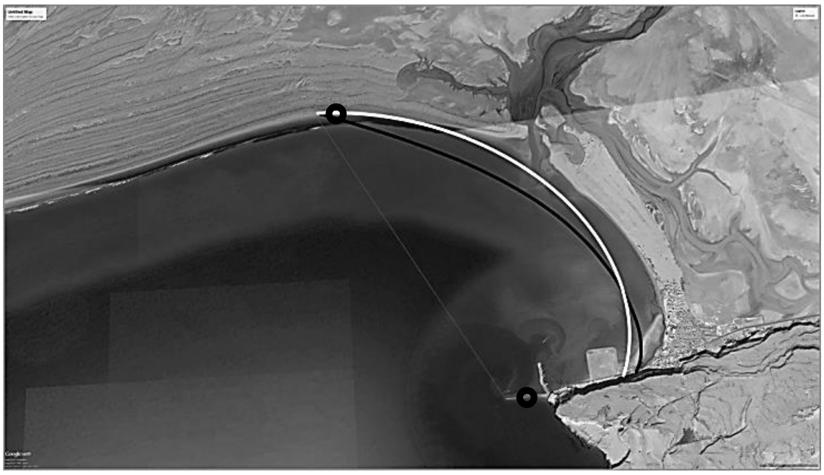

Figure 12- Changes of stable coastline because of breakwater construction along east-west (white curved line): empirical model MEPBAY, (black curved line): numerical model COVE

coastline is calculated by means of both numerical and empirical tools. As discussed in previous sections, the coastline was in an equilibrium condition before port construction (see Figure 4). The location of this headland has been changed in two steps. At first, an east-west breakwater is constructed and then, due to sedimentation problems, a north-south breakwater is designed. After breakwater construction along east-west, a new equilibrium condition as shown in Figure 12 has been created. Through breakwater construction along north-south, the diffraction wave points have been changed again. Meanwhile, as depicted in Figure 13, the new equilibrium condition in this condition is in better conformity with the present coastline.

From the above-mentioned results, it can be concluded that with the new breakwater, the stable coastline in Pozm bay is very close to the current condition and it is anticipated that no intense sediment problem threaten the port.

7. Conclusion

In this research, the stability of two crenulate-shaped bays of Mokran coasts in south-west of Iran is studied. For this purpose, the empirical tool MEPBAY and the numerical model COVE are selected and after verification of these models, they have been applied to study the coastlines of two Chabahar and Pozm bays. These bays are selected since the location of their heads has been changed after breakwater construction. The results of sensitivity analysis show that the wave height and wave angle are the main effective parameters in coastline changes; while the contribution of other parameters such as wave and bed slope is less sensible in the final stable shape. According to the results, any construction at the headlands affects the stable shapes of the bays and it is advised to design a compatible layout with the present form of the bay to minimize unwanted effects. Based on the results, both methods can be applied suitably to predict the equilibrium shape of bays. However, the numerical model because of considering different parameters such as wave height, period, direction and also estimation of the required time to reach a static equilibrium, can be more practical. Its results are also more accurate than empirical outcomes where no additional sediment source exists.

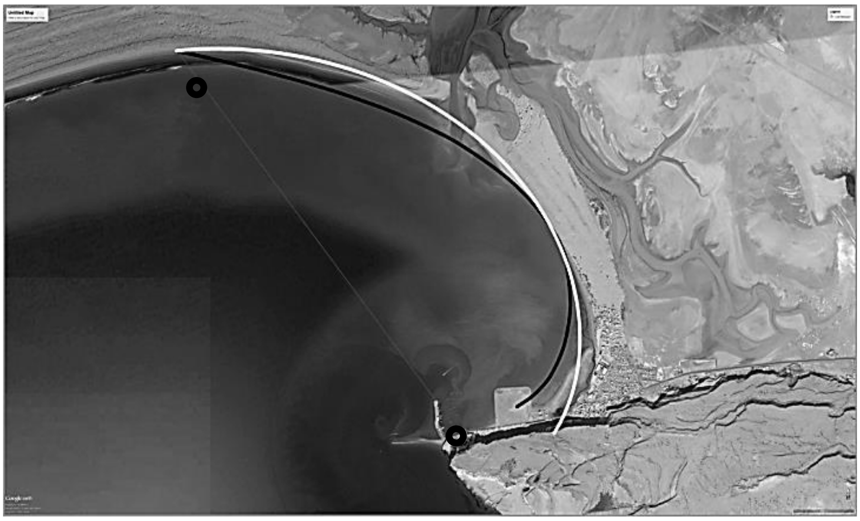

Figure 13- Coastline changes because of breakwater construction along north-south. (white curved line): empirical model MEPBAY, (black curved line): numerical model COVE

8. References

1- Barkwith, A., C. W. Thomas, P. W. Limber, M. A. Ellis, and A. B. Murray (2014a), Coastal vulnerability of a pinned, soft-cliff coastline—Part I: Assessing the natural sensitivity to wave climate, Earth Surf. Dyn., 2(1), 295–308.

2- Barkwith, A., M. D. Hurst, C. W. Thomas, M. A. Ellis, P. L. Limber, and A. B. Murray (2014b), Coastal vulnerability of a pinned, soft-cliff coastline. II: Assessing the influence of sea walls on future morphology, Earth Surf. Dyn., 2(1), 233–242.

3- Daly, C. J., C. Winter, and K. R. Bryan (2015), On the morphological development of embayed beaches, Geomorphology, 248, 252–263,

4- Daly, C. J., K. R. Bryan, and C. Winter (2014), Wave energy distribution and morphological development in and around the shadow zone of an embayed beach, Coastal Eng., 93, 40–54.

5- Gonzalez, M., Medina, R., (2001), On the application of static equilibrium bay formations to natural and man-made beaches, Coast. Eng. 43 (3–4), 209–225.

6- Hsu, J.R.C., Silvester, R., Xia, Y.M., (1989), Generalities on static equilibrium bay, Coast.Eng. 12, 353–369.

7- Hurst, M., & Barkwith, A. (2015), Exploring the sensitivities of crenulate bay shorelines to wave climates using a new vec tor-based one-line model, Journal of Geophysical Research: Earth Surface, 2586-2608.

8- Kaergaard, K., and J. Fredsoe (2013a), A numerical shoreline model for shorelines with large curvature, Coastal Eng., 74, 19–32.

9- Kaergaard, K., and J. Fredsoe (2013b), Numerical modeling of shoreline undulations. Part 1: Constant wave climate, Coastal Eng., 75, 64–76.

10- Kaergaard, K., and J. Fredsoe (2013c), Numerical modeling of shoreline undulations. Part 2: Varying wave climate and comparison with observations, Coastal Eng., 75, 77–90.

11- Krumbein, W.C., (1944), Shore processes and beach characteristics, Technical Memorandum, vol. 3. Beach Erosion Board, U.S. Army Corps of Engineers, p.47.

12- LeBlond, P. H. (1972), On the formation of spiral beaches, Coastal Eng. Proc., 1(13), 1331–1343.

13- Martino, E., Moreno, L., Kraus, N.C., (2003), Engineering guidance for the use of bayed beach formulations, Proc. Coastal Sediments'03. ASCE.

14- Moreno, L.J., Kraus, N.C., (1999), Equilibrium shape of headland-bay beaches for engineering design, Proc. Coastal Sediments '99, vol. 1. ASCE, p.860–875.

15- Pelnard-Considere, R. (1956), Essai de theorie de l’evolution des formes de rivage en plages de sable etde galets, in 4th Journees de l’Hydraulique, Les Energies de la Mer, vol. 3, p.289–298.

16- Rea, P. D., and C. C. Komar (1975), Computer simulation models of a hooked beach shoreline configuration, J. Sediment. Res., 45(4), 866–872.

17- Silvester, R., Hsu, J.R.C., (1997), Coastal stabilization, World Scientific, Singapore, p.578.

18- Walton Jr., T.L., (1977), Equilibrium shores and coastal design, Proc. Coastal Sediments'77, ASCE, p. 1–16.

19- Yasso, W.E., (1965), Plan geometry of headland bay beaches. J. Geol. 73, 702–714

INTERNATIONAL JOURNAL OF
COASTAL & OFFSHORE ENGINEERING

IJCOE Vol.4/No. 1/Spring 2019 (21-29)

Available online at: http://ijcoe.org/browse.php?a_code=A-10-269-1&sid=1&slc_lang=en

Numerical Modeling of Wave and Current Patterns of Beris Port in East of Chabahar-Iran

Mesbah Sayehbani[1*], Danial ghaderi[2]

[1] *Assistant Professor, Department of Marine Engineering, Amirkabir University of Technology, Bandar Abbas, Iran, msaybani@aut.ac.ir*
[2*] *Ph.D. student, Faculty of Marine Science and Technology, University of Hormozgan, Bandar Abbas, Iran; danialghaderi1@gmail.com*

ARTICLE INFO

Article History:
Received: 22 Feb. 2019
Accepted: 22 May 2019

Keywords:
Breakwater
Oman Sea
Beris port
MIKE21

ABSTRACT

The wave and current patterns of the Beris port and its surroundings before and after construction of the breakwater structure was investigated by numerical model, MIKE 21. For this purpose, the required data was provided and the model was prepared for implementation within a month from July 22 to August 21, 2016. In order to verify the modeling results, the extracted data were compared with the data derived from the global wave model; WAVEWATCH III and ECMWF. The simulation results show the significant effect of the breakwater on the stillness of the basin and the change in flow direction. According to the position of the port and the morphology of the coast, is expected to parallels sedimentation caused by waves and currents of the region focused on the long arm breakwaters and adjacent to the entrance mouth of breakwaters, as well as in the coastal part of the small arm of the breakwater.

1. Introduction

The coastal zone is one of the most dynamic regions that are affected by various parameters such as waves, currents and storms. On the other hand, this zone has always been exploited by human beings. In order to manage and control such a region and the structures constructed therein such as ports, hydrodynamic study of the region is essential. In the present study, we have tried to investigate the patterns of wave, current and sedimentation around the Beris Fishing Port in the East of Chabahar Port. Since reliable data and validated sampling are necessary for such studies, it has been tried to study the hydrodynamic conditions of the region by numerical modeling using existing and available data from global atmospheric and wave models.

The wind plays a major role in the formation and propagation of waves, so that ocean waves with different spatial and temporal scales as well as coastal waves are all strongly influenced by wind [1]. Today, the third-generation numerical models allow historical studies and prediction of various water areas. Physical and numerical models are two main methods available for simulating the wave propagation or the interaction between waves and marine structures in the coastal engineering [2]. A calibrated and validated model can be a suitable basis for short- and long term studies [1]. With advances in the field of computers and such numerical models, human knowledge of the waves and currents of the seas have now grown considerably, and this feature can partially resolve the prerequisites of hydrodynamic studies. Nowadays, numerical models are the first step in climate change and energy research. [3]. The wave models can be divided into two distinct categories of ocean waves (large scale) and coastal waves (small scale). While most models can be applied to both large and small amplitude, factors such as limitations in computing, efficiency and accuracy determine their use. Numerical models of ocean known as; WAM [4], WW3 [5], and coastal-like; SWAN [6], MIKE21-SW [7] and TOMAWAC [8]. It should always be noted that its crucial point lies in the evaluation of the model inputs according to its outputs, including boundary conditions and physical parameters such as white capping, wave breaking and bottom friction [9].

One of the main problems of Iranian ports, after construction, is the sedimentation problem that occurs in the entrance of the port and then proceeds to the main basin, which disrupts the vessel traffic and ultimately results in inefficiencies of the ports. A study on the northern coasts of the Gulf of Oman on the wave and current pattern of the Ramin Port (near the study area of this research) was carried out by Isaie Moghaddam et al. 2018, that shows, that coastal currents flow to the port minor basin and form cyclonic genres that contribute in carrying and depositing coastal sediments inside the port basins [10]. Beris port is also facing this problem, and dredging operations with high costs are carried out annually to overcome this problem [11]. Although several studies have already been done on sedimentation in this port, in this research we have tried to study wave and current patterns by numerical model using available data and global models of wind and current, and interpret the sedimentation processes by using the obtained results.

2. Materials and methods

The patterns of wave and current were simulated by using a software package of MIKE21 for the coastal part of the Oman Sea in the vicinity of Beris port, As with other similar studies using this software package [12]. In this numerical simulation by MIKE21/3 Coupled Model FM, the wave module (SW) and the current module (HD) have been used.

2.1 The Study Region

The study area in this research is Beris fishery harbor, located in southeast of Iran, along the northern coasts of the Gulf of Oman at 25.147° N latitude and 61.176° E longitude (figure 1A), This fishing port is located 85 km east of Chabahar city. Beris port is composed of two breakwaters, so that the main breakwater (The big one) is located on the extent of coastal nose along south-north direction, and the subsidiary breakwater (The small one) has been constructed along east-west direction. figure 1B shows the coastline changes around the port of Beris during 1994 and 2016, With the visual interpretation of aerial images, well-defined areas affected by sedimentation. It is therefore predictable that the major sediment is in the subsidiary breakwater (The small one).

2.2 Numerical model

Among the most popular numerical models for analyzing the phenomena governing the marine environment, the MIKE mathematical model developed by the Danish Hydraulic Institute is well-known and widely used software [7]. This modeling software has the capability of simulating phenomena in one, two and three dimensions in all aquatic environments, including estuaries, coastal areas, seas and oceans [4]. Various features of this numerical model for receiving input data in a wide range and providing graphical outputs suitable for research and engineering needs make it an appropriate tool for simulating and analyzing phenomena such as wave and current patterns, sedimentation and erosion in coastal regions, and determining the transfer rate of coastal sediments [13]. In this study, the SW and HD modules of MIKE21 software package was used to simulate wave and current patterns.

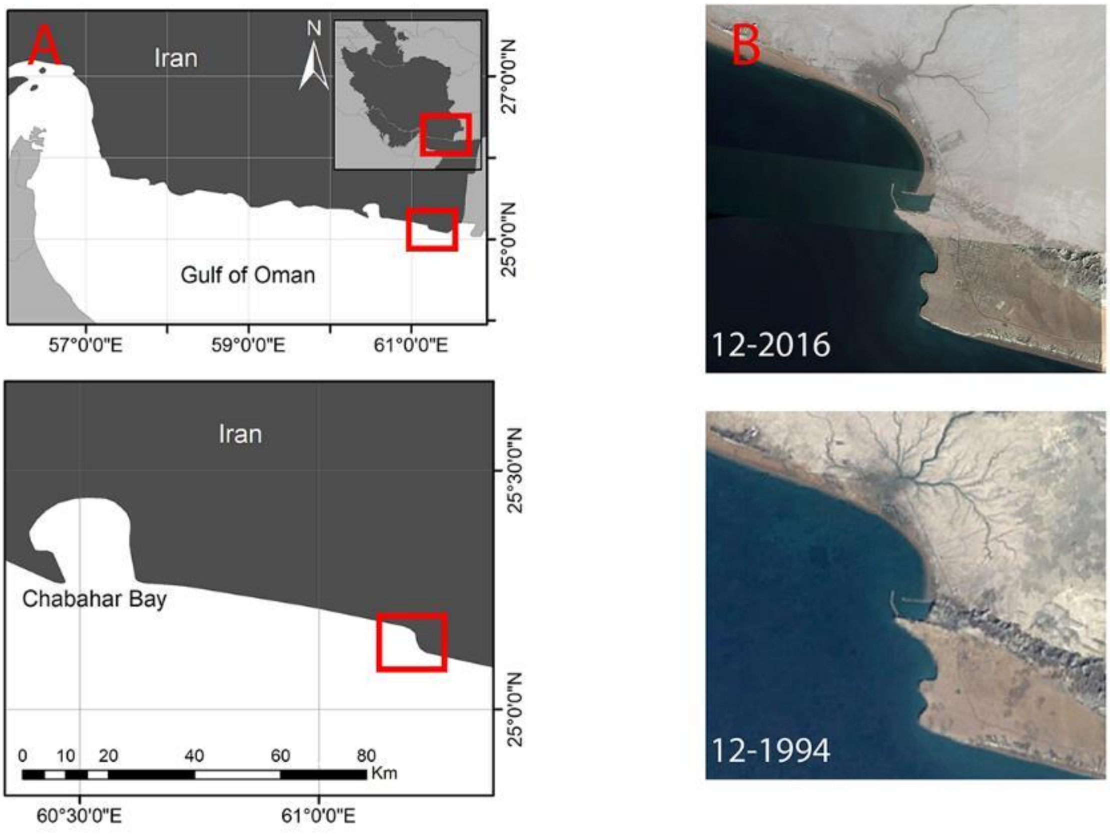

Figure 1: A: Location of the Beris Port, relative to Iran and the Gulf of Oman.
B: Aerial view of the Beris fishing port during 1994-2016

Table 1: The selected domain and its specifications for numerical modeling

Mesh	Mesh environment	Latitude (N)	Longitude (E)
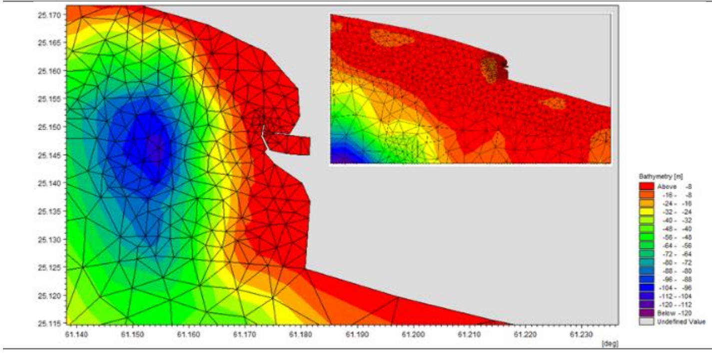	1	24.84495	60.59340
	2	25.29640	60.59340
	3	25.29640	61.37414
	4	24.84495	61.37414
	Nodes/ Elements	2030/3789	

Therefore, according to the region under study, a region with the specifications listed in Table 1 was selected for simulation. This region was discretized to 2030 nodes and 3789 elements using an unstructured mesh, which was made up of coarser mesh in the zone far from breakwater and finer meshes in the zone near the breakwater (Table 1). Using a coarser mesh in the overall domain of the model is to reduce computational time. To create bathymetry file, the topography data of SRTM + 30 version 6.0 was used, which is referred to USGS EROS institute [14]. Also, the study region has 4 boundaries, so that the northern boundary is considered as land border and the eastern, western, and southern boundaries as water borders.

In the hydrodynamic module, tidal data in the form of water level were introduced as boundary data for the western boundary of the model (figure 2). For eastern and southern boundaries, a fixed value was used because of the absence of a measurement station. Also, for the spectral wave model, the first wave level parameter (Wave parameters (version 1)) was used at all three boundaries. In order to apply the atmospheric conditions to the region, the ECMWF-ERA40 wind data has been used (figure 2), so that the wind speed and direction data from July 22, 2016 for one month was considered for the entire study region in a form of a file with a three-hour time step. In order to study the wave and current conditions of the region, first the numerical model was implemented without the presence of the breakwater, and the model was calibrated in comparison with the data of WW3 and ECMWF global wave models by using the parameters of white capping, wave breaking and bottom friction. It should also be noted that in order to create close-to-reality conditions, the wave-current coupling was used in the simulations. After the model was appropriately calibrated, it was implemented in the presence of the Beris' breakwater. In Table 2, the input parameters of the model are expressed.

WW3 global wave model is a prediction model with a 0.5 degrees accuracy, which is available by the University of Hawaii based on the GFS wind data with one-hour time step from 2010. The WW3 is an open source model developed by NOAA and NCEP [15], which is well validated for deep water and widely used around the world [16]. It is also used for nearshore areas [17].

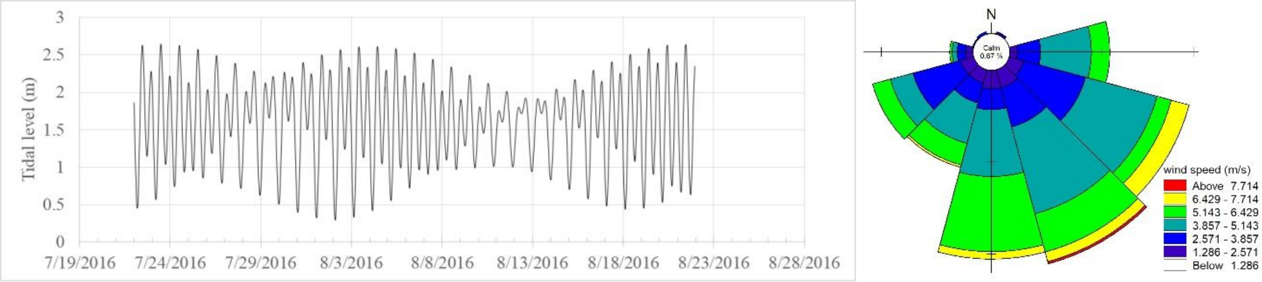

Figure 2: The water level data of Chabahar port and wind roses of the region, extracted from ECMWF-ERA40

Table 2: Parameters used in modeling of the study region

Module	Applied in this investigation	Equations	#
SW/HD	1 Spectral formulation-fully spectral formulation 2 Time –unsteady formulation	Basic Equations	**1**
SW	Dissipation coefficient (cdis=4.5 and Delta=0.5)	White capping	**2**
SW	Gamma data with the value of 0.8 The calibration constant factor,(alpha= 1)	Wave breaking	**3**
SW	Nikuradse roughness =0.04	Bottom friction	**4**
SW/HD	Quadruplet-wave interaction	Energy transfer	**5**
SW	Data from ECMWF institute	Wind forcing	**6**
HD	Tidal level of Chabahar Port	Water level conditions	**7**
SW/HD	SRTM+30	Bathymetry	**8**
HD	The Smagorinsky formulation= 0.28	Eddy viscosity	**9**
HD	Wave Radiation	Wave Radiation	**10**
HD	Chezy number= 32	Bed Resistance	**11**

2.3 Verification of the numerical model

In order to verify the present model, the results of the model were compared with WW3 and ECMWF wave model data at geographic coordinates of 61° E longitude and 25° N latitude [17; 18]. Using calibration coefficients, the numerical results have been tried to be more consistent with the two basic models. As shown in Table 3, in four steps of implementation of the model with the white capping coefficients of 4.5 and 2 and wave breaking coefficients of 0.8, 1, and 0.5, The model with code 1 has the lowest error percentage relative to data of WW3 model as well as ECMWF model. Given the bias statistical index indicating the difference between the mean of the baseline data and the output data of the model (the closer to zero, the higher the accuracy of the model), the index for the model with code 1 has a smaller value than the other models, compared to WW3 and ECMWF models [19]. Also, the model with code 1 shows a better treatment in term of Root Mean Square Error and scatter index , indicating the dispersion rate of the variables relative to the baseline variables and the absolute dispersion of the two variables, respectively. The results of model with code 1 (RUN1) compared with global model data have been shown in figure3. WW3 and ECMWF data are in agreement together, But RUN1 is different. The reason for this difference is the larger mesh in the area, due to the distance from the studied port in order to save time, the model computing network is considered to be larger.

Table 3: Statistical Indicators for verification of the model with different coefficients, against global wave models

	Run1 White Capping =4.5 Wave Breaking =0.8	Run2 White Capping =2 Wave Breaking =0.8	Run3 White Capping =2 Wave Breaking =1	Run4 White Capping =2 Wave Breaking =0.5
% Error WW3	2.16	5.18	6.35	6.24
% Error ECMWF	3.82	6.89	8.08	7.97
Bias WW3	-0.041	-0.100	-0.122	-0.120
Bias ECMWF	-0.072	-0.130	-0.153	-0.151
RMSE WW3	0.280	0.300	0.292	0.299
RMSE ECMWF	0.207	0.241	0.239	0.240
SI WW3	14.52	15.57	15.15	15.54
SI ECMWF	10.74	12.52	12.43	12.45

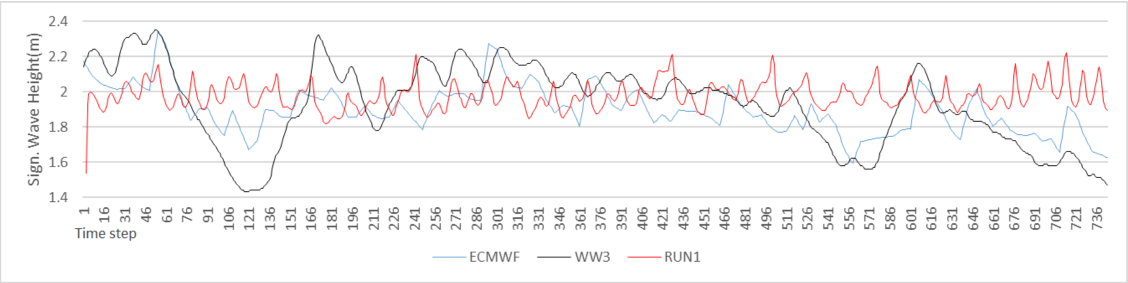

Figure 3: The results of model with code 1 (RUN1) compared with global model data, WW3 and ECMWF

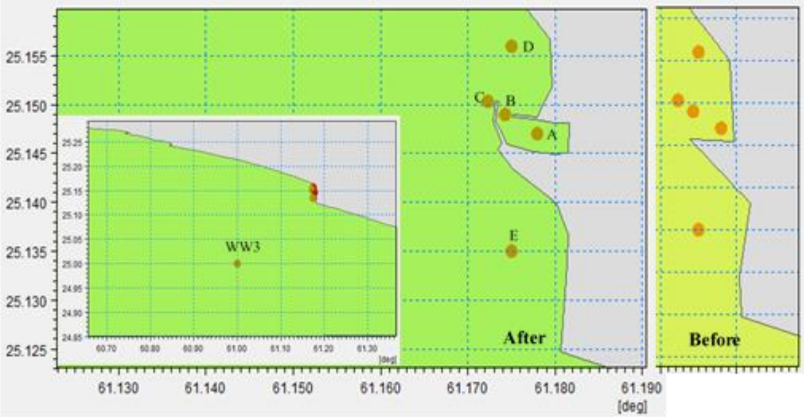

Figure 4: The position of the selected points for comparison of results of model.

3. Results

In order to examine the model of the study region, five points were selected within the basin, at the mouth of the port, behind the major arm of the port, and at upstream and downstream of the port (figure 4). The coordinates of the selected points shown in table 4. After extraction of the data at these points, the necessary analyzes have been done to determine the wave and current patterns as well as prediction of the sedimentation pattern.

3.1 Results of SW model

A view of the overall direction of wind-generated waves in the study region is shown in figure 5. According to this figure, the dominant direction of wind-generated waves is from southwest, as expected.

Diagram of wave heights and Wave roses have been extracted in five-point that shon in figure 6 and table 5. As it is obvious, at the points A and B, which are respectively located within basin and mouth of the port, the wave height has significantly decreased compared to non-presence of the breakwater arm. At point A, the wave height in the absence of the breakwater arm is equal to the average value of 0.62 m and maximum value of 0.8 m, while the average value of wave height in the presence of breakwater arm is 0.01 m. Also, at the point B, the average wave height is 0.68 m, and it reaches to 0.05 m after construction of the port. The wave direction has also significantly changed due to the construction of the Beris port of, so that, in the normal conditions, the wave directions are often from the southwest, and after the construction, they are from the mouth of the breakwater as the only way (Table 5).

In the area behind the breakwater arm (point C), the wave height is about 0.95 m. After the construction of the port, only the dissipation rate of the high velocities has decreased (Table 5).

The wave height at the point D, located outside and at the upper part of the port, a 10.8 percent drop in wave height is observed after the presence of the Beris breakwater and reached to and average height of 0.7 after construction of the port. Also, the wave direction in this area is slightly shifted from southwest to the west, indicating the transport of the sediment particles to the back of the minor arm of the Beris breakwater.

At the point E which is located away from the port, as expected, no change was created in the height and direction of the waves by constructing the port, and the average wave height is about 1.3 m.

Table 4: The coordinates of the selected points for extracting the data from the model and comparing it with the data of the global wave model

Output of points	Latitude (N)	Longitude (E)
WW3/ECMWF	25	61
A	25.147	61.178
B	25.149	61.1743
C	25.1503	61.1723
D	25.156	61.175
E	25.135	61.175

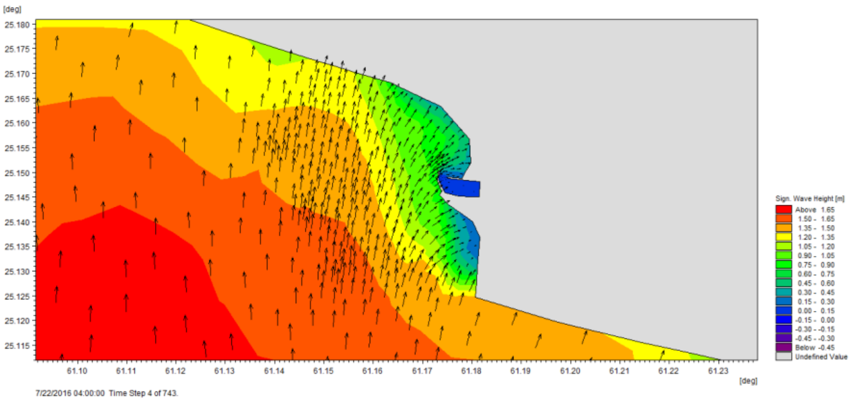

Figure 5: The dominant direction of wind-generated waves near the fishing port; results of SW model

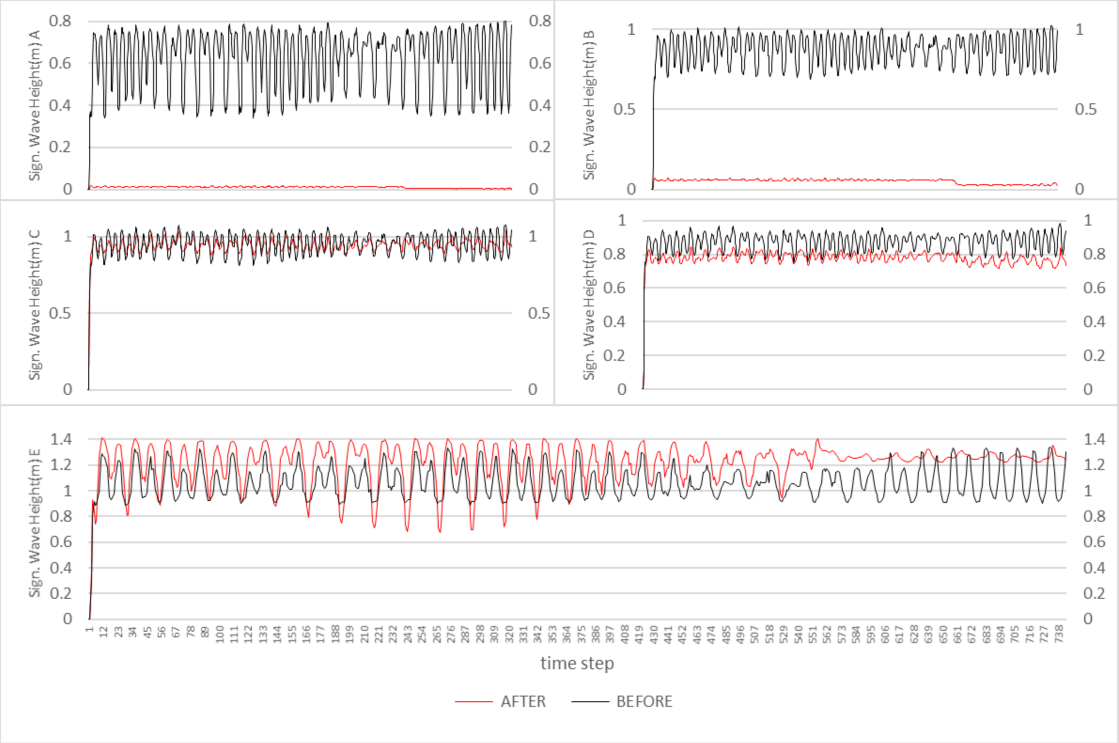

Figure 6: Diagram of wave heights at the five selected points of the port and its surroundings, before and after the construction of the port; results of SW model

Table 5: Wave roses of the selected points of the port and its surroundings, before and after the construction of the port, results of SW model

Point A		**Point B**	
After	Before	After	Before
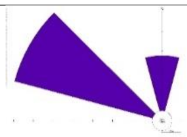	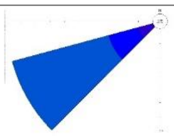	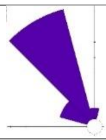	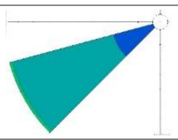
Point C		**Point D**	
After	Before	After	Before
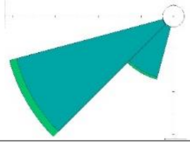	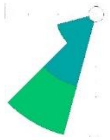	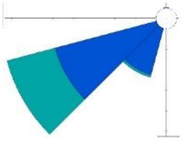	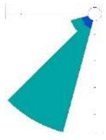
Point E		**Color Legend**	
After	Before		
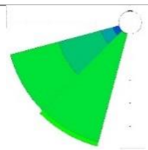	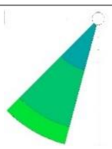	Wave height (m) 🟦 0.8 - 1.0 🟦 0.6 - 0.8 🟦 0.4 - 0.6 🟪 0.2 - 0.4 🟪 0.0 - 0.2 ☐ Below 0.0	🟥 Above 2.2 🟧 2.0 - 2.2 🟨 1.8 - 2.0 🟩 1.6 - 1.8 🟩 1.4 - 1.6 🟩 1.2 - 1.4 🟩 1.0 - 1.2

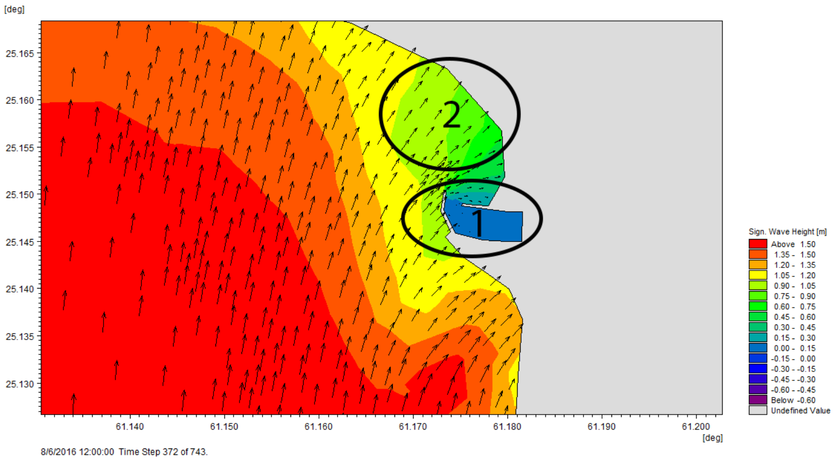

Figure 7: A view of the patterns of wave height and direction around the Beris port; results of SW model

As noted earlier, the direction of dominant waves is from the southwest. This is well illustrated in figure 7, which is related to the time step 372 of the model. According to the figure, the wave height in the port is noticeably low, as expected (the zone 1 in figure 7). Another point to note is that the wave height decreases in the upstream of the port (the zone 2 in Fig. 7), which reduces the water turbulence and therefore can provide a good environment for deposition of sediments.

3.2 Results of HD model

A view of the overall current direction in the Beris port and its surroundings has been shown In figure 8. Accordingly, the dominant current direction is from east to west, which is consistent with the current pattern of the Persian Gulf and Oman Sea. With respect to the coastal morphology, the current direction is changed to be along the coast after reaching the Beris port, and flow includes small circulations and vortices during crossing the Beris breakwater and its upper part (point D).

The results of the HD model representing the current speed are shown in Table 4. As can be seen, at the point A and B, after the construction of the port, the current speed has decreased by 84.3 and 52.4%, and reached from average values of 0.4 m/s and 0.6 m/s to 0.006 m/s and 0.02 m/s respectively.

In the zone behind the breakwater arm (point C), the change in current speed is about 11% and the average speed reaches from 0.05 m/s to 0.06 m/s, which shows the effect of breakwater on the current speed of this area. Also, some vortices forms in this area after the construction of the port and the breakwater arm.

At point D, located in the upper part of the port, the change in current speed is about 27.8% and a decrease from 0.09 m/s to 0.05 m/s is observed.

At point E, unexpectedly, the current speed is increased from an average value of 1.4m/s to 2.6 m/s after construction of the port. Although this increase is unexpected, it can be due to the changes in computational mesh after the inclusion of the port and its arms in the numerical model.

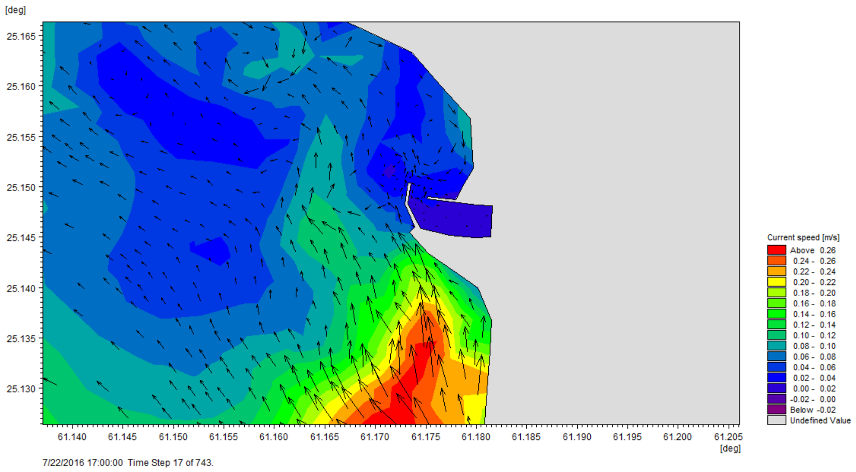

Figure 8: The dominant current direction near the fishing port; the results of HD model

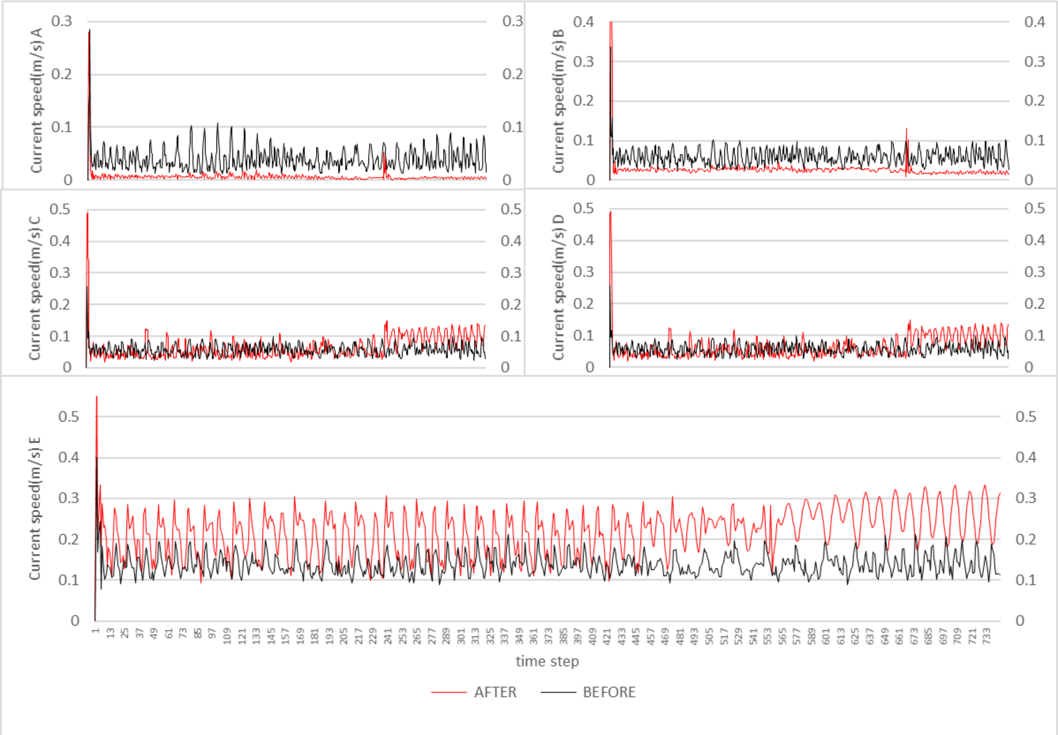

Figure 9: The diagram of current speed at the five selected points of Beris port and its surroundings, before and after construction of the port; results of HD model

The current direction in the study region is toward the west (figure 9), and as seen in figure 10, around Beris port, the current direction is parallel to the coast and toward the head of breakwater (the zone 3 in figure 10). In this region, the current speed decreases rapidly, and some vortices are also formed behind and at the head of the breakwater arm due to the existence of this arm. Inside the port and the inner basin, due to the presence of primary and secondary arms of breakwater, the current speed is extremely low, as shown in the part 1 of figure 10. Another important region is the zone 2 in figure 10, in which the current is often accompanied by a clockwise rotation due to the structure of the coast and the construction of the Beris port. This current has a higher speed at northern part of zone 2 and a lower speed at southern part of zone 2 which is located in the vicinity of the mouth of breakwater.

4. Conclusion

According to the obtained results of wave and current patterns around the Beris fishing port and analysis of these results, one can get an understanding of the general pattern of sedimentation in this port. Also, the present model and verification method used are in a good agreement in comparison with the other studies carried out on this port.

The construction of the Beris breakwater has caused the wave height to decrease in the upper part of the port and the wave directions, which are often from the southwest, to be slightly oriented toward west and guided to the behind of the minor arm of breakwater.

Consequently, suitable conditions for penetration of sediments to the region located in the vicinity of the mouth of breakwater are provided. Also, there is a

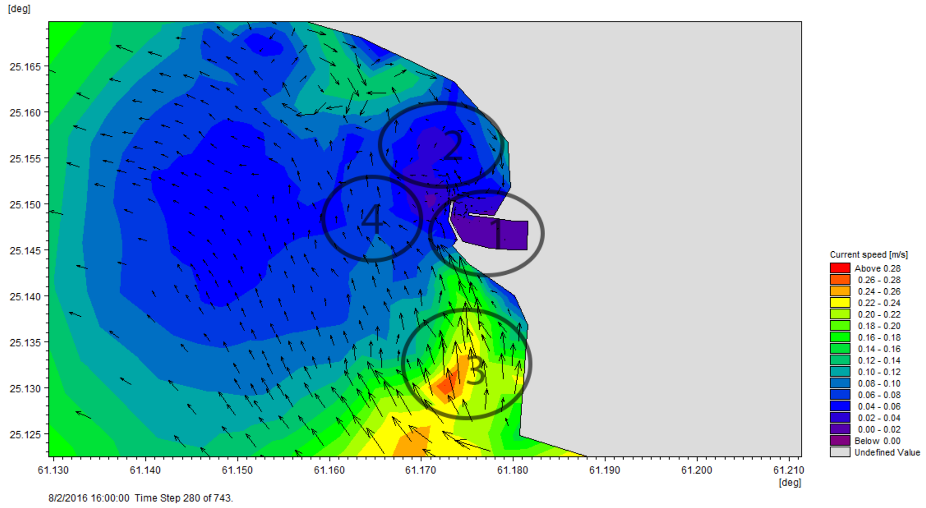

Figure 10: A view of current speed and direction around the Beris port, results of HD model

clockwise current in this region that can transport sediments to the behind of the minor arm of breakwater. Due to the low current speed in this region, a considerable amount of sediment is accumulated in the long run. This issue can be confirmed by comparing satellite images from previous years.

In the region behind the major arm of breakwater, the current speed is generally increased in comparison with the absence of a breakwater, which indicates the effect of this structure on the current pattern of the region. The current speed is higher at the lower part of the Beris port and is parallel to the coastline toward the behind of the major arm. This speed is suddenly drops and causes all sediments, transported to the lower part of the port, have the opportunity to be deposited behind the major arm of Beris port. Therefore, the port encounters a sediment problem at the head of the breakwater, which this sediment can then be transferred into the basin.

5. Acknowledgments

In this way, the authors of the paper express their gratitude and appreciation for the Management of Hydrographic and Tidal Iran Mapping Organization, for the use of the tidal data and the University of Hawaii for the use of world wave model data, WW3.

References

1- Reguero, B. G., Losada, I. J., & Méndez, F. J. (2015). *A global wave power resource and its seasonal*, interannual and long-term variability. Applied Energy, 148, 366-380.

2- Yang, Z. W., Liu, S. X., & Li, J. X. (2014). *An improved coupling of numerical and physical models for simulating wave propagation*. China Ocean Engineering, 28(1), 1-16.

3- Janssen, P. A. (2008). *Progress in ocean wave forecasting*. Journal of Computational Physics, 227(7), 3572-3594.

4- Komen, G. J., Cavaleri, L., Donelan, M., Hasselmann, K., Hasselmann, S., & Janssen, P. A. E. M. (1996). *Dynamics and modelling of ocean waves*. Dynamics and Modelling of Ocean Waves, by GJ Komen and L. Cavaleri and M. Donelan and K. Hasselmann and S. Hasselmann and PAEM Janssen, pp. 554. ISBN 0521577810. Cambridge, UK: Cambridge University Press, August 1996, 554.

5-Tolman, H.L., 2014. W.I. development Group. *User manual and system documentation of WAVEWATCH III version 4.18 [No. 316]*. U. S. Department of Commerce National Oceanic and Atmospheric Administration National Weather Service National Centers for Environmental Prediction 5830 University Research Court College Park, MD 20740: Environmental Modeling Center Marine Modeling and Analysis Branch.

6- Delft, T. (2014). *SWAN User Manual Cycle III version 41.01*. Delft, Nederlands: Delft University of Technology Faculty of Civil Engineering and Geosciences Environmental Fluid Mechanics Section.

7-DHI. MIKE21. 2014. http://www.mikebydhi.com/products/mike-21.

8-Tomawac, 2014. *TOMAWAC wave model*, http://www.opentelemac.org/index. Php/modules-list/20-tomawac.

9- Rao, Y. H., Liang, S. X., & Yu, Y. X. (2012). *A method to determine the incident wave boundary conditions and its application*. China Ocean Engineering, 26(2), 205-216.

10- Moghaddam, E. I., Allahdadi, M. N., Hamedi, A., & Nasrollahi, A. (2018). *Wave-induced Currents in the Northern Gulf of Oman: A Numerical Study for Ramin Port along the Iranian Coast*. American Journal of Fluid Dynamics, 8(1), 30-39.

11- Ardani, S., & Soltanpour, M. (2015). *Modelling of sediment transport in Beris fishery port*. Civil Engineering Infrastructures Journal, 48(1), 69-82.

12- Pakhirehzan, M., Rahbani, M., & Malakooti, H. (2018). *Numerical Study of Winter Shamal Wind Forcing on the Surface Current and Wave Field in Bushehr's Offshore Using MIKE21*. IJCOE 2018, 2(2); p. 57-65.

13- Lavidas, G., & Venugopal, V. (2018). *Application of numerical wave models at European coastlines: A review*. Renewable and Sustainable Energy Reviews, 92, 489-500.

14- Becker, J. J., Sandwell, D. T., Smith, W. H. F., Braud, J., Binder, B., Depner, J. L., ... & Ladner, R. (2009). *Global bathymetry and elevation data at 30 arc seconds resolution: SRTM30_PLUS*. Marine Geodesy, 32(4), 355-371.

15- Badiei, P., & Siadat Mousavi, M. (2010). *The Third Generation Spectral Wave Model, WAVEWATACH-III, Enhanced for use in Nearshore Regions*. Civil Engineering Infrastructures Journal, 44(2), 289-302.

16- Jouon, A., Lefebvre, J. P., Douillet, P., Ouillon, S., & Schmied, L. (2009). *Wind wave measurements and modelling in a fetch-limited semi-enclosed lagoon*. Coastal engineering, 56(5-6), 599-608.

17- Smith, J. M., Hesser, T., Roland, A., & Bryant, M. (2018). *VALIDATION OF UNSTRUCTURED WAVEWATCH III FOR NEARSHORE WAVES.* Coastal Engineering Proceedings, 1(36), 55.

18-Sanil Kumar, V., & Muhammed Naseef, T. (2015). *Performance of ERA-Interim wave data in the nearshore waters around India*. Journal of Atmospheric and Oceanic Technology, 32(6), 1257-1269.

19-Mahjoobi, J., Etemad-Shahidi, A., & Kazeminezhad, M. H. (2008). *Hindcasting of wave parameters using different soft computing methods*. Applied Ocean Research, 30(1), 28-36.

INTERNATIONAL JOURNAL OF
COASTAL & OFFSHORE ENGINEERING
IJCOE Vol.4/No. 1/Spring 2019 (31-40)

Available online at: http://ijcoe.org/browse.php?a_code=A-10-269-1&sid=1&slc_lang=en

Application of Soft Computing in Forecasting Wave Height (Case Study: Anzali)

Mohammad Akbarinasab[1], Iman Esmaili Paeen Afrakoti[2*]

[1]*Assistance Professor, Department of Physical Oceanography, Faculty of Marine Science, University of Mazandaran, Babolsar Mazandaran province, Iran; m.akbarinasab@umz.ac.ir*
[2]** Corresponding author: Assistance Professor, Faculty of Engineering & Technology, University of Mazandaran, Pasdaran Street, Babolsar, Iran;* i.esmaili.p@umz.ac.ir

ARTICLE INFO

Article History:
Received: 7 May 2019
Accepted: 16 Jun. 2019

Keywords:
Soft computing techniques
Wave height
Caspian Sea
Prediction

ABSTRACT

Wave height forecasting is very important for coastal management and offshore operations. In this paper, the accuracy and performance of three soft computing techniques [i.e., Multi-Layer Perceptron (MLP), Radial Basis Function Neural Network (RBFNN) and Adaptive Neuro Fuzzy Inference System (ANFIS)] were assessed for predicting significant wave height. Using different combinations of parameters, the prediction was done over a few or a two days' time steps from measured buoy variables in the Caspian Sea (case study: Anzali). The data collection period was from 03.01.2017 to 06.01.2017 with 30-minute intervals. The performance of different models was evaluated with statistical indices such as root mean squared error (RMSE), the fraction of variance unexplained (FVU), and coefficient of determination (R2). Different simulations of performance assessment showed that the ANFIS techniques with requirements of past and current values of atmospheric pressures and height waves has more accuracy than the other techniques in the specified time and location. Meanwhile, in high lead times, the friction velocity decreases the accuracy of wave height forecasting.

1. Introduction

Wave prediction is essential for engineering applications, understanding sediment movement in coastal area and wave energy harvesting. Different approaches have been used for wave height estimating such as Empirical models, Numerical models, and Soft computing techniques. Empirical methods, which are fast and simple, have been developed for primary wave prediction, SMB [1,2], Shore Protection Manual (SPM), Coastal Engineering Manual (CEM) [3], JONSWAP, and SPM [4] . Among the numerical models, we should reference Wave Analysis Model (WAM), which is used primarily for deep-water conditions [5] SWAN that is used mainly for shallow water region [6] etc. Numerical models are generally more accurate than the empirical methods; but, costly and time-consuming [7]. Despite the long history of numerical and empirical models, previous studies have shown that these models have some disadvantages like time-consuming. Implementation of these models requires various parameters such as topography, whitewash, and wind data. Soft computing approaches are introduced as a convenient technique regarding disadvantages of numerical models. Different soft computing techniques, available to develop wave forecasting models, are Artificial Neural Network (ANN) [8; 9;10;11;12;13;14], Multi-Layer Perceptron (MLP), Radial Basis Function Neural Network (RBFNN), Adaptive Neuro Fuzzy Inference System (ANFIS), Genetic programming, regression trees [15;16], Support Vector Machine (SVM) and etc. Many studies have been carried out to predict wave height using soft computing techniques. The friction velocity (u*) is one of the most effective parameters in this issue [17; 8]. The main objectives of this article are as follows:

- Comparison of three methods (MLP, RBFNN and ANFIS) of soft computing techniques to predict wave height and choosing the best method for wave height forecasting.
- Investigation various combinations of effective parameters on wave height prediction.

The paper is organized as follows. Section 1, the mentioned three soft computing techniques, MLP, RBFNN, and ANFIS; are used to train models based on the observed data from a wave buoy. In section 2, the observed data are analyzed and a brief definition for the three soft computing algorithms is represented. In section 3, the study area is defined, combinations of the employed models are mentioned and the models are trained to forecast the wave height in 3 h, 6 h, 12 h, 24 h and 48h based on the observed data. The results of different models are compared in section 4 and finally the discussions of the results are conducted in section 5.

2. Materials and methods

Three different soft computing technologies are used in this study to forecast wave height in the Caspian Sea (Anzali). A brief description of each method is presented as follows.

2.1 Multi-layer perceptron (MLP)

MLP is a kind of artificial neural network which is inspired from human biological brain system. The basic processing element of MLP is called the perceptron neuron which implements a nonlinear type (usually sigmoid) activation function. Each MLP network consists of different layers which are aligned in a feed-forward structure and the data flows in the network through the synaptic weights between neurons. In Figure 1 a general structure of a MLP network is shown.

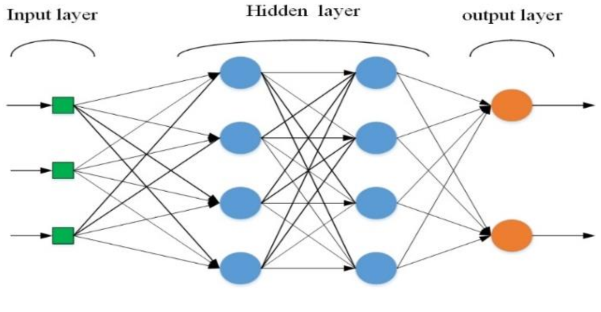

Figure 1. Structure of MLP algorithm

The MLP structure consists of at least 3 layers, input, hidden, and output layer. The input layer receives the value of input variables, hidden layer increase the computation ability of network for non-linear systems and output layer delivers the value of the systems output. MLP is a powerful algorithm in solving a nonlinear supervised problem. The synaptic weights should be computed in the training phase of the algorithm. The back-propagation algorithm is being used for training the network. Applying the training data using back-propagation algorithm the synaptic weights will be set in the training phase, in the modeling phase, applying the test data to the inputs of network will result in the systems output value on the relevant output neuron.

In this paper, 70 percent of data was used for training the network and the other 30 percent was used for testing the algorithm. The network is chosen with three layers, input layer with different number of neurons depends on the chosen model, hidden layer that its neuron number is chosen with a statistical procedure and output layer with a single neuron.

The transfer function used for the hidden layer is a logarithmic sigmoid function and a pure-line transfer function used for the output node.

2.2 Radial basis function neural network (RBFNN)

2.2.1 Radial basis function

Broomhead and Lowe proposed the RBF neural networks in artificial neural network literature [18]. RBF have shown its efficacy as a soft-computing algorithm in many applications such as function approximation [19], data classification [20], system control [21] and etc.

Input layer, hidden layer and output layer are the main elements of the RBF structure. Input layer receives the inputs of the system to the hidden layer. In the hidden layer a multivariate Gaussian activation function applying to inputs from input layer neurons. The output of the algorithm is being computed based on linear combination of the neurons outputs in hidden layer. The structure of a typical RBN network is shown in Figure 2.

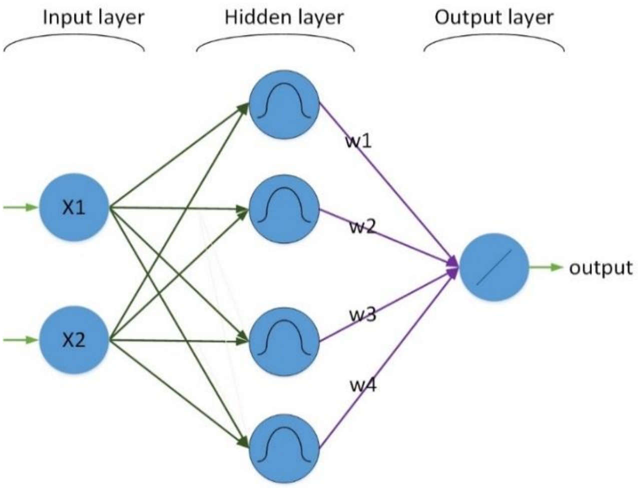

Figure 2. RBF model for a system with two inputs and one output

The RBF model (Figure 2) consists of two input neurons, four Gaussian hidden neurons and a linear neuron as an output neuron which is used for modeling a system with two inputs and one output. The multivariable Gaussian function is used as the activation function for neurons in hidden layer as shown in Equation 1. In Equation (1) the yj is the output of the jth hidden neuron, $\vec{x}$ is the input vector which is defined as $\vec{x}=[x_1,x_2]$ $\vec{\mu}_j$ is the center of jth hidden neuron which is defined by $\vec{\mu}_j=[\mu_{1j},\mu_{2j}]$ and σ_j is the variance of the Gaussian function and assumed equal for both x1 and x2 variables.

$$y_j = \exp(\frac{-\|\vec{x}-\vec{\mu}_j\|^2}{\sigma_j^{\,2}} \qquad (1)$$

After computation the activation of each hidden neuron, their output will be feed to the output neuron and its output can be defined by linear combination of the all hidden neurons output as shown in Equation (2).

$$y\_out = \sum_j w_j y_j = \sum_j w_j \exp\left(\frac{-\|\vec{x}-\vec{\mu}_j\|^2}{\sigma_j^{\,2}}\right) \qquad (2)$$

One or more Gaussian function may be activated by an input vector, because depend on their centers and variances the Gaussian may have overlap with each other, So linear combination of the activated receptive fields (Gaussian functions in RBF network) will be used for computation of models output.

Many parameters in RBF structure such as number of neurons in hidden layer, center and variance of Gaussian functions and the wj coefficients are existed which should be defined by a suitable learning algorithm. The number of neurons in the hidden layer in many applications is set to the number of training sample, and each training sample will be the center of a Gaussian function and all the variances are set to a fixed value. The wj coefficients can be defined by minimizing the error function as shown in Equation 3, which y_{ti} is the real output of the ith training sample and y_{mi} is the output of the constructed model. Minimization of this error function can be done by any suitable optimization algorithm like gradient decent [22], genetic algorithm [23] and etc.

$$Error = \sum_{i=1}^{n} \| y_{ti} - y_{mi} \|^2 \qquad (3)$$

In this paper all the simulations have been conducted in MATLAB environment using its RBF toolbox.

2.3 Adaptive Neuro Fuzzy Inference System (ANFIS)

The main concept of using the advantages of both fuzzy inference and artificial neural network algorithm was the reason of developing the ANFIS algorithm in early 1990 by Jang [22]. The effectiveness of the proposed ANFIS algorithm has been shown in different engineering applications such as modeling, control, classification and etc. [25; 26; 27; 29]. ANFIS algorithm is shown to be a universal approximate [29]. The structure of ANFIS algorithm consists of five layers is shown in Figure 3. Responsibility of each layer will be discussed as follows with more details:

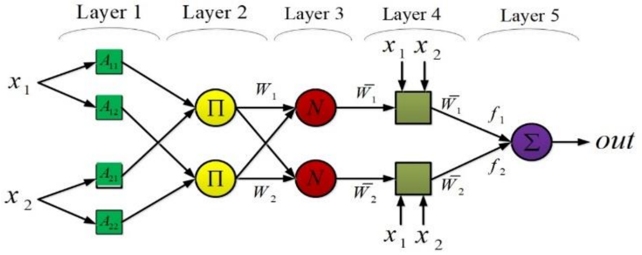

Figure 3. Structure of ANFIS algorithm

Layer1:

Each node in this layer consists of a membership function Aij. The input of each node in this layer is xi (one of system input) and output is a number between 0 and 1 that shows the degree which xi satisfies Ak. Ai is a linguistic variable like small, big and etc.

Layer2:

The output node in this layer is the product of their inputs, for example $w_1 = A_{11}(x_1) \times A_{21}(x_2)$, and actually, the output of these nodes can be the application of any T-norm operators that perform generalized AND can be used as a node function.

Layer3:

The output node in this layer is ratio of corresponding wi to the sum of all wk: k=1: n.

$$\bar{w}_1 = \frac{w_1}{w_1 + w_2}$$

Layer4:

The output nodes in this layer will be as follows:

$$o_i = \bar{w}_i \times f_i = \bar{w}_i \times (p_i x_1 + q_i x_2 + r_i)$$

where, $\bar{w}_i$ is the output of the previous layer and $\{p_i, q_i, r_i\}$ are the parameter set which should be computed in learning mechanism.

Layer5:

The single node in this layer, computes the overall output of the system as follow:

$$out = f(x_1, x_2) = \sum_i \bar{w}_i \times f_i$$

Computation of the parameters can be done by various learning algorithms such as gradient descent, evolutionary algorithms and etc. For learning phase, a suitable error measure should be selected; thus the learning algorithm should select the parameters for minimizing the error.

In this paper, the genfis3 function of MATLAB is used for implementation of the ANFIS algorithm.

2.4 Statistical criteria

Since the variation of input parameters is not homogeneous, therefore, according to Equation 4, the data were normalized

$$x_{normal} = \frac{x - \bar{x}}{\sigma} \qquad (4)$$

where x , $\bar{x}$ and σ are the measurement , mean and variance values of observed data respectively . Normalized data is applied to different algorithms. The output wave height of the model by the inverse process of the Equation (4) is returned to its original state.

In this study, three statistical criteria, namely, The correlation coefficient, R, the mean square error RMSE and fraction of variance unexplained (FVU) were used for evaluating of different models and algorithms.

Correlation coefficient, R, was used as:

$$R = \frac{\sum_i ((x_i - \bar{x}) \times (y_i - \bar{y}))}{\sqrt{\sum_i (x_i - \bar{x})^2 \sum_i (y_i - \bar{y})^2}} \qquad (5)$$

In order to evaluate the spread of the predicted values, RMSE, can be defined as:

$$MSE = \sqrt{\frac{\sum_i (x_i - y_i)^2}{n}} \qquad (6)$$

In order to evaluate the fraction of variance unexplained, FVU can be defined as:

$$FVU = \frac{VAR_{err}}{VAR_{tot}} = \frac{ss_{err}/n}{ss_{tot}/n} = \frac{ss_{err}}{ss_{tot}}$$

$$ss_{err} = \sum_{i=1}^{N} (\mathrm{x}_i - y_i)^2 \qquad (7)$$

$$ss_{tot} = \sum_{i=1}^{N} (\mathrm{x}_i - \bar{x})^2$$

where, xi and yi represent the observed and predicted values at ith time step, respectively, $\bar{x}$ is the mean of observed values, and N is the number of observations.

2.5 Observed data

Wave data collected by a buoy deployed at 15 meter depth at 49°53'0"E and 37°25'0"N off the Anzali coast (south of the Caspian Sea). Data collection was done by I.R. Iran Meteorological Organization (IRIMO). The data cover the period from 03.01.2017 to 06.01.2017 with 30-minute intervals. The statistic of recorded data is provided in Table 1.

Figure 5 shows the wind rose diagram of observed data. As can be seen, winds are predominantly from east.

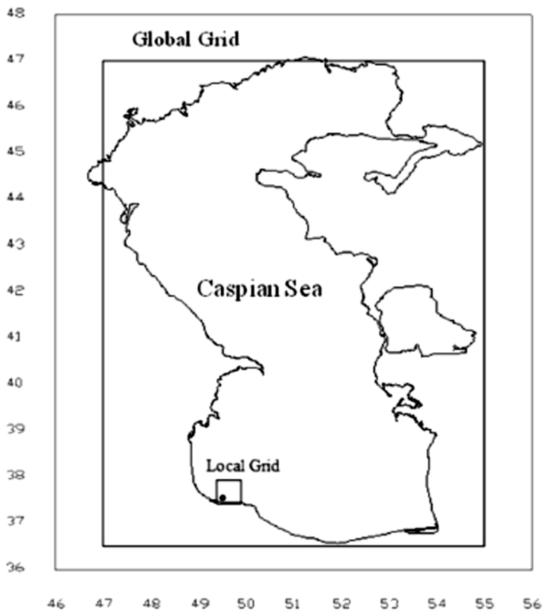

Figure 4. Map of the Caspian Sea and location of the buoy.

Table 1. Statistics of recorded data

Parameter	Minimum	Maximum	Average
Atmospheric pressure (hPa)	999.28	1035.95	1016.5
Wave height (m)	0.06	1.71	0.3556
Wave period (s)	1.4	4.5	2.409
Wind direction (deg)	0	359.69	145.69
Wind speed (m/s)	0	9.71	2.28
Current direction (deg)	0	359.69	169.31
Current surface(cm/s)	0.29	72.74	16.06

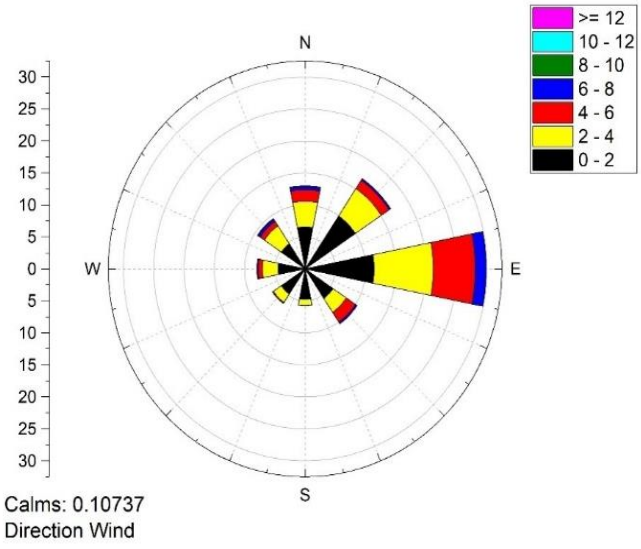

Figure 5. Wind rose diagram for study period of Anzali

The time series in Figure 6 shows the wave height, atmospheric pressure, and wind speed during the study period.

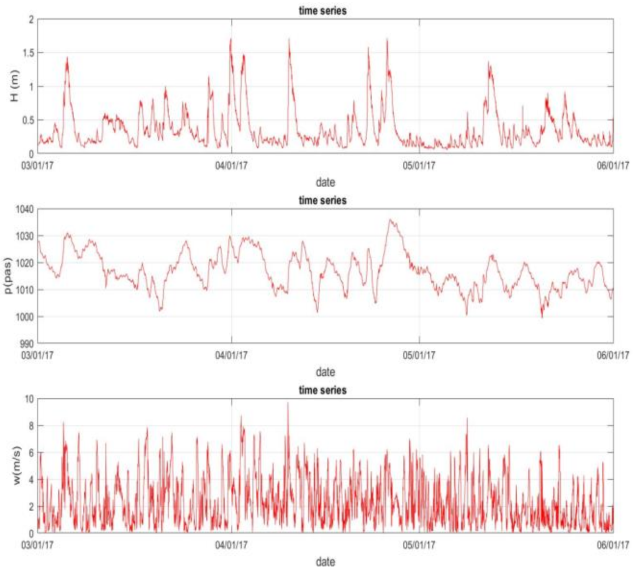

Figure 6. Half-hourly variations of the used training and testing data sets: (a) wave height (b) atmospheric pressure (c) wind speed during (01.03.2017 to 01.06.2017) in Anzali.

2.6 The models

Accurate prediction of wave height needs identification of influence factors on wave generation. One of the important factors in forecasting wave parameters is wind speed. Earlier studies showed that using shear velocity, U*, instead of wind speed at 10m height increases the accuracy of the model in the extreme events [30; 31; 32].

According to Deo et al [33] sensitivity study showed that consideration of fetch and duration neither helps in achieving training nor in improving accuracy of the output.

In this study, in addition to accepting the suggestions of the previous studies, the atmospheric pressure parameter was applied to predict the wave in some models. For the analysis and predication, friction velocity, atmospheric pressure, wave height and wave period at current time and previous time were entered into the models and algorithms to predict significant wave height in different lead times (3h, 6h, 12h, 24h and 48h).

In this paper, the following models were used to predict wave height.

Model A:

$$H_{t+i} = f(H_t, H_{t-1}, H_{t-2}, P_t, P_{t-1}, P_{t-2}, \ldots, P_{t-7})$$

Model B:

$$H_{t+i} = f(H_t, H_{t-1}, H_{t-2}, U_t^*, U_{t-1}^*, U_{t-2}^*, \ldots, U_{t-7}^*)$$

Model C:

$$H_{t+i} = f(H_t, H_{t-1}, H_{t-2}, U_t^* \cos(\varphi_t - \theta_t), U_{t-1}^* \cos(\varphi_{t-1} - \theta_t), U_{t-2}^* \cos(\varphi_{t-2} - \theta_t))$$

ModelD:

$$H_{t+i} = f(H_t, H_{t-1}, H_{t-2}, P_t, P_{t-1}, P_{t-2})$$

where, “i” indicates the forecasting lead time of 3, 6, 12, 24, and 48h.

In these models, the variables include significant wave height (H_t), sea surface wind speed (U), wave direction (θ_t), wind direction (φ_t), pressure air (P).

In order to select the best number of neurons in hidden layer, the models were run with different number of neurons. Then, based on the root mean squared error (RMSE) and coefficient of determination (R), the best number of neuron was determined for each model. Figure 7 shows a typical process of determining the neurons number.

The results of selecting the best number of neurons in the hidden layer for all of prediction lead-time are shown in Table 2.

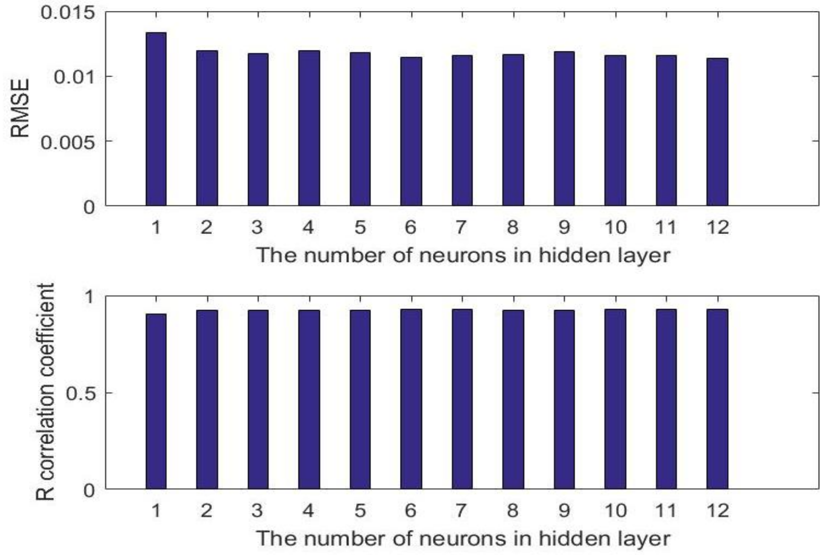

Figure 7. Assessment of the number of neurons in the hidden layer

Table 2. The best number of hidden layer neurons of each model to forecast lead-time in MLP algorithm.

	lead time(h)	**3**	**6**	**12**	**24**	**48**
model A	The correlation coefficient (R)	0.9273	0.83	0.66	0.39	0.33
	MLP_std_reg	0.01138	0.0241	0.045	0.069	0.072
	Number of neurons in the hidden layer	10	5	11	12	11
Model B	The correlation coefficient (R)	0.9211	0.8089	0.55	0.219	0.12
	MLP_std_reg	0.012	0.02841	0.056	0.077	0.081
	Number of neurons in the hidden layer	4	5	3	7	5
Model C	The correlation coefficient (R)	0.92	0.8	0.547	0.22	0.069
	MLP_std_reg	0.0122	0.029	0.5695	0.077	0.081
	Number of neurons in the hidden layer	2	2	10	6	10
Model D	The correlation coefficient (R)	0.928	0.833	0.65	0.3968	0.37
	MLP_std_reg	0.011	0.0249	0.0469	0.068	0.071
	Number of neurons in the hidden layer	11	12	12	7	12

3. Results and Discussion

The present study aims at the application of MLP, RBF, and ANFIS to carry out the real- time forecasting of significant wave heights over time steps of a few or two days at a specified location and season. Tables 3 to ۶ show the error statistics in the testing stages of three algorithms for the models A, B, C, and D. As shown, when the model B (the model without atmospheric pressure inputs) is compared with the models A and D (the model without friction velocity inputs). The results of models B and C have less accuracy than those of models A and D in large lead-time. This means that the need for atmospheric pressure parameters as inputs is very important in long-time forecasting.

The bold numbers in tables 3 to 6 show output better than other algorithms.

Table 3. Error indices for all three algorithms in model A for 3- 48 hourly forecasting times

	lead times(h)	Algorithm	FVU_error	std_FVU	RMSE_error	std_mse	R_coef	std_reg
Model A	3	MLP	0.228	0.027	0.096	0.004	0.914	0.009
	3	RBF	0.222	0.014	0.094	0.003	0.919	0.005
	3	ANFIS	**0.163**	0.000	**0.007**	0.000	**0.931**	0.000
	6	MLP	0.614	0.078	0.133	0.005	0.825	0.016
	6	RBF	0.729	0.060	0.141	0.005	0.803	0.016
	6	ANFIS	**0.455**	0.000	**0.016**	0.000	**0.845**	0.000
	12	MLP	2.042	0.429	0.195	0.017	0.553	0.107
	12	RBF	2.939	0.242	0.187	0.008	0.617	0.056
	12	ANFIS	**1.575**	0.000	**0.029**	0.000	**0.697**	0.000
	24	MLP	**7.344**	1.668	0.261	0.003	0.106	0.044
	24	RBF	15.194	0.991	0.224	0.006	0.453	0.114
	24	ANFIS	11.572	0.000	**0.047**	0.000	**0.555**	0.000
	48	MLP	**5.251**	1.644	0.262	0.013	0.106	0.071
	48	RBF	6.558	0.927	0.252	0.005	0.149	0.010
	48	ANFIS	20.796	0.000	**0.055**	0.000	**0.308**	0.000

Table 4. Error indices for all three algorithms in model B for 3 to 48 hourly forecasting times 3 to 48 hourly forecasting times

	lead times	Algorithm	FVU_error	std_FVU	RMSE_error	std_mse	R_coef	std_reg
Model B	3	MLP	0.189	0.028	0.088	0.005	0.927	0.008
	3	RBF	0.204	0.003	0.091	0.000	0.922	0.001
	3	ANFIS	**0.164**	0.000	**0.007**	0.000	0.930	0.000
	6	MLP	0.560	0.081	0.131	0.004	0.833	0.011
	6	RBF	0.671	0.014	0.139	0.001	0.808	0.002
	6	ANFIS	**0.498**	0.000	**0.017**	0.000	0.834	0.000
	12	MLP	3.025	0.781	0.186	0.007	0.622	0.033
	12	RBF	3.252	0.018	0.190	0.000	0.596	0.000
	12	ANFIS	**2.272**	0.000	**0.032**	0.000	0.656	0.000
	24	MLP	**24.234**	12.545	0.232	0.005	0.200	0.072
	24	RBF	27.049	3.888	0.227	0.004	0.278	0.079
	24	ANFIS	39.890	0.000	**0.050**	0.000	0.405	0.000
	48	MLP	**19.123**	5.399	0.251	0.004	-0.117	0.030
	48	RBF	15.844	0.316	0.253	0.001	-0.111	0.015
	48	ANFIS	34.660	0.000	**0.059**	0.000	**-0.052**	0.000

Table 5. Error indices for all three algorithms in model C for 3 to 48 hourly forecasting times

	lead times	Algorithm	FVU_error	std_FVU	RMSE_error	std_mse	R_coef	std_reg
Model C	3	MLP	**0.162**	0.005	0.087	0.001	0.927	0.001
	3	RBF	0.170	0.002	0.087	0.000	0.927	0.000
	3	ANFIS	0.167	0.000	**0.008**	0.000	**0.928**	0.000
	6	MLP	**0.479**	0.041	0.130	0.001	0.831	0.003
	6	RBF	0.507	0.002	0.132	0.001	0.825	0.002
	6	ANFIS	0.499	0.000	**0.017**	0.000	**0.834**	0.000
	12	MLP	2.635	0.185	0.185	0.001	0.623	0.009
	12	RBF	2.449	0.113	0.182	0.001	0.643	0.002
	12	ANFIS	**2.258**	0.000	**0.032**	0.000	**0.660**	0.000
	24	MLP	19.982	8.050	0.222	0.003	0.359	0.036
	24	RBF	**17.107**	0.700	0.222	0.002	0.366	0.036
	24	ANFIS	42.402	0.000	**0.050**	0.000	**0.405**	0.000
	48	MLP	83.165	75.203	0.241	0.003	-0.069	0.037
	48	RBF	**29.049**	3.053	0.244	0.001	**-0.066**	0.004
	48	ANFIS	86.229	0.000	**0.057**	0.000	-0.074	0.000

Table 6. Error indices for all three algorithms in model D for 3- 48 hourly forecasting times

	lead times	Algorithm	FVU_error	std_FVU	RMSE_error	std_mse	R_coef	std_reg
Model D	3	MLP	0.221	0.041	0.096	0.008	0.913	0.016
	3	RBF	0.197	0.011	0.089	0.002	0.927	0.003
	3	ANFIS	**0.164**	0.000	**0.007**	0.000	**0.931**	0.000
	6	MLP	0.800	0.150	0.152	0.013	0.761	0.051
	6	RBF	0.725	0.086	0.140	0.007	0.807	0.022
	6	ANFIS	**0.483**	0.000	**0.016**	0.000	**0.839**	0.000
	12	MLP	2.879	1.191	0.196	0.015	0.539	0.107
	12	RBF	3.145	0.198	0.187	0.009	0.625	0.076
	12	ANFIS	**1.712**	0.000	**0.030**	0.000	**0.680**	0.000
	24	MLP	**8.403**	6.649	0.251	0.008	0.162	0.062
	24	RBF	14.249	0.799	0.230	0.002	0.388	0.070
	24	ANFIS	10.555	0.000	**0.048**	0.000	**0.530**	0.000
	48	MLP	**2.944**	0.953	0.313	0.043	0.035	0.078
	48	RBF	5.464	0.874	0.255	0.004	0.147	0.002
	48	ANFIS	18.118	0.000	**0.055**	0.000	**0.309**	0.000

Figure 8 shows scatter plots for all the considered models. This plot displays the direct Comparison between the observed and forecasted H computed by three algorithms for model A in different lead-times: (a) 3h, (b) 6h. (c)12h, and (d) 24h. For short lead times (3h and 6 h), the data are dense around the first quadrant bisector, but for large lead times (24h), the performance of all methods were reasonable in the small wave height. So For the lead time of 24 h, the prediction accuracy further dropped down. The correlation coefficient of all three methods for 3 h lead time is in the same range (0.927–0.93); however, by increasing the lead time, the correlation coefficient of all methods decreases

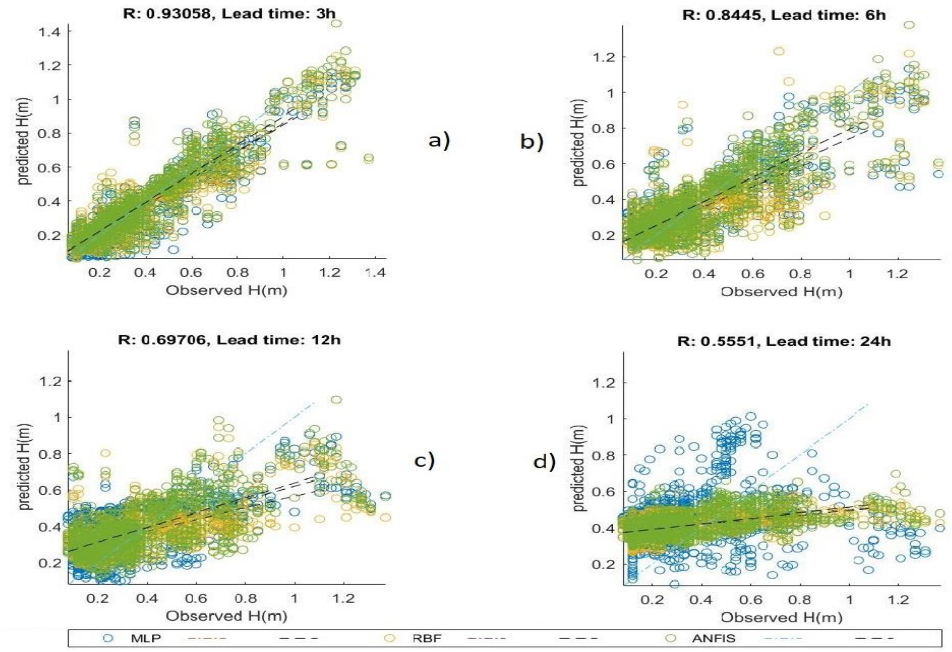

Figure 8. Comparison between the observed and forecasted H computed by three algorithm for model A and different lead-time: (a) 3h, (b) 6h, (c) 12h, and (d) 24h

Figure 9 shows the observed and predicted wave height computed by different algorithms during the analysis 05.12.2017 to 06.01.0217 for model A in 3, 6, 12, 24, and 48h lead times. Fig. 9a shows the forecast for short lead time (3 h) where all three algorithms were well trained and able to forecast almost whole time period including one hurricane. For 6 h lead time (Fig. 9b) , 12h (Fig. 9c), 24 h (Fig. 9d) and 48 h (Fig. 9e), ANFIS algorithm was well trained to forecast of significant height.

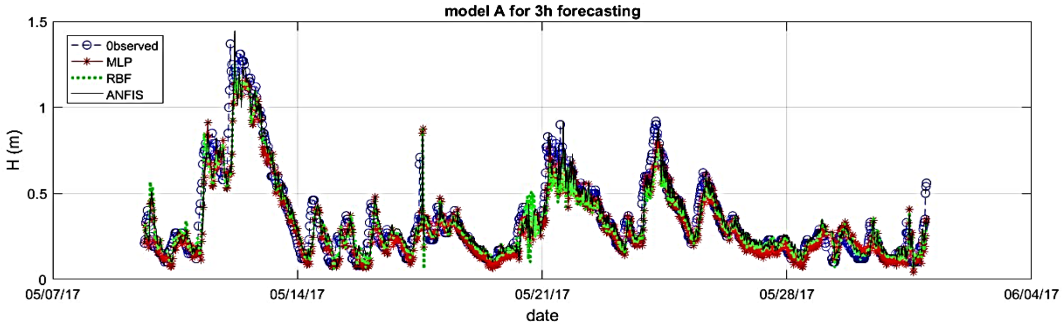

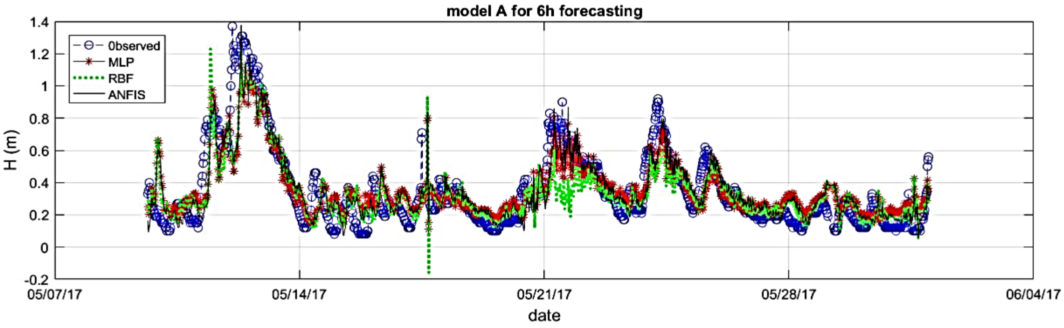

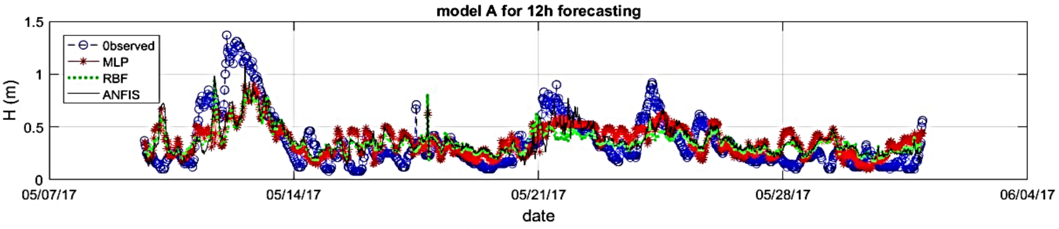

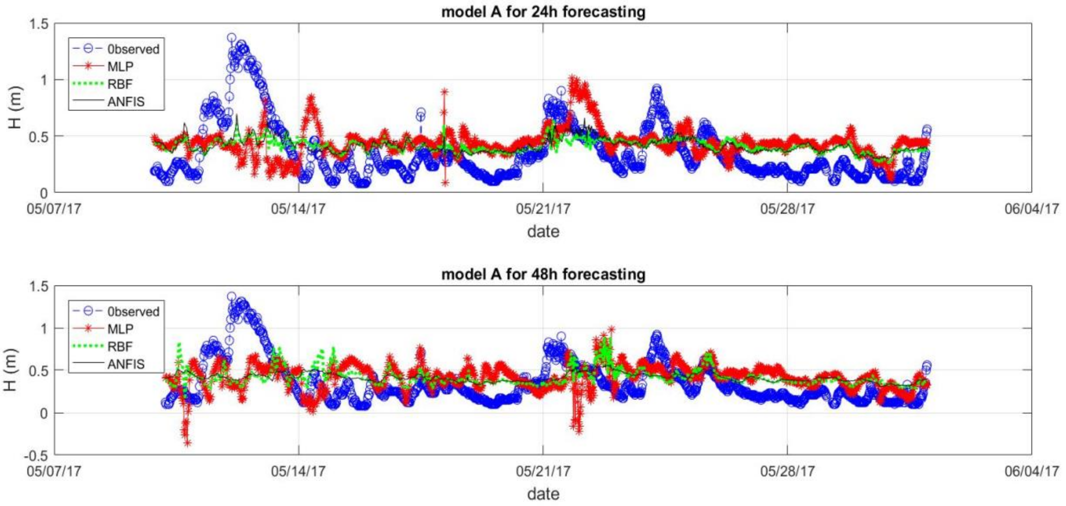

Figure 9. Predicted and observed wave height during test period using three methods and different lead-times: (a) 3h, (b) 6h, (c) 12h, (d) 24h (e) 48h

4. Conclusion

This research mainly focused on predicting significant wave height over the Caspian Sea (Anzali) for winter season by different soft computing methods; Multi-layer perceptron (MLP), radial basis function neural network (RBFNN) and Adaptive Neuro Fuzzy Inference System (ANFIS). In order to investigate the effectiveness of each parameter, all four-mentioned model were applied to three soft computing techniques (MLP, RBF and ANFIS) with normalized input and output. The results showed that using atmospheric pressure instead of friction velocity and significant wave height at current time, Hh,s , Hh,s-1, and Hh,s-2 increases the accuracy of the model in short and long lead times based on ANFIS algorithm. Meanwhile, in any combination that contains the atmospheric pressure parameter, the results indicated a higher accuracy. Also, in long lead times, the predicted wave height does not correlate to the pervious and current friction velocity. In summary, Figure 10 shows the comparison of error indices of the models for different lead-times by ANFIS algorithm. As the figure indicates, the model A has better results than other models.

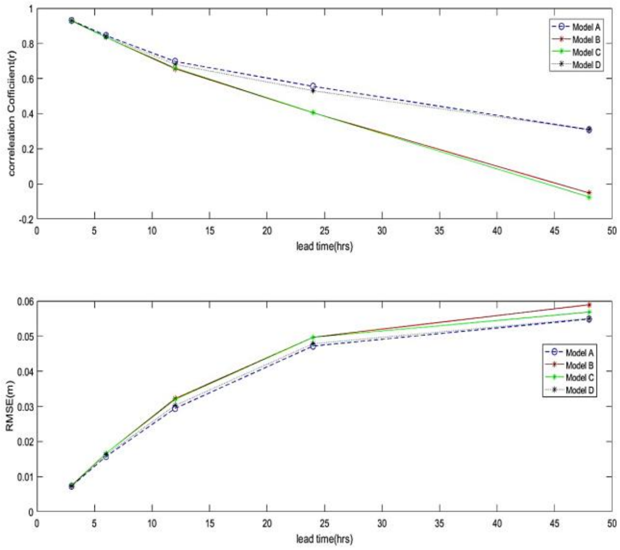

Figure 10. Comparison of error indices in different methods for different lead-times; (a) Variations of correlation coefficient (R) (b) RMSE, vs. forecasting lead-time

References

1- Bretschneider, C. L., (1951). *Revised wave forecasting relationships*. Coastal Engineering Proceedings, 1(2), 1.

2-Sverdrup, H. U., & Munk, W. H.,(1947), *Wind, sea, and swell: theory of relations for forecasting*.

3-Army, U. S., (2003), *Coastal engineering manual, chapter II-2, meteorology and wave climate*. US Army Engineer Waterways Experiment Station, US Government Printing Office, No. EM, 1110–1112.

4- Donelan, M. A., (1980). *Similarity theory applied to the forecasting of wave heights, periods and directions*. National Water Research Institute.

5- Booij, N., Ris, R. C., and Holthuijsen, L. H., (1999), *A third- generation wave model for coastal regions: 1. Model description and validation*. Journal of Geophysical Research: Oceans, 104(C4), 7649–7666.

6- Komen, G. J., Cavaleri, L., and Donelan, M., (1996), *Dynamics and modelling of ocean waves.* Cambridge university press.

7- Goda, Y., (2003), *Revisiting Wilson's formulas for simplified wind-wave prediction.* Journal of Waterway, Port, Coastal, and Ocean Engineering, 129(2), 93–95.

8-Mahjoobi, J., Etemad-Shahidi, A., and Kazeminezhad, M. H., (2008), *Hindcasting of wave parameters using different soft computing methods*. Applied Ocean Research, 30(1), 28–36.

9- Makarynskyy, O., (2004), *Improving wave predictions with artificial neural networks*. Ocean Engineering, 31(5–6), 709–724.

10-Tsai, C.-P., & Lee, T.-L., (1999), *Back-propagation neural network in tidal-level forecasting*. Journal of Waterway, Port, Coastal, and Ocean Engineering, 125(4), 195–202.

11- Vimala, J., Latha, G., and Venkatesan, R.,(2014). *Real time wave forecasting using artificial neural network with varying input parameter*.

12-Dezvareh, R., (2019). *Application of Soft Computing in the Design and Optimization of Tuned Liquid Column–Gas Damper for Use in Offshore Wind Turbines.* International Journal of Coastal and Offshore Engineering, 2(4), pp.47-57.

13-Dezvareh, R., (2019). *Providing a new approach for estimation of wave set-up in Iran coasts.* Research in marine sciences, 4(1), 438-448.

14-Dezvareh, R., Bargi, K. and Moradi, Y., (2012). *Assessment of Wave Diffraction behind the Breakwater Using Mild Slope and Boussinesq Theories*. International Journal of Computer Applications in Engineering Sciences, 2(2).

15-Etemad-Shahidi, A., and Mahjoobi, J., (2009), *Comparison between M5′ model tree and neural networks for prediction of significant wave height in Lake Superior*. Ocean Engineering, 36(15–16), 1175–1181.

16- Samadi, M., Jabbari, E., and Azamathulla, H. M., (2014), *Assessment of M5′ model tree and classification and regression trees for prediction of scour depth below free overfall spillways.* Neural Computing and Applications, 24(2), 357–366.

17- Kazeminezhad, M. H., Etemad-Shahidi, A., & Mousavi, S. J, (2005), *Application of fuzzy inference system in the prediction of wave parameters.* Ocean Engineering, 32(14–15), 1709–1725.

18- Broomhead, D. S., and Lowe, D., (1988), *Radial basis functions, multi-variable functional interpolation and adaptive networks.* Royal Signals and Radar Establishment Malvern (United Kingdom).

19- Powell, M. J. D., (1985), *Radial basis function for multivariable interpolation: a review.* In IMA Conference on Algorithms for the Approximation of Functions ans Data, 1985. RMCS.

20-Belloir, F., Fache, A., and Billat, A., (1999), *A general approach to construct RBF net-based classifier*. In ESANN (pp. 399–404). Citeseer.

21- Li, Y., Qiang, S., Zhuang, X., and Kaynak, O., (2004), *Robust and adaptive backstepping control for nonlinear systems using RBF neural networks.* IEEE Transactions on Neural Networks, 15(3), 693–701.

22- Karayiannis, N. B., (1999), *Reformulated radial basis neural networks trained by gradient descent.* IEEE Transactions on Neural Networks, 10(3), 657–671.

23- Chen, S., Wu, Y., and Luk, B. L., (1999), *Combined genetic algorithm optimization and regularized orthogonal least squares learning for radial basis function networks.* IEEE Transactions on Neural Networks, 10(5), 1239–1243.

24- Jang, J.-S., (1993), *ANFIS: adaptive-network-based fuzzy inference system*. IEEE Transactions on Systems, Man, and Cybernetics, 23(3), 665–685.

25- Manoj, S. B. A., (2011), Identification and control of nonlinear systems using soft computing techniques. International Journal of Modeling and Optimization, 1(1), 24.

26- Pradhan, B., (2013), *A comparative study on the predictive ability of the decision tree, support vector machine and neuro-fuzzy models in landslide susceptibility mapping using GIS*. Computers & Geosciences, 51, 350–365.

27- Tushar, A., & Pillai, G. N., (2015), *Extreme Learning ANFIS for classification problems*. In Next Generation Computing Technologies (NGCT),1st International Conference on (pp. 784–787). IEEE.

28- Kaplan, K., Kuncan, M., and Ertunc, H. M., (2015), *Prediction of bearing fault size by using model of adaptive neuro-fuzzy inference system.* In Signal Processing and Communications Applications Conference (SIU), pp. 1925–1928. IEEE.

29- Jang, J.-S. R., Sun, C.-T., and Mizutani, E. (1997), *Neuro-fuzzy and soft computing; a computational approach to learning and machine intelligence*.

30- Zamani, A., Solomatine, D., Azimian, A., and Heemink, A., (2008), *Learning from data for wind–wave forecasting.* Ocean Engineering, 35(10), 953–962.

31- Kamranzad, B., Etemad-Shahidi, A., and Kazeminezhad, M. H.(2011), *Wave height forecasting in Dayyer, the Persian Gulf.* Ocean Engineering, 38(1), 248–255.

32- Mafi, S., and Amirinia, G., (2017), Forecasting hurricane wave height in Gulf of Mexico using soft computing methods. Ocean Engineering, 146, 352–362.

33- Deo, M. C., Jha, A., Chaphekar, A. S., and Ravikant, K. (2001). *Neural networks for wave forecasting*. Ocean Engineering, 28(7), 889-898.

INTERNATIONAL JOURNAL OF
COASTAL & OFFSHORE ENGINEERING

IJCOE Vol.4/No. 1/Spring 2019 (41-46)

Available online at: http://ijcoe.org/browse.php?a_code=A-10-243-1&sid=1&slc_lang=en

Recent Wave Breaking Prediction Formulas Evaluation Based On Compiled Laboratory Data

Behrooz Tadayon[1], Hamid Dehghani[2], Cyrus Ershadi[3*]

[1] *M.Sc Student, Civil Engineering Department, Faculty of Engineering, Hormozgan University, Hormozgan, Iran; b.tadayon.stu@hormozgan.ac.ir*
[2] *M.Sc Student, Civil Engineering Department, Faculty of Engineering, Hormozgan University, Hormozgan, Iran; hamid.dehghani.stu@hormozgan.ac.ir*
[3*] *Assistant Professor, Civil Engineering Department, Faculty of Engineering, Hormozgan University, Hormozgan, Iran; cyrusershadi1@yahoo.co.uk*

ARTICLE INFO

Article History:
Received: 30 Apr. 2019
Accepted: 3 Jun. 2019

Keywords:
wave breaking
breaker type
breaker height
breaker depth
laboratory data

ABSTRACT

One of the most important issues in the area of coastal structures design is determination of forces and loadings resulted from shallow water wave breaking. In the process of wave breaking, the subsequent particle motion is transformed from irrotational to rotational motion and due to this matter, vorticity and turbulence are generated and the sediment transport is affected by this phenomenon. Therefore, it is necessary to know about the location of wave breaking and other parameters such as the breaker height, breaker depth, etc. Over the last century, several formulas have been presented for predicting the wave breaking onset. These formulas depend on many parameters (e.g. seabed slope, water depth at the location of breaking, offshore wave height, etc.) that need to be known in order to obtain the desired wave breaking parameter (e.g. breaker height). In this study, some of the formulas for predicting wave breaking onset proposed in the recent decade are evaluated using the available laboratory data and it is tried to find out which formula is more suitable in different cases and conditions. A refinement process is carried out for choosing the appropriate data points out of all the available compiled laboratory data. The comparison is carried out in two phases. In the first one, the formulas are compared using all the data and in the second one, the comparisons are made based on the breaker type. These two phases yield to different outcomes. In the first phase, the formula proposed by Delavari et al. has the lowest values of bias, relative error, scatter index and root mean square error and the coefficient of determination of Goda's formula is the highest. In the second phase, the data are categorized based on the plunging and spilling breaker types and the comparisons are made based on this categorization. The outcomes derived from the first phase are different from the ones derived from the second one.

1. Introduction

Generally, as a wave propagates from deep water into shallow parts, its characteristics are changed and the wave steepness is increased due to shoaling. This increase is continued until the wave breaks at certain depth. Wave breaking also occurs in deep water, but the main focus here is on the wave breaking due to shoaling as a coastal process. When breaking is initiated, it develops quickly until the process is finished. In this process, a considerable amount of wave energy is released. For almost a century, many researchers have focused on the initiation of wave breaking because it's an important aspect in the design of coastal structures. The magnitude of wave forces and structures loadings depend on the wave height; thus it is necessary to predict the wave height in the instant of breaking (i.e. the breaker height). A considerable amount of formulas has been proposed by different researchers for predicting the wave height and water depth when wave breaking takes place [1]. Most of these formulas have two factors in common; the wave steepness and seabed slope. These two factors are almost the main factors for predicting the wave breaking initiation.

The aforementioned formulas can be classified into six different groups [1]. This classification is based on different factors that influence the four common indices for describing the breaker height. These indices are in the dimensionless form of H_b/d_b, H_b/H_o, H_b/L_b, and H_b/L_o. The subscripts *b* and *o* indicate the breaking and offshore conditions, respectively, and *H*, *d* and *L* are the wave height, water depth and wavelength, respectively. The first and second indices are known as the breaker depth index (γ_b) and the breaker height index (Ω_b), respectively. In this six-group categorization, the effective factors on the indices are the surf similarity parameter, breaking wavelength, offshore wavelength and height, and seabed slope. It should be mentioned that the surf similarity parameter ξ_o (also known as the Irribaren number) is used for categorizing the breaker type:

$$\xi_o = \frac{\tan\beta}{\sqrt{H_o/L_o}} \tag{1}$$

where β denotes the seafloor angle, H_o is the offshore wave height and L_o indicates the offshore wavelength. According to this parameter, the breaking type is classified into 3 groups [2] (i.e. surging/collapsing, plunging, and spilling).

The initial attempts to propose a new wave breaking predicting formula were based on simple laboratory tests with limited applications. For instance, McCowan studied wave breaking for the case of a solitary wave over a horizontal seafloor in 1894 [3] and proposed the formula $H_b = 0.78d_b$ for predicting breaker height. Thereafter, several other researches have been carried out with more complicated beach types and waves (including irregular and random waves) [1]. In 2010, Delavari et al. [4] proposed a formula using a statistical model based on the available laboratory data. The relation is given in the following:

$$H_b = L_0 \times \left[0.001m^{-0.358} + 0.608m^{-0.069} \left(\frac{H_0}{L_0} \right)^{0.768m^{-0.053}} \right] \tag{2}$$

in which, *m* is the seabed slope. As seen in Eq. (2), the breaker height can be calculated using the seabed slope and offshore wave height and wavelength. As stated by Delavari et al., the proposed relation is more accurate than other relations mentioned in Ref. [4] for predicting the breaker height.

Another formula investigated here is the formula proposed by Goda in 2010 [5]. The relation is as follows:

$$H_b = 0.17L_0 \left[1 - \exp\left(-1.5 \frac{\pi d_b}{L_o} \left(1 + 11m^{\frac{4}{3}} \right) \right) \right] \tag{3}$$

Eq. (3) is a modification of Goda's initial wave breaking prediction formula (see Ref. [2] for more details). This modification has led to better agreement with the available laboratory data mentioned in Ref. [2].

In 2015, Robertson et al. [6] proposed a new wave breaking prediction formula using the artificial neural networks (ANNs). The new formula was evaluated by both laboratory and field data so that full-scale studies were done and the limitations of laboratory-based analyses (e.g. scaling issues, inability in scaling all characteristics of breaking, and etc.) were eliminated. The formula is given below:

$$H_b = 0.17L_0 \left[1 - \exp\left(\frac{\pi d_b}{L_o} (1.978m - 1.792) \right) \right] \tag{4}$$

The other formula investigated here is proposed by Antoniadis in 2018 [2]. This formula considers the effect of oblique waves on wave breaking. The relation is as follows:

$$\begin{aligned} H_b &= 0.1657\cos\theta_0 - 0.1885m + \\ &1.0284H_0 + 0.00189L_0 - 0.1504 \end{aligned} \tag{5}$$

in which, θ_0 denotes the deep water wave angle. The accuracy of this formula in predicting the breaker height was shown to be better than other published formulas.

In this research, the wave breaking predicting formulas introduced in the previous paragraphs are compared and evaluated based on the available compiled laboratory data and it is tried to find the most accurate one. Note that some of the data points are ignored due to a refinement process described in the following section. The parameters such as seabed slope and offshore wavelength are common in all of the formulas investigated here. Two phases are considered in the comparison process. The first one contains all of the refined data points for comparing the formulas and in the second phase, the comparisons are based on the breaker type. As it is shown in the next parts, these phases lead to different outcomes.

2. Materials and methods

Twenty-five experimental datasets with overall 536 data points were gathered (as shown in Table 1). After carrying out a refinement process, about 370 data points were selected. They are used for comparing the aforementioned empirical relations with the available laboratory data.

The refinement process is based on two breaker type criteria described by Battjes [7] and Camenen and

Larson [8]. According to Battjes [7], the breaker type is described by the Irribaren number as below:

Table 1: The available compiled laboratory data

Dataset	$H_b\,(\mathrm{m})$	m	$T\,(\mathrm{s})$
Munk (1949)	0.068-0.099	0.009-0.072	0.86-1.98
Iversen (1952)	0.047-0.125	0.02-0.1	0.74-2.67
Morison and Crooke (1953)	0.055-0.113	0.02-0.1	0.78-2.62
Horikawa and Kuo (1967)	0.060-0.182	0.0125-0.05	1.2-2.3
Komar and Simmons (1968)	0.034-0.170	0.036-0.105	0.81-2.37
Galvin (1969)	0.038-0.177	0.05-0.2	1.0-6.0
Weggel (1970)	0.089-0.161	0.051	1.26-2.05
Saeki and Sasaki (1973)	0.099-0.106	0.02	1.3-2.5
Iwagaki et al. (1974)	0.044-0.128	0.03-0.1	1.0-2.0
Walker (1974)	0.024-0.115	0.033	1.17-2.33
Van Dorn (1978)	0.108-0.166	0.022-0.083	1.65-4.80
Hansen and Svendsen (1979)	0.071-0.102	0.0292	1.0-3.33
Singamsetti and Wind (1980)	0.073-0.193	0.025-0.2	1.03-1.73
Mizuguchi(1981)	0.1	0.1	1.2
Visser (1982)[1]	0.058-0.108	0.05-0.101	0.7-2.01
Stive (1986)	0.178	0.025	1.79
Smith and Kraus (1990)	0.082-0.164	0.033	1.02-2.49
Ting and Kirby (1994)	0.163-0.191	0.0286	2.0-5.0
Zou et al. (1999)	0.044-0.120	0.01-0.025	1.0-2.0
Hoque (2002)	0.117-0.207	0.1053	1.12-1.8
Deo and Jagdale (2003)	0.094-0.141	0.033-0.100	0.74-1.20
Cox and Shin (2003, 2006)	0.144-0.157	0.0286	1.5-3.0
Tsai et al. (2005)	0.135-0.305	0.1-0.333	1.8-2.6
Mori and Kakuno (2008)	0.120-0.165	0.033	1.6-3.8

$$\begin{cases} \text{spilling} & \text{if } \xi_0 \le 0.5 \\ \text{plunging} & \text{if } 0.5<\xi_0 \le 3.3 \\ \text{surging/collapsing} & \text{if } \xi_0 > 3.3 \end{cases} \tag{6}$$

In 2007, Camenen and Larson [8] proposed the following relationships between the Irribaren number and breaker depth for describing the breaker type:

$$\begin{cases} \text{spilling/plunging} \\ \qquad \text{when } \xi_0 = 1.5 - 1.25\gamma_b \quad \left(\xi_0 = 0.2 - 0.6\right) \\ \text{plunging/collapsing} \\ \qquad \text{when } \xi_0 = 4.4 - 2.5\gamma_b \quad \left(\xi_0 = 0.8 - 2.9\right) \\ \text{collapsing/surging} \\ \qquad \text{when } \xi_0 = 1.7 + 3.3\gamma_b \quad \left(\xi_0 = 3.6 - 6\right) \end{cases} \tag{7}$$

If these two criteria yield to the same breaker type, then the data point will be used. Otherwise, the data is ignored.

As it is seen in Table 1, the ranges of observed breaker height, seabed slope and period are between 0.015-0.305m, 0.009-0.105 and 0.7-8.0 sec, respectively. It should be mentioned that in the experiment of Visser [9], different wave angles are used, i.e. oblique waves are considered.

In order to compare the observed breaker height (H_{bo}) and the calculated one (H_{bc}), the following statistical characteristics are used:

- Root mean square error (*RMSE*): A non-negative parameter used as a measure of accuracy. The model which has lower *RMSE* is more accurate.

$$RMSE = \sqrt{\frac{\sum_{i=1}^{N}\left(H_{bc,i} - H_{bo,i}\right)^2}{N}} \tag{8}$$

- Coefficient of determination (R^2): A measure for showing how well a model explains and predicts future outcomes. The model with a value of R^2 closer to 1 is more fit and accurate.

$$R^2 = \left[\frac{\sum_{i=1}^{N}\left(H_{bc,i} - \bar{H}_{bc}\right)\left(H_{bo,i} - \bar{H}_{bo}\right)}{\sqrt{\sum_{i=1}^{N}\left(H_{bc,i} - \bar{H}_{bc}\right)^2}\sqrt{\sum_{i=1}^{N}\left(H_{bo,i} - \bar{H}_{bo}\right)^2}}\right]^2 \tag{9}$$

- Bias (*B*): A measure for overestimating or underestimating a parameter. The model that has smaller value of *B* is more accurate.

$$B = \frac{\sum_{i=1}^{N} H_{bc,i} - H_{bo,i}}{N} \tag{10}$$

- Percentage relative error (*E*) for average wave heights:

$$E\,(\%) = \left|\frac{\bar{H}_{bc} - \bar{H}_{bo}}{\bar{H}_{bc}}\right| \times 100 \tag{11}$$

- Scatter index (*SI*):

$$SI\,(\%) = \frac{RMSE}{\frac{1}{N}\sum_{i=1}^{N} H_{ob,i}} \times 100 \tag{12}$$

3. Results and discussion

The comparison process carried out in this study consists of two phases. In the first phase, the formulas (Eqs. (2-5)) are compared using all of the 370 refined data points and its outcomes are provided in Table 2. As seen in this table, the root mean square error (*RMSE*), relative error (*E*), bias (*B*) and scatter index (*SI*) of Delavari's formula are the lowest with the values of 0.0182m, 1.90%, 0.0021m, and 16.85%, respectively and Goda's formula has the highest coefficient of determination (R^2) with the value of 0.80. Therefore, it can be concluded that the formula proposed by Delavari has better and more accurate results and Goda's formula's results are less scattered than the others.

It should be mentioned that the formula proposed by Antoniadis considers the effect of wave direction but due to the lack of the data gathered here for oblique waves, all of the experiments are assumed to have head-on waves, except for Visser's experiment that includes oblique waves. Another thing that is worthwhile to mention here is that although the formula proposed by Robertson et al. [6] has about 4.5% error in predicting the breaker height, its main applicability is for full-scale field studies with the breaker height in the range of 0.8 and 3.5 meters, but here only the available laboratory data with the maximum of 0.3 m breaker height is considered.

Figure 1 illustrates the scatter diagrams of the results of comparison between the aforementioned formulas. As it can be seen, the formula proposed by Goda is a formula with very good statistical fits.

Another aspect considered here as the second phase of the comparison process is based on the breaker type. The available compiled refined laboratory dataset contains two types of breaker type; namely plunging and spilling. Tables 3 and 4 include the comparisons between the prediction formulas (Eqs. (2-5)) for spilling and plunging types, respectively.

It can be understood from Tables 3 and 4 that for the spilling breaker type, all formulas provide acceptable results. The formula proposed by Antoniadis has the lowest bias (B) and relative error (E) with the values of 0.0002m and 0.15%, respectively. The values of root mean square error ($RMSE$) and scatter index (SI) of Goda's formula are 0.0124m and 11.13%, respectively, which are the lowest values compared to the other formulas. This formula also has the highest coefficient of determination (R^2) with the value of 0.86. When the type of breaking changes to plunging, the values of root mean square error ($RMSE$), bias (B), relative error (E), and scatter index (SI) of the formula proposed by Delavari et al. are 0.0210m, 0.0021m, 2.01% and 20.66%, respectively and the coefficient of determination (R^2) of Antoniadis's formula is 0.87. Therefore, a formula that leads to the best results in the first phase does not necessarily lead to the same results when investigating different breaker types.

4. Conclusions

The wave breaking phenomena in shallow waters is considered as a substantial criterion in coastal engineering design and it is very important to know about the location and other characteristics of wave breaking so that the resulting forces and effects on coastal areas can be understood and estimated. For about 150 years, many researchers have been trying to propose new formulas for predicting wave breaking characteristics (e.g. breaker height). In this research, about 370 experimental cases from 25 different sources were used for evaluating four wave breaking prediction formulas proposed in the recent decade. The range of the seabed slope was between 0.009 and 0.105 and the observed breaker heights were between 0.015 and 0.307m. One of the formulas was proposed by Goda in 2010. Another one was the work of Delavari et al. in 2010. The other two formulas were the ones proposed by Robertson et al. in 2015 and Antoniadis in 2018. The evaluation of the formulas was carried out using a two-step comparison process. In the first step, all of the refined data points were used for the comparison and the in the second step, the data points with similar breaker type were categorized into groups and the comparison was based on the breaker type. It has been understood from the results that the formula proposed by Delavari et al. had less error and therefore more accuracy than the other formulas in the first step of comparison. Moreover, the value of the coefficient of determination of Goda's formula was higher than the other formulas. For the second step, when the breaker type was in the form of spilling, Antoniadis's formula had the lowest values of bias and relative error and the values of root mean square error and scatter index of Goda's formula was the lowest. This formula's coefficient of determination was also the highest. For the plunging breaker type, the formula proposed by Delavari et al. was more accurate than the others since its values of root mean square error, bias, relative error and scatter index was the lowest. For the coefficient of determination, the formula proposed by Antoniadis had the highest values. Since the number of refined data points used here is limited to 370, it is suggested to evaluate these formulas using a wider range of observed breaker heights to evaluate them and find out which one is more accurate when the conditions become closer to the full-scale field condition.

Table 2: Comparison between the calculated breaker height and the observed one

Formula	Average observed wave height $\bar{H}_{bo}$ (m)	Average calculated wave height $\bar{H}_{bc}$ (m)	$RMSE$ (m)	B (m)	R^2	E (%)	SI (%)
Delavari (2010)	0.1084	0.1105	0.0182	0.0021	0.79	1.90	16.85
Goda (2010)	0.1084	0.1121	0.0188	0.0038	0.80	3.36	17.31
Robertson (2015)	0.1084	0.1037	0.0216	-0.0046	0.72	4.46	19.94
Antoniadis (2018)	0.1084	0.1026	0.0202	-0.0058	0.76	5.63	16.69

Table 3: Comparison between the calculated breaker height and the observed one for spilling breaker type

Formula	Average observed wave height $\bar{H}_{bo}$ (m)	Average calculated wave height $\bar{H}_{bc}$ (m)	*RMSE* (m)	*B* (m)	R^2	*E* (%)	*SI* (%)
Delavari (2010)	0.1114	0.1141	0.0149	0.0027	0.81	2.39	13.41
Goda (2010)	0.1114	0.1121	0.0124	0.0008	0.86	0.67	11.13
Robertson (2015)	0.1114	0.1148	0.0168	0.0034	0.78	2.95	15.06
Antoniadis (2018)	0.1114	0.1116	0.0164	0.0002	0.78	0.15	14.74

Table 4: Comparison between the calculated breaker height and the observed one for plunging breaking type

Formula	Average observed wave height $\bar{H}_{bo}$ (m)	Average calculated wave height $\bar{H}_{bc}$ (m)	*RMSE* (m)	*B* (m)	R^2	*E* (%)	*SI* (%)
Delavari (2010)	0.1017	0.1038	0.0210	0.0021	0.81	2.01	20.66
Goda (2010)	0.1017	0.1115	0.0279	0.0098	0.78	8.81	27.48
Robertson (2015)	0.1017	0.0797	0.0293	-0.0220	0.86	27.6	28.84
Antoniadis (2018)	0.1017	0.0845	0.0242	-0.0172	0.87	20.4	23.80

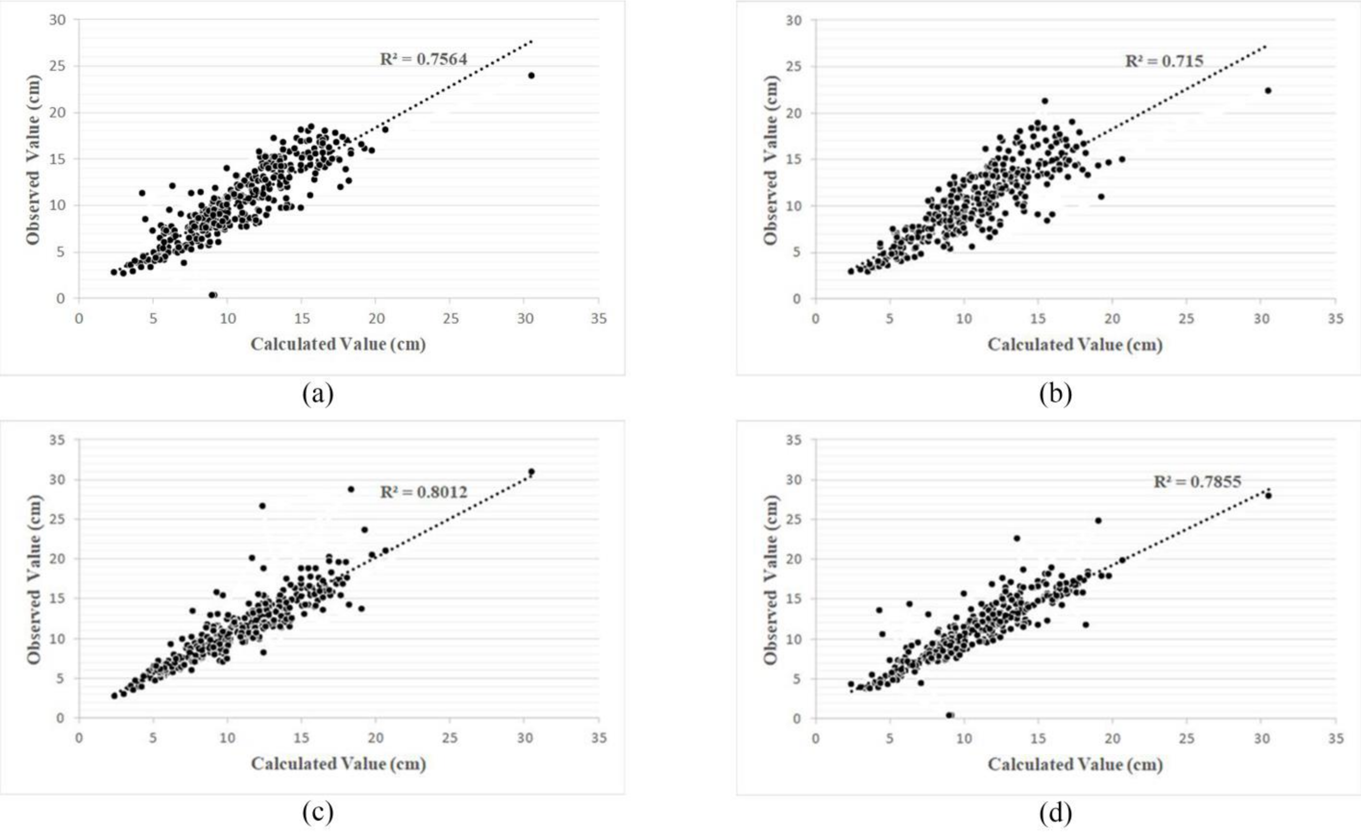

(a) (b) (c) (d)

Figure 1. The scatter diagram of (a) Antoniadis's formula (b) Robertson's formula (c) Goda's formula (d) Delavari's formula

5. Acknowledgment

The authors would like to appreciate Dr. Delavari for providing us the necessary information and data.

6. References

1-Robertson, B., Hall, K., Zytner, R., and Nistor, I., (2013), *Breaking waves: Review of characteristic relationships*, Coastal Engineering Journal, Vol.55(1).

2-Antoniadis, C., (2018), *Experimental verification of wave breaking formulae for obliquely incident waves on mixed and gravel beaches*, International Journal of Oceanography & Aquaculture, Vol.2(1).

3-McCowan, J., (1894), *On the Highest Waves of a Permanent Type*, Philosophical Magazine, Edinburgh, Vol.38, p.351–358.

4-Delavari, E., Gharebaghi, M.A., and Chenaghloo, M.R., (2011), *Prediction of water wave breaking height and depth using ANFIS*, Proceedings of the ASME 2011 30th International Conference on Ocean, Offshore and Arctic Engineering, Rotterdam, The Netherlands.

5-Goda, Y., (2010), *Reanalysis of regular and random breaking wave statistics*, Coastal Engineering Journal, Vol.52, p. 71-106.

6-Robertson, B., Gharabaghi, B., and Hall, K., (2015), *Prediction of incipient breaking wave-heights using artificial neural networks and empirical relationships*, Coastal Engineering Journal, Vol.57.

7- Battjes, J., (1974), *Surf similarity*, Proceedings of the 14th International Conference on Coastal Engineering (Copenhagen, Denmark, ASCE), p. 1050–1061.

8-Camenen, B. and Larson, M., (2007), *Predictive formulas for breaker depth index and breaker type*, Journal of Coastal Research, Vol.23(4), p.1028–1041.

9-Visser, P.J., (1982) *The proper longshore current in a wave basin*, Laboratory of fluid mechanics, Delft University of Technology, Delft, The Netherlands.

INTERNATIONAL JOURNAL OF
COASTAL & OFFSHORE ENGINEERING
IJCOE Vol.4/No. 1/Spring 2019 (47-54)

Available online at: http://ijcoe.org/browse.php?a_code=A-10-272-1&sid=1&slc_lang=en

Pitch Motion Response of an Equipped Semi-Submersible Platform with Tuned Sloshing Dampers

Arefeh Emami[1], **Ahmad Reza Mostafa Gharabaghi**[2*]

[1] *PhD candidate, Faculty of Civil Engineering, Sahand University of Technology, Tabriz, Iran; a_emami@sut.ac.ir*
[2*] *Corresponding author, Prof, Faculty of Civil Engineering, Sahand University of Technology, Tabriz, Iran; mgharabaghi@sut.ac.ir*

ARTICLE INFO

Article History:
Received: 15 Jan. 2019
Accepted: 15 Jun. 2019

Keywords:
Tuned Sloshing Dampers
Semi-Submersible
Pitch Motion
Internal Fluid Sloshing
SESAM software

ABSTRACT

Tuned sloshing dampers (TSDs) are applied to dissipate and absorb vibrational energy in structures. They can become an appropriate candidate for damping vibration in rotating offshore structures. In this study, the TSD systems are utilized in a semi-submersible platform in order to suppress its pitch motion response. First, the hydrodynamic behaviors of two different types of vessels are evaluated including a typical GVA4000 semi-submersible rig, and a floating oil storage tank using a finite element analysis. The results are compared with the available data from previous research, which the agreement is good. Subsequently, the semi-submersible platform equipped with four TSDs, which are located inside the bilge of pontoons and filled with 20% water is analyzed. It is analyzed in the frequency domain by considering the effect of internal fluid sloshing of TSDs. The results show that TSDs play a significant role for reducing the pitch motion response of the semi-submersible platform.

1. Introduction

Offshore structures are designed and constructed for different purposes which can be applied for oil exploration, production, processing, storage and transportation. Due to the reduced oil resources in shallow water fields, the offshore platforms are developed and moved into the deeper offshore area. One such platform is a semi-submersible which is commonly used for oil exploration in deep waters. The major components of a semi-submersible platform are the hull, mooring system and risers. The hull consists of the pontoons, columns, braces, deck, and topside. The mooring lines anchor this platform to the seafloor with a driven or suction pile. The risers are vertical tubes which are used for pumping seawater into decks, for exchange of heat, and to carry partially processed oil or gas to another place. The semi-submersible platform has six degrees of freedom including surge, sway, heave, pitch, roll, and yaw. The heave, pitch and roll are the most important motions of the semi-submersible platform. These motions can affect the efficiency of platform, threaten its safety and reduce oil production. Therefore, it is necessary to reduce them. One way is application of tuned oscillator systems, which can be commonly classified into passive, active, semi-active, and hybrid systems. Passive systems don't require an external power source. Active systems require a large artificial power source to send energy to the platform. Semi-active systems generally require a small power source. Hybrid systems are constructed from combination of the passive and high performance active systems [1].

Tuned liquid damper (TLD) is a type of passive energy dissipation system which falls into three categories: tuned sloshing dampers (TSDs), tuned liquid column dampers (TLCDs), and controllable TLDs [2].

In general, if the frequency of TLD system is close to one of the natural frequencies of its internal fluid, the large sloshing can be expected. When both frequencies are close to each other, the resonance will be occurred. Adjusting sloshing frequency of TLD to the natural frequency of structure cause a large amount of sloshing and wave breaking at the resonant frequencies of the structure equipped with TLD which, dissipates significant amount of energy [2].

The vibration control of offshore platforms under environmental loading using TLDs is one of the attractive subjects for a number of researchers. Spillane et al. [3] experimentally studied the effect of vertical caisson pairs mounted on the tension leg platform (TLP) columns. Karimi et al. [4] and Luo et al. [5] numerically investigated the efficiency of TLCD with a controllable valve in the motions of spar platform. The results showed that this can strongly reduce its displacements. Utilizing a TLCD in TLP was studied by Lee and Juang [6], analytically and experimentally. The results revealed that TLCD can suppress its dynamic response. A comparative study between TLCD and tuned liquid columns ball damper (TLCBD) in the vibration control of TLP under wave action was carried out numerically by Chatterjee and Chakraborty [7]. It was detected that using TLCBD is better than TLCD for vibration reduction of TLP. The pitch motion response of a spar platform under irregular wave was reduced with installing a semi-active TLCD by Coudurier et al. [8]. The dynamic behavior of a modified spar platform with multilayer tuned liquid damper (TLD) was investigated by Ha and Cheong [9], numerically and experimentally. It was noticed that the multilayer TLD system suppresses a greater amount of the pitch motion response rather than the single layer TLD.

Moreover, there are several investigations about the coupling effect of internal fluid sloshing of the tank and vessel on the motion response of vessel, numerically and experimentally. Simulation of the 3D sloshing flow in anti-rolling tank using a finite difference method and ship motion using a time domain panel method were carried out by Kim [10]. The coupling between fluid sloshing of the tanks and motions of ship studied by Kim et al. [11], using the method of impulse response function formulation. Nasar et al [12] experimentally studied the effect of sloshing on the liquid barge tanks under regular beam waves. Zhao et al [13] experimentally showed that sloshing phenomena of inner tank plays significant role in the roll motion of the FLNG vessel. The motion response of a ship with a 3D rectangular container was studied by Mitra et al. [14], in the time domain approach. They studied nonlinear sloshing using a finite element method while the nonlinear ship motion was modeled by a hybrid marine control system. The coupling between sloshing, wave, and ship motion was investigated by Li et al. [15], using Open Filed Operation and Manipulation software. The effect of fluid sloshing inside the tank on the motion response of FLNG was investigated by Hu et al. [16], experimentally and numerically. The numerical modeling was developed by SESAM software. The experimental test carried out in the deep-water offshore basin at Shanghai Jiao Tong University, where good agreement between the results was observed. Liu [17] numerically simulated the floating oil storage tank response with considering the sloshing effect. It was modeled by SESAM software with both frequency domain and time domain approaches. The results showed that the internal liquid sloshing has a significant effect on its surge and especially pitch motion response.

It can be recognized that in literature, there are few attempts to suppress the pitch motion response of the semi-submersible platform with tuned dampers. It seems that using a type of tuned dampers is a suitable approach to improve pitch motion response of the semi-submersible platform. Therefore, in this study, tuned sloshing damper (TSD) is applied for semi-submersible platform.

A TSD plays a significant role to reduce structural vibration. The damping mechanism of the TSD is based on the energy dissipation of the fluid sloshing, to remove the energy from the structure equipped with TSD system, consequently decreasing its response. The significant advantage of TSD is low installation cost, easy to install, applicable to control a different vibration type of multi-degree of freedom system with different frequency for each other, and its natural frequency can be adjusted by water depth and container shape [2].

The TSD can also be classified as deep water and shallow water. If the internal liquid depth of the container relative to its length is less than 0.15, it will be shallow water; otherwise, it will be deep water. Although the effect of damping in shallow water type is significant, it is not appropriate in the large scale for externally excited vibration. Indeed, the analysis of the TSD with shallow water type in the large scale under the externally excited vibration is very difficult, because of the nonlinear behavior of water sloshing in the tank [2].

In this study, a new approach in the form of deep water type TSD is applied in the semi-submersible platform in order to reduce its pitch motion response. The studied platform is Iran Amirkabir semi-submersible rig with four TSDs located inside the bilge of its pontoons. It is represented as an equipped semi-submersible platform. The analysis is performed by using SESAM finite element software. Firstly, the structural model of the platform with TSDs is modeled. Secondly, the hydrodynamic analysis in the frequency domain is carried out by the same software, under the irregular waves. Finally, its motion response is estimated. It is concluded that utilizing TSDs can improve significantly the pitch motion response of the semi-submersible platform.

2. Description of the Semi-Submersible

Iran Amirkabri drilling rig is a type of GVA4000M platform that designed and manufactured for drilling oil or gas at water depth of 1000 meters in Caspian Sea, North of Iran. The geometrical form of this platform is simple and consists of two pontoons, four columns, two braces, deck, eight mooring lines and risers. The main hull dimensions of this platform are presented in Table 1[18].

Environmental characteristics of Caspian Sea for a return period of 100 years have also been reported in Table 2 [18]. In this study, waves of head sea (0^o direction) condition, which are the dominant waves, are used to obtain motions response (Table 2). In addition, the water density of Caspian Sea is considered as 1010 kg/m^3[18].

Table 1. Dimensions of Iran Amirkabir Platform

Characteristic	Value	Unit
Diameter of Columns	12.9	m
Diameter of braces	2	m
Transverse and Longitudinal distance of columns	54.72	m
Height to upper deck	36.5	m
Height to lower deck	28.5	m
Height to pontoon	7.5	m
Length of pontoon	80.56	m
Breadth of pontoon	18.68	m
Displacement at operational draught	28621	ton
Operation draught	20.5	m

Table 2. Environmental characteristics of Caspian Sea [18]

Orientation relative to north direction (degree)	Probability of occurrence (%)	Height of nominal wave (m)	Period (s)	Suitable Spectrum
0	24	10.50	16.25	JONSWAP

3. Theory of the floating motion and Sloshing

Sloshing means any motion of the free liquid surface inside its container. Depending on the type of disturbance and container shape, the free surface can create various types of motions includes simple planer, nonplanar, irregular beating, symmetric or asymmetric, quasi-periodic. The basic problem of liquid sloshing is to estimate its hydrodynamic performances such as pressure distribution, forces, reactions, moments, and its natural frequencies. Also, these parameters can significantly influence on the dynamic behavior and performance of a moving structure supporting this container [19].

For a rigid body with six degrees of freedom, the governing equation of motion is expressed in the form of Eq. (1)[20].

$$\left[M_{ij}+m_{ij}(\omega)\right]\ddot{\varepsilon}+C_{ij}(\omega)\dot{\varepsilon}+K_{ij}\varepsilon=F(\omega) \qquad (1)$$

where, M_{ij} is the mass matrix of floating platform, $m_{ij}(\omega)$ is the hydrodynamic added mass matrix, $C_{ij}(\omega)$ is the hydrodynamic damping matrix, ε is the related rigid body motion, K_{ij} is the hydrostatic restoring matrix and $F(\omega)$ is the vector of exciting wave force.

When the TSD is installed inside the floating structure, the internal fluids free surface moves according to the tank motions. Consequently, the coupling effect of sloshing phenomena and floating container will be occurred. Therefore, the motion equation of rigid body will be modified as Eq. (2) [2].

$$\left[M_{ij}+m_{ij}(\omega)+m_{ij-\tan k}(\omega)\right]\ddot{\varepsilon}+\left[C_{ij}(\omega)+C_{ij}^{*}\right]\dot{\varepsilon}+\left[K_{ij}+K_{ij-\tan k}\right]\varepsilon=F(\omega) \qquad (2)$$

where, $m_{ij-\tan k}(\omega)$ is the added mass due to the internal liquid motion, C^{*} is the linear equivalent damping coefficient and considered as viscous damping and $K_{ij-\tan k}$ is the hydrostatic restoring matrix of the tanks.

In this paper, the studied floating structure is a semi-submersible platform equipped with TSD systems. It is analyzed by using SESAM software. It is a robust finite element software where is widely applied in offshore engineering. It is used for analyzing of fix as well as floating structures, mooring and riser systems, and pipelines [21].

4. Numerical Modeling

Before the investigation on the hydrodynamic behavior of the equipped semi-submersible platform, the accuracy of the applied software must be verified in the modeling process as well as in the calculation of the coupling effect of sloshing and vessel motions.

4.1. Validation of the numerical modeling

In order to verify the numerical modeling process, a similar platform without TSD is modeled (Fig 1). This platform is a GVA4000 type drilling rig platform with geometrical dimensions illustrated in Fig. 1 and 2. The experimental heave and pitch RAOs data of this platform are available which was performed over a model with scale 1:81 in a wave flume with length of 80m, width of 4m and water depth of 1.5 m under the rogue and monochromatic waves. Its behavior was studied under random waves with JONSWAP spectrum, significant wave height of 11.92 m and zero-up crossing period of 10.8 s with a maximum height of 25.63 m and crest elevation of 18.5 m [22].

Figs. 3 and 4 illustrate both numerical modeling and experimental data of the heave and pitch RAOs, which indicates suitable agreement.

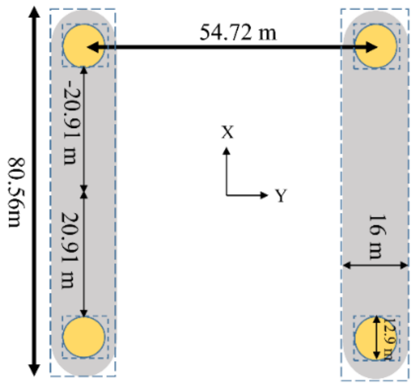

Figure 1. **The Top side of the studied GVA4000 semi-submersible drilling platform.**

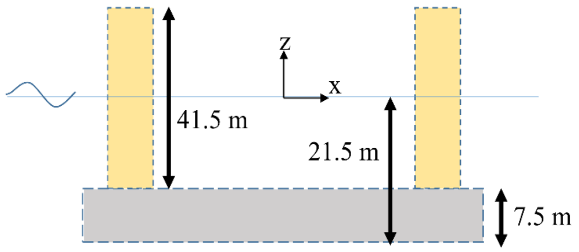

Figure 2. **The front side of the studied GVA4000 semi-submersible drilling platform.**

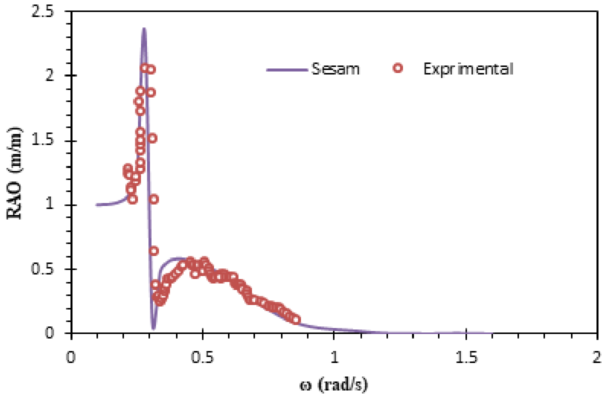

Figure 3. **Comparison of the numerical and experimental heave RAO under the head sea waves**

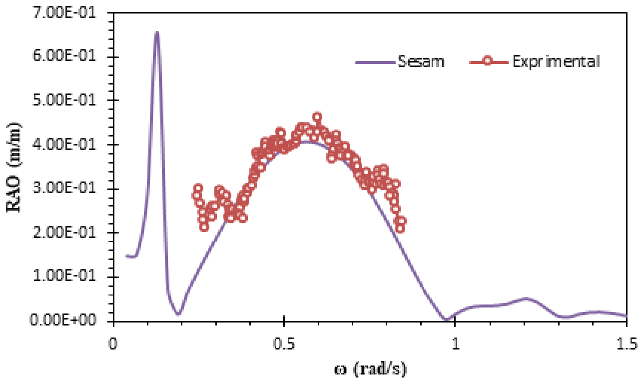

Figure 4. **Comparison of the numerical and experimental pitch RAO under the head sea waves**

4.2. Validation of the Effect of Sloshing

In the next step, the coupling effect of the internal fluid sloshing of the tank with the vessel motions is verified. For this purpose, a type of floating oil storage tank (FOST) is considered. The FOST is contained from an external rectangular tank and internal cylindrical with dimensions of 35m x 35m x 20m, which designed to store diversity oil products. It is located in the near-shore area around Singapore with the water depth of 30m. The density of water is 1025 kg/m^3 and oil is 870 kg/m^3 [2].

The structural model of FOST which is filled up to 40% with oil is simulated (Fig. 5 and 6) and then the coupling effect of liquid sloshing and FOST motion is investigated in the frequency domain.

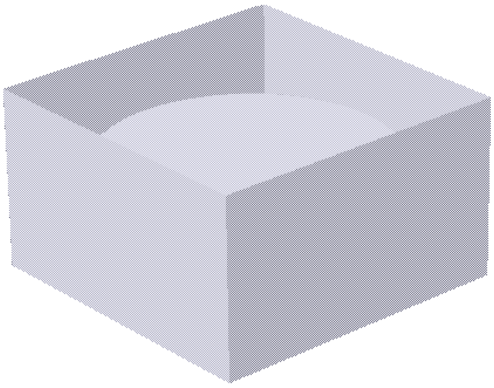

Figure 5. **Structural modeling of FSOT**

Figure 6. **The FSOT with 40% oil filled**

The comparison of the heave and pitch RAOs of modeled FOST and the results of Liu's study [2] have been illustrated in Figs 7 and 8. The results are close enough to be considered acceptable. Moreover, the comparison of FOST filled up to 40% with oil and the empty one shows the applied method can simulate the coupling between the sloshing and FOST motions. It is notable the effect of the sloshing is more visible in the pitch motion of FOST.

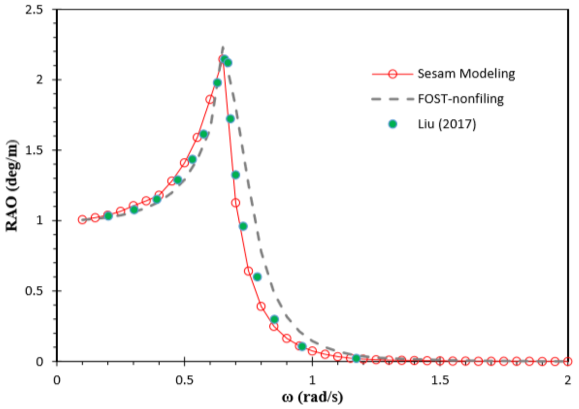

Figure 7. **Comparison of the results modeled FOST and Liu** [2] **for heave RAO under the head sea waves**

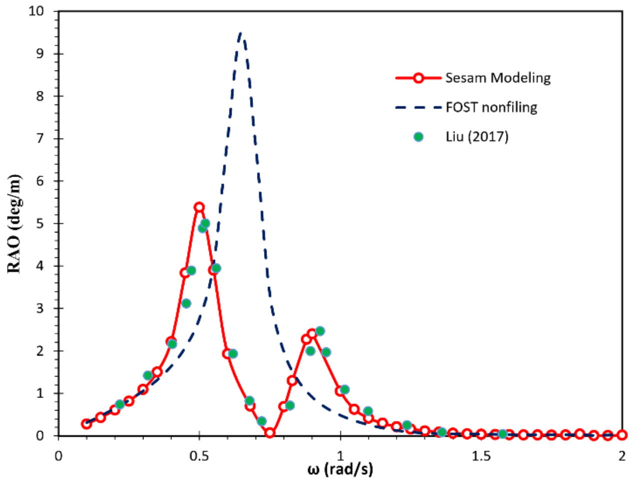

Figure 8. Comparison of the results modeled FOST and Liu [2] pitch RAO under the head sea waves

4.3. Modeling of Equipped Semi-Submersible

In the next step, the structural model of Iran Amirkabir semi-submersible platform is simulated with different parts such as pontoons, columns, bracings, and deck (Fig. 9). Four semicircular TSDs are placed inside the bilge of pontoons (Fig. 10). The radius of TSDs is 9.34 m and its height is 7.5 m.

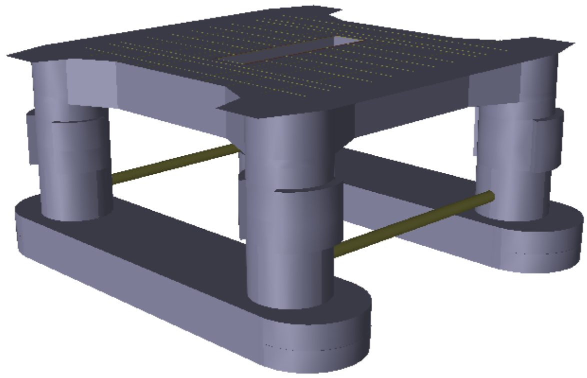

Figure 9. The developed model of Iran-Amirkabir

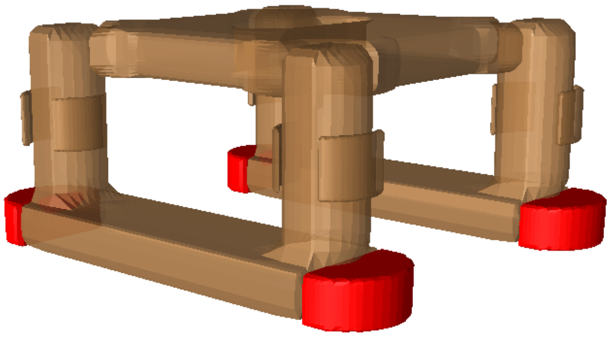

Figure 10. Semicircle TSDs placed inside the bilge of pontoons of the semi-submersible platform.

4.3.1 Hydrodynamic Behavior of Equipped Semi-Submersible

To determine the effect of TSD on the semi-submersible motions, the TSD's fluid properties such as filling fraction and fluid density are defined and associated with the structural model. The filling fraction includes 20% water by assuming the deep water type and density of 1010 kg/m^3 (Fig. 11).

Modeling is carried out in the frequency domain with considering the dynamic behavior of the TSDs' fluid, under the environmental characteristics of Caspian Sea. Finally, the results of its motions are processed. The corresponding numerical simulation results and their comparison with the original semi-submersible platform have been given in Figs. 12-14.

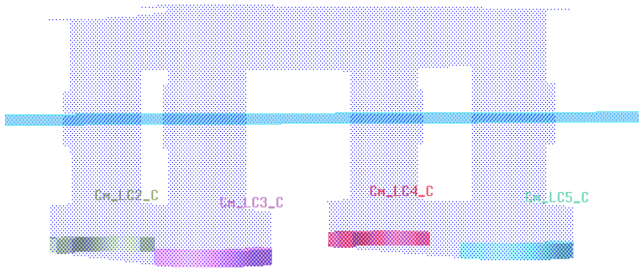

Figure 11. Iran Amirkabir platform equipped with TSDs filled up to 20% with water

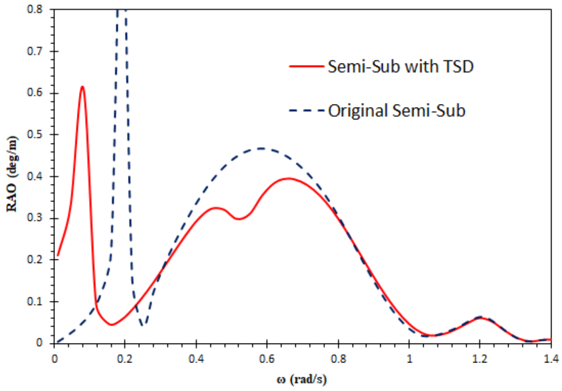

Figure 12. Comparison of pitch RAO of equipped semi-submersible platform with original case under the head sea waves

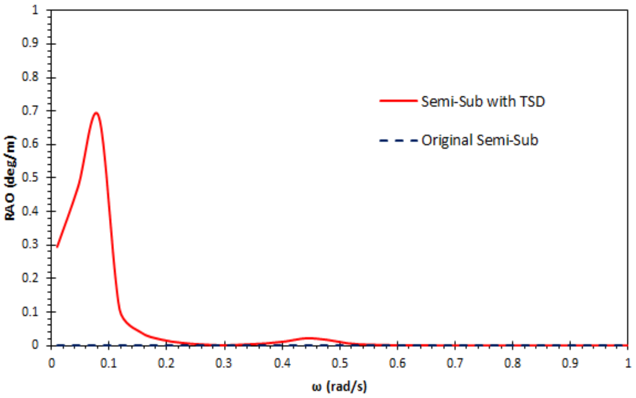

Figure 13. Comparison of roll RAO of the equipped semi-submersible platform with its original case

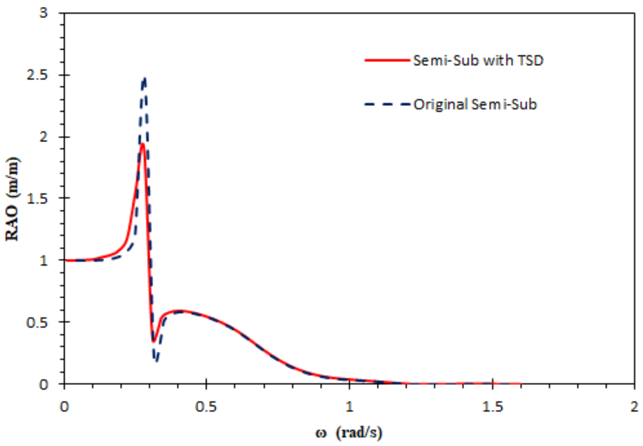

Figure 14. **Comparison of heave RAO of the equipped semi-submersible platform with original case**

4.3.2. Motion Response Spectrum

In order to determine the effect of TSDs on the motion response of the semi-submersible platform, the value of the motion response must be evaluated which is calculated using Eq. (3).

$$S_s(\omega) = RAO^2 \times S_{JONSWAP},$$
$$m_{0s} = \int_0^{\infty} S_s(\omega) d\omega, \tag{3}$$
$$(2S)_s = 4\sqrt{m_{0s}}$$

Irregular waves based on JONSWAP spectrum [23] is applied.The characteristics of Caspian Sea waves (Table. 2) are used. The results of the pitch, roll and heave motions are compared with the original platform in Figs. 15-17. Moreover, the reduction percentage relative to the original platform are presented in Table 3. As shown, the pitch motion has reduced more than 30% whilst slight changes are observed in heave and roll motions. As a result, using TSD system is a way appropriate for improving pitch motion response of the semi-submersible platform without making considerable change in the heave and roll motion response.

Table 2. Comparison of the maximum pitch motion response of the equipped semi-submersible platform with original case

Motions of equipped semi-sub	Value of motion response of original case	Value of motion response of equipped semi-sub	Percentage of reduction
Pitch (deg)	1.58	1.10	30.37
Roll (deg)	0	1.2E-6	-
Heave (m)	1.865	1.805	3.217

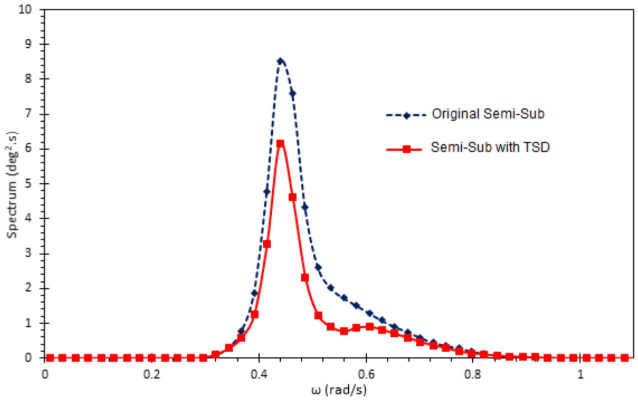

Figure 15. **Comparison of pitch motion response of the equipped semi-submersible platform with original case**

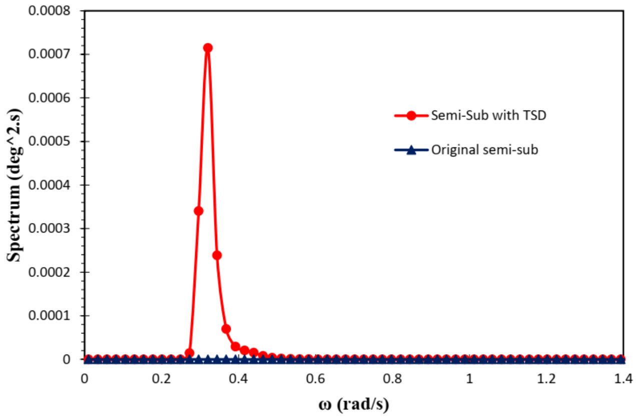

Figure 16. **Comparison of roll motion response of the equipped semi-submersible platform with original case**

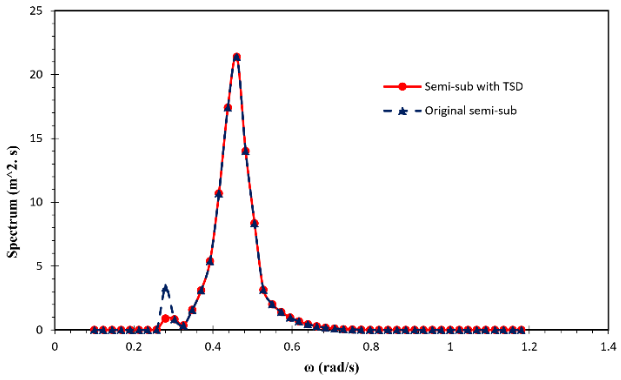

Figure 17. **Comparison of heave motion response of the equipped semi-submersible platform with original case**

4.4. Effect of the Filling Fraction

The pitch motion response of the equipped semi-submersible is studied with different filling fraction for TSD including 20%, 40%, and 60%. The corresponding results for pitch RAO are given in Fig. 18. Furthermore, the pitch motion response spectrum is illustrated in Fig. 19. Obviously, by decreasing water filling fraction, the pitch motion response would be more suppressed (Table 3). Therefore, TSD with 20% water filling fraction is more suitable.

Table 3. Comparison of pitch motion response of the equipped semi-submersible platform with different filling fraction for TSD

Filling ratio	Pitch Motion Response (degree)	Percentage of reduction for Pitch motion response
Original	1.58	-
20%	1.10	30.37
40%	1.234	21.8
60%	1.285	18.6

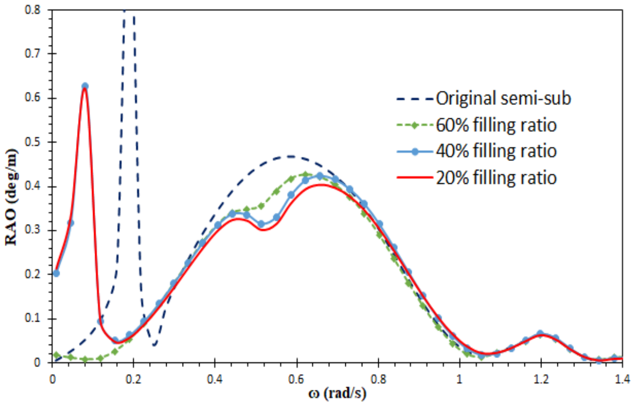

Figure 18. **Comparison of pitch RAO of equipped semi-submersible platform with 20%, 40%, and 60% water filling fraction under the head sea waves**

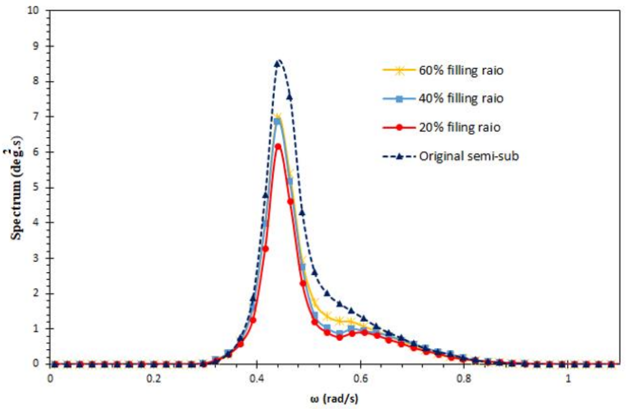

Figure 19. **Comparison of pitch motion response of the equipped semi-submersible with 20%, 40%, and 60% water filling fraction under the head sea waves**

5. Conclusion

Offshore platforms are unique structures that pose many challenges in their development and conceptual design. A semi-submersible platform is the category of offshore platform which commonly used for gas and oil exploration in deep waters. The heave, pitch or roll motion response of the conventional semi-submersible platforms are relatively significant. This can often limit their operability especially for drilling rigs or even can damage to its risers and mooring system. In this paper, it was focused on the pitch motion response of Iran-Amirkabri semi-submersible rig with four TSDs. It was named as an equipped semi-submersible platform. A finite element software was applied to simulate its hydrodynamic behavior. The results of the equipped semi-submersible platform was calculated and compared with original case. The following conclusions were obtained:

- The pitch motion response has two separate peaks: one close to the peak wave frequency and the other at the sloshing natural frequency.
- The pitch motion response of the equipped semi-submersible platform is decreased by about 30% relative to its original case.
- The heave and roll motion response of the equipped semi-submersible platform is slightly changed relative to the original case.
- The value of the filling fraction of TSD can be effective for reducing the pitch motion response of the semi-submersible platform.

It is summarized that TSDs are an appropriate device to suppress pitch motion response of the semi-submersible platform. Moreover, this study can make significant contribution to the more economical and more efficient design of semi-submersible oil and gas drilling platforms.

6. References

1- Kandasamy, R., Cui, F., Townsend, N., Foo, C. C., Guo, J., Shenoi, A., Xiong, Y. J. O. E., (2016), A review of vibration control methods for marine offshore structures., Vol. 127, pp. 279-297.

2- Nanda, B., (2010), Application of tuned liquid damper for controlling structural vibration, Master Thesis,National Institute of Technology, Rourkela.

3- Spillane, M. W., Rijken, O. R., Leverette, S. J., (2007), In Vibration absorbers for deepwater TLP's, The Seventeenth International Offshore and Polar Engineering Conference, International Society of Offshore and Polar Engineers.

4- Karimi, H. R., Zapateiro, M., Luo, N., (2010), In Semiactive vibration control of offshore wind turbine towers with tuned liquid column dampers using H∞ output feedback control, 2010 IEEE International Conference on Control Applications, IEEE: pp 2245-2249.

5- Luo, N., Bottasso, C., Karimi, H. R., Zapateiro, M., (2011), In Semiactive control for floating offshore wind turbines subject to aero-hydro dynamic loads, International Conference on Redevelopedable Energies and Power Quality (ICREPQ'11) Las Palmas de Gran Canaria (Spain), 13th to 15th April, 2011.

6- Lee, H. H., Juang, H. J. S. S., (2014), Systems, Experimental study on the vibration mitigation of offshore tension leg platform system with UWTLCD**,** Vol. 9 (1), pp. 71-104.

7- Chatterjee, T., Chakraborty, S. J. O. E., (2014), Vibration mitigation of structures subjected to random wave forces by liquid column dampers. Vol. 87, 151-161.

8- Coudurier, C., Lepreux, O., Petit, N. J. I. P., (2015), Passive and semi-active control of an offshore floating wind turbine using a tuned liquid column damper. Vol. 48 (16), pp. 241-247.

9- Ha, M., Cheong, C. J. O. E., (2016), Pitch motion mitigation of spar-type floating substructure for offshore wind turbine using multilayer tuned liquid damper, Vol. 116, pp. 157-164.

10- Kim, Y. J. J. O. S. R., (2002), A numerical study on sloshing flows coupled with ship motion the anti-rolling tank problem, Vol. 46 (1), pp. 52-62.

11- Kim, Y., Nam, B., Kim, D., Kim, Y. J. O. E., (2007), Study on coupling effects of ship motion and sloshing, Vol. 34 (16), pp. 2176-2187.

12- Nasar, T., Sannasiraj, S., Sundar, V. J. F. D. R., (2008), Experimental study of liquid sloshing dynamics in a barge carrying tank, Vol. 40 (6), p. 427.

13- Zhao, W. H., Yang, J.M., Hu, Z. Q., Xiao, L. F. J. J. O. H., Ser. B, (2012), Experimental investigation of effects of inner-tank sloshing on hydrodynamics of an FLNG system, Vol. 24 (1), pp. 107-115.

14- Mitra, S., Wang, C., Reddy, J., Khoo, B. J. O. E., (2012), A 3D fully coupled analysis of nonlinear sloshing and ship motion. Vol. 39, pp. 1-13.

15- Li, Y. l., Zhu, R.C, Miao, G. P., Ju, F. J. J. o. H., Ser. B, (2012), Simulation of tank sloshing based on OpenFOAM and coupling with ship motions in time domain, Vol. 24 (3), pp. 450-457.

16- Hu, Z. Q., Wang, S. Y., Chen, G., Chai, S. H., Jin, Y. T. J. I. J. o. N. A., (2017), The effects of LNG-tank sloshing on the global motions of FLNG system, International Journal of Naval Architecture and Ocean Engineering, Vol. 9 (1), pp. 114-125.

17- Liu, X., (2017), Numerical modelling and simulation of floating oil storage tanks considering the sloshing effect. Master thesis, Norwegian University of Science and Technology.

18- Armak, S., Mostafa Gharebaghi, A. R., (2012), In Effect of HEAVE plates on the dynamic response of Amirkabir semi-submersible platform, Proceeding of International Conference on Coasts, Ports and Marine Structures.

19- Ibrahim, R. A., (2005), Liquid sloshing dynamics: theory and applications. Cambridge University Press.

20- Patel, M. H., (2013), Dynamics of offshore structures. Butterworth-Heinemann.

21- Ludewig, J., Bassler, T., Deininger, M., Schneider, K., Schwille, J., (1992), In SESAM-simulating software projects, Proceedings Fourth International Conference on Software Engineering and Knowledge Engineering, IEEE, pp 608-615.

22- Clauss, G. F., Schmittner, C., Stutz, K., (2002), In Time-domain investigation of a semisubmersible in rogue waves, ASME 2002 21st International Conference on Offshore Mechanics and Arctic Engineering, American Society of Mechanical Engineers, pp 509-516.

23- Goda, Y. J. C. E. J., (1999), A comparative review on the functional forms of directional wave spectrum, Vol. 41 (1), pp. 1-20.